

**Development of flat-field EUV spectrometers
with absolute calibration and
study of impurity behavior in edge plasmas
on LHD**

Malay Bikas Chowdhuri

Doctor of Philosophy

**Department of Fusion Science
School of Physical Sciences
The Graduate University for Advanced Studies**

2008

Abstract

Impurity control is one of crucial problems to be solved in fusion research. The extreme ultraviolet (EUV) spectroscopy gives a major diagnostic technique to monitor and study the impurity behavior in magnetically confined fusion plasmas. For the purpose, two flat-field EUV spectrometers for impurity diagnostics in 10–130 and 50–500Å ranges have been developed with varied-line-spacing (VLS) laminar-type holographic gratings. The spectral characteristics obtained from the holographic gratings were compared with ones from conventional ruled gratings and excellent property was found in the holographic gratings, i.e., negligibly low level of stray light and higher-order emission intensity. The EUV spectrometers have been absolutely calibrated using a new technique based on the combination of EUV bremsstrahlung and branching ratio. EUV spectra have been thus successfully observed from high-temperature plasmas in Large Helical Device (LHD) and several EUV line emissions of Ti, Fe, Mo and W have been analyzed and identified in detailed for the purpose of further development of the impurity diagnostics.

The edge impurity transport in intrinsically existing ergodic layer of LHD, where the transport parallel to magnetic fields is relatively dominant, has been studied through the observation of carbon emissions. Four resonance transitions of CIII (977Å: $2s2p\ ^1P_1-2s^2\ ^1S_0$), CIV (1548Å: $2p\ ^2P-2s\ ^2S$), CV (40.27Å: $1s2p\ ^1P_1-1s^2\ ^1S_0$) and CVI (33.73Å: $2p\ ^2P-1s\ ^2S$) have been observed with the EUV spectrometers and 20cm normal incidence VUV spectrometers. The ratio of CV+CVI to CIII+CIV has been analyzed in a variety of magnetic configurations and plasma parameters. The impurity screening was evidently observed and the physical mechanism on the impurity transport given by the edge stochastic magnetic fields has been discussed with the thermal force and friction force. The modeling of the edge impurity transport with EMC3+EIRENE simulation code strongly suggests the importance of the friction force for the enhancement of the impurity screening. The density dependence of the measured ratio indicating the impurity screening effect is in good agreement with the modeling result.

Contents

1. Introduction	1
1.1. Impurity in nuclear fusion research.....	1
1.2. EUV spectroscopy.....	2
1.3. Motivation of the present study.....	4
1.4. LHD and relevant diagnostics.....	6
References.....	11
2. Development of EUV spectrometers and their calibration	13
2.1. Spectrometer for 50-500Å (EUV_Long).....	13
2.1.1. Introduction.....	13
2.1.2. Details on 1200grooves/mm flat-field EUV spectrometer.....	14
2.1.3. Comparison between ruled and holographic gratings.....	21
2.1.4. Absolute intensity calibration.....	25
2.1.5. Summary.....	29
2.2. Spectrometer for 10-130Å (EUV_Short).....	31
2.2.1. Introduction.....	31
2.2.2. Details on 2400grooves/mm flat-field EUV spectrometer.....	32
2.2.3. Comparison between ruled and holographic gratings.....	36
2.2.4. Absolute intensity calibration.....	42
2.2.5. Summary.....	46
2.3. Spectroscopic evaluation on a ruled and two holographic gratings to monitor 10-30Å.....	47
2.3.1. Introduction.....	47
2.3.2. Comparative studies on a ruled and two holographic gratings.....	49
2.3.3. Summary.....	53
2.4. Comparison between 1200 and 2400grooves/mm gratings.....	54
References.....	57
3. EUV spectra and line analysis	59
3.1. Details on high-Z Mo and W spectra observed by EUV_Long.....	59
3.1.1. Introduction.....	59
3.1.2. Experimental setup.....	60
3.1.3. EUV spectra and analysis.....	61
3.1.3.1. Molybdenum.....	61
3.1.3.2. Tungsten.....	66
3.1.4. Summary.....	68
3.2. Details on low- and medium-Z spectra observed by EUV_Short.....	69
References.....	76

4. Analysis on carbon behavior in LHD.....	77
4.1. CIII to CVI behaviors during recombining phase.....	77
4.1.1. Introduction.....	77
4.1.2. Experimental setup.....	78
4.1.3. Description of calculation.....	79
4.1.4. Results and discussions.....	80
4.1.4.1. Temporal evolution of carbon emissions during recombining phase.....	80
4.1.4.2. Density dependence of carbon emissions during recombining and steady state phases.....	87
4.1.5. Summary.....	89
4.2. Edge impurity transport study of plasmas with ergodic layer using CIII to CVI....	92
4.2.1. Introduction.....	92
4.2.2. LHD edge magnetic structures.....	93
4.2.3. Experimental setup.....	96
4.2.4. Brief description on impurity transport in ergodic layer.....	97
4.2.5. Experimental results and discussions.....	99
4.2.5.1. Density dependence of carbon emissions.....	103
4.2.5.2. Carbon emissions with different magnetic axes.....	105
4.2.5.3. Carbon emissions with externally supplied $m/n=1/1$ magnetic island.....	110
4.2.5.4. Carbon emissions with H ₂ and He discharges.....	114
4.2.6. Comparison with simulated carbon emission with edge transport code.....	118
4.2.7. Summary.....	123
References.....	124
5. Summary and conclusion.....	127
Acknowledgements.....	131
List of publications.....	133

List of Figures

1.1	Cross sectional view of LHD with magnetic field structure, coils position, vacuum vessel and cryostat.....	7
2.1	Details of EUV flat-field spectrometer.....	15
2.2	Schematic diagram of EUV flat-field spectrometer.....	16
2.3	Calculated focal curves as a parameter of angles of incidence.....	17
2.4	Experimentally obtained spectral resolution before and after alignments.....	18
2.5	Theoretical and experimental reciprocal linear dispersions as a function of wavelength.....	20
2.6	Typical spectra with ruled and holographic gratings.....	21
2.7	Experimentally obtained spectral resolution for ruled and holographic gratings as a function of wavelength.....	22
2.8	Peak intensity of higher order light and raw spectra including higher order emission for ruled and holographic gratings.....	24
2.9	Experimental and estimated continuum as a function of wavelength for ruled and holographic gratings.....	27
2.10	Variation of relative sensitivities as a function of wavelength for ruled and holographic gratings.....	28
2.11	Inverse absolute sensitivity of holographic grating EUV spectrometer as a function of wavelength.....	28
2.12	Schematic drawing and design specification of 2400grooves/mm EUV flat-field spectrometer.....	33
2.13	Calculated focal curves of 2400grooves/mm VLS concave grating as a parameter of angle of incidence.....	34
2.14	Experimental and theoretical reciprocal linear dispersions as a function of wavelength.....	35
2.15	Experimentally obtained spectral resolution at three wavelengths as a function of distance from designed linear focal position.....	36
2.16	Typical EUV spectra with ruled and holographic gratings.....	37

2.17 Experimentally obtained spectral resolution for ruled and holographic gratings as a function of wavelength.....	38
2.18 Examples of Gaussian fitted line profile showing spectral resolution for ruled and holographic grating.....	40
2.19 EUV spectra from LHD discharges obtained for ruled and holographic gratings representing higher order CVI emissions.....	41
2.20 Calculated and experimental EUV bremsstrahlung continuum as a function of wavelength for ruled and holographic gratings.....	43
2.21 Variation of relative sensitivities against wavelength for ruled and holographic gratings.....	44
2.22 Absolute sensitivity of 2400grooves/mm EUV spectrometer with ruled and holographic gratings as a function of wavelength.....	45
2.23 Typical spectra from LHD discharges obtained with ruled, old holographic and new holographic gratings.....	48
2.24 Inverse absolute sensitivities as a function of wavelength for ruled, old holographic and new holographic gratings.....	50
2.25 Experimentally obtained spectral resolution for ruled, old holographic and new holographic gratings as a function of wavelength.....	51
2.26 Computationally simulated spectral resolution for old and new holographic gratings as a function of wavelength.....	52
2.27 Local groove line-spacing as a function of distance from grating center for old and new holographic gratings.....	53
2.28 Comparison between EUV Spectra in 50 to 130Å simultaneously recorded from two flat-field spectrometers of EUV_Short and EUV_Long.....	55
2.29 Comparison of spectral resolution (FWHM) and absolute sensitivity between two EUV spectrometers.....	56
3.1 Mo spectrum in 20–165Å.....	62
3.2 Mo spectrum in 165–315Å.....	64
3.3 Mo spectrum in 315–500Å.....	64
3.4 W spectra in 24–80Å at $\Delta t=340$ and 440ms after pellet injection.....	65
3.5 EUV spectrum in 20 to 65Å of H- and He-like ions from low-Z impurities.....	70

3.6 FeXVII-XXIV EUV spectrum of n=2-3 transitions from L-shell partially ionized iron and neon EUV spectrum.....	71
3.7 TiXIII-XX EUV spectrum of n=2-3 transitions from L-shell partially ionized titanium.....	73
4.1 Typical discharge for the present analysis showing plasma stored energy, NBI heating pulses, $\langle n_e \rangle$, $T_e(0)$ and emissions of CIII, CIV, CV and CVI.....	81
4.2 Time behaviors of central electron temperature and horizontal plasma radius at horizontally elongated plasma cross section during recombining phase.....	82
4.3 Calculated and experimental total radiation power of CIII, CIV, CV and CVI.....	83
4.4 Radial profiles of n_e , T_e and densities and emissivities of CIII to CVI.....	84
4.5 Fractional abundances and emissivities for CIII, CIV, CV and CVI.....	86
4.6 CVI intensity and $CVI/(n_e Q)$ plotted against line-averaged electron density for recombining and steady state phases.....	88
4.7 CV intensity and $CV/(n_e Q)$ plotted against line-averaged electron density for recombining and steady state phases.....	90
4.8 CIII intensity against line-averaged electron density for recombining and steady state phases.....	91
4.9 CIV intensity against line-averaged electron density for recombining and steady state phases.....	91
4.10 Schematic views of horizontally elongated plasma cross section in $R_{ax}=3.6$ and 4.0m of LHD.....	94
4.11 Edge profiles of magnetic field connection length as a function of major radius at outboard side of horizontally elongated plasma cross section in $R_{ax}=3.6$ and 4.0m.....	95
4.12 Fractional abundances of C^+ , C^{+2} , C^{+3} , C^{+4} , C^{+5} and C^{+6} as a function of T_e	100
4.13 Vertical profiles of CIII, CIV and CV at $R_{ax}=3.6$ m.....	102
4.14 View chords of visible spectrometer and magnetic field structure of LHD in $R_{ax}=3.6$ m.....	102
4.15 Ratio of $CV+CVI$ to $CIII+CIV$ and normalized intensities of $(CV+CVI)/n_e$ and $(CIII+CIV)/n_e$ for $R_{ax}=3.6$ m.....	103
4.16 Edge n_e and T_e profiles for low- and high-density discharges in $R_{ax}=3.6$ m.....	104

4.17 Ratio of CV+CVI to CIII+CIV and normalized intensities of (CV+CVI)/n _e and (CIII+CIV)/n _e in R _{ax} =3.60, 3.75, 3.90 and 4.00m.....	106
4.18 Edge profiles of magnetic field connection length, L _c , at inboard and outboard sides for horizontally elongated plasma cross section in R _{ax} =3.60, 3.75, 3.90 and 4.00m.....	107
4.19 Ergodic layer thickness at inboard and outboard sides in horizontally elongated plasma cross section.....	108
4.20 Edge n _e and T _e profiles for R _{ax} =3.60 and 4.00m.....	109
4.21 Radial profiles of rotational transform in R _{ax} =3.60, 3.75, 3.85, 3.90 and 4.00m....	109
4.22 Magnetic field structures of edge ergodic layer at horizontally elongated plasma cross sections R _{ax} =3.75 and 3.85m with and without LID.....	111
4.23 Ratio of CV+CVI to CIII+CIV and normalized intensities of (CV+CVI)/n _e and (CIII+CIV)/n _e for R _{ax} =3.75 and R=3.85m without and with LID.....	112
4.24 Edge n _e and T _e profiles with and without LID at R _{ax} =3.75 and 3.85m.....	113
4.25 Ratio of CV+CVI to CIII+CIV and normalized intensities of (CV+CVI)/n _e and (CIII+CIV)/n _e for H ₂ and He discharges.....	115
4.26 Plasma stored energy, line-averaged density and normalized intensities of CIII/n _e , CIV/n _e , CV/n _e and CVI/n _e in H ₂ and He discharges.....	116
4.27 T _e at ρ=1 and divertor ion saturation current for H ₂ and He discharges.....	117
4.28 2-dimensional profile of connection length in ergodic layer of LHD (R _{ax} =3.75m) superposed with Poincare plot of magnetic field lines.....	118
4.29 Edge profiles of carbon density summed up over all charge states for different edge densities of n _{LCFS} =2 and 4×10 ¹⁹ m ⁻³	119
4.30 Ratios of CV to CIII+CIV obtained from experiment and simulation with and without friction force.....	120
4.31 Radial carbon density profiles of each charge state simulated by EMC3-EIRENE code with n _{LCFS} =2 and 4×10 ¹⁹ m ⁻³	122

List of Tables

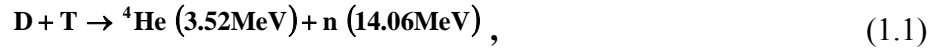
1.1	LHD plasma diagnostics.....	8
2.1	Observed transitions of Mo ($Z=42$) ions in 65–90Å.....	63
2.2	Observed transitions of W ($Z=74$) ions in 24–40Å.....	67
2.3	Observed transitions of W ($Z=74$) ions in 50–70Å.....	68
2.4	Observed n=2-3 transitions of L-shell partially ionized Fe ($Z=26$) ions in 10 to 20Å.....	72
2.5	Observed n=2-3 transitions of L-shell partially ionized Ti ($Z=22$) ions in 10 to 30Å.....	74

Chapter 1

Introduction

1.1. Impurity in nuclear fusion research

The most promising nuclear reaction for fusion reactor using magnetic confinement is;



where D and T are the deuterium and tritium, respectively, and ${}^4\text{He}$ (alpha particle) and n (neutron) are the nuclear reaction product. High temperature ($\sim 10\text{keV}$) and high density ($\sim 10^{20}\text{m}^{-3}$) plasma is required to produce enough fusion output. The Lawson criterion [1] gives the physical condition for the fusion reactor formation based on the α particle heating. It is defined by the fusion triple product of the plasma energy confinement time, τ_E , plasma temperature, T, and plasma ion density, n_i and gives us the following relation;

$$n_i T \tau_E > 10^{21} \text{ m}^{-3} \cdot \text{keV} \cdot \text{s}, \quad (1.2)$$

where τ_E is defined by

$$\tau_E = W_p / P_{in}. \quad (1.3)$$

Here, W_p is the plasma stored energy and P_{in} is the input heating power.

Impurities such as carbon, oxygen and metallic elements intrinsically exist in the magnetic confined plasmas since several plasma facing components are installed in the vacuum vessel [2, 3]. The presence of impurities leads to an increase of radiation loss in addition to a dilution of fuel ions [4]. The net input power, P_{in-net} , is reduced by the radiation loss as

$$P_{in-net} = P_{in} - P_{rad}. \quad (1.4)$$

Impurity control becomes basically an important issue in fusion research. The control of metallic impurities is essentially required, since the radiation loss from high-Z impurities

is much bigger than low-Z impurities [5]. The line radiation loss from a specific impurity element is expressed by

$$\mathbf{P}_{\text{rad}} = \mathbf{n}_e \mathbf{n}_{\text{imp}} \mathbf{R} , \quad (1.5)$$

where R is the radiation coefficient as a function of electron temperature. The total radiation loss is the sum of line emissions from impurities. The impurity control becomes a crucial issue in fusion research. Therefore, the study of the impurity behavior is also important to find better impurity control method.

1.2. EUV spectroscopy

In fusion plasmas, carbon (Z=6) is widely used as a plasma facing component in the vacuum vessel and oxygen (Z=8) exists on the surface of the plasma facing component as water and carbon oxide. Nitrogen (Z=7) sometimes appears after opening of the vacuum vessel. Boron (Z=5) is found through boronization which is one of methods to control the impurity content. These impurities are called 'low-Z impurity'. On the other hand, metallic impurities such as chromium (Z=24) and iron (Z=26) are basically originated in the vacuum vessel made of stainless steel. Titanium gettering to suppress the oxygen influx brings titanium (Z=22) into plasmas. These impurities are called 'medium-Z impurity' in the present thesis. Recently, the use of high-Z impurity like molybdenum (Z=42) and tungsten (Z=74) is planned in ITER as a candidate for the plasma facing components.

The extreme ultraviolet (EUV) wavelength range of 10–500Å contains many strong spectral lines which can be used as a tool for spectroscopic diagnostics. For example, $\Delta n=0$ resonance transitions from partially ionized medium-Z impurities are emitted in the 90–500Å range [3, 6]. This range also contains spectral lines from higher excited states in low-Z impurities [3, 7]. Resonance lines from H- and He-like ions of B, N, C, and O appear in 10–65Å. This shorter wavelength range also contains $\Delta n=1$ transitions from Ti and Fe [3, 8]. Strong spectral band appears in 45–85Å range for Mo

and W [9, 10]. Therefore, the observation of spectra in this EUV range is very crucial to understand the impurity behavior in fusion plasmas.

Plasma spectroscopy in the EUV range is commonly performed using a grazing incidence spectrometer based on diffraction grating. This grating consists of a large number of grooves ruled on concave substrate. The groove structure makes possible to diffract the incident light into one or more spectral orders according to the grating equation [11];

$$m\lambda = d(\sin\alpha + \sin\beta) , \quad (1.6)$$

where λ , d and m are the wavelength of light, groove spacing and spectral order number, respectively. The values of α and β are the angles of incidence and diffraction, respectively. In the EUV range, the angle of incidence has to be large, since the reflectivity on the grating becomes low for shorter wavelength. Therefore, the grazing incidence spectrometer is used instead of normal incidence spectrometer. The focal mechanism of the traditional grazing incidence spectrometer [12] is based on Rowland circle geometry [13]. However, the focal position is curved along the Rowland curve. It is difficult for the grazing spectrometer to observe spectra using multichannel detector such as charge couple device (CCD). The grazing incidence spectrometer is then limited to use as monochromator.

A flat focal plane is required in order to observe the EUV spectra with good spectral resolution. Fonck et al. has developed an EUV spectrometer for measurement of 100-1100Å range using 450grooves/mm flat focal toroidal grating with spectral resolution of $\sim 2\text{Å}$ [14]. It can also monitor the EUV spectra with better resolution of $\sim 0.4\text{Å}$, replacing by 2100grooves/mm toroidal grating. The complete flat focal plane has been achieved by Kita et al. [15] using an aberration corrected varied-line-spacing (VLS) grooves spherical-concave grating which focuses all diffracted rays onto the flat plane. The flat focal plane therefore provides the same spectral resolution along a certain wavelength interval. The necessary ruled grating is manufactured using a feedback-controlled mechanical ruling machine. The EUV spectra have been observed using this flat-field spectrometer with VLS ruled grating at least during past 20 years.

1.3. Motivation of the present study

The EUV spectrometer with VLS ruled grating usually suffers from higher order effect and larger stray light. The influence is typically seen in the line identification. The identification becomes often difficult because many spectral lines closely exist in the EUV wavelength range and the 1st order original lines overlap with many other higher orders lines. Therefore, it is pointed out that further improvement is required in addition to its sensitivity and spectral resolution. One of the candidates for the improvement is the replacement of the ruled grating by the holographic grating. It is well known that the holographic grating has a specific property to suppress the higher orders light and the stray light [16].

Recently, the VLS laminar-type holographic grating has been newly developed by Shimadzu Co. Ltd. [17]. It has a rectangular groove shape whereas the ruled grating has a triangular groove shape. The holographic grating is manufactured using holographic technique through chemical process. The flat-field spectrometers with laminar-type holographic gratings have been developed through the present thesis for the further improvement on the spectral characteristics.

Molybdenum and tungsten have been considered as a candidate for the plasma facing material in ITER. The spectroscopic study on the high-Z impurities becomes important in the next generation fusion device. The spectral lines of the high-Z elements, however, have not been well investigated until now. Any exact wavelengths have not been determined even now. Most of the spectral lines from such highly ionized high-Z impurities are emitted in EUV and soft X-ray ranges. Extensive study is necessary on the line analysis of high-Z elements in addition to theoretical work based on atomic physics. On the other hand, $n=3-2$ transitions from partially L-shell ionized medium-Z impurities ($16 < Z < 27$) emitted in the 10-30Å range are very useful to impurity diagnostics, since the charge state distribution can be easily measured from the transition array. The spectral line structure of the transition has not been actively studied until now mainly due to the technical difficulty. The emission spectra in such a short wavelength range can be successfully measured using flat-field spectrometer because of its wider wavelength

interval with good spectral resolution in comparison with the conventional grazing incidence and crystal spectrometers [12, 18].

In helical devices, such as Large Helical Device (LHD) [19], the edge magnetic fields are intrinsically stochastic and the edge plasma is then characterized by the presence of thick stochastic magnetic field structure surrounding the plasma core, which is called ergodic layer [20]. The particle transport parallel to the magnetic fields becomes important in the ergodic layer as well as the transport perpendicular to the magnetic fields. It is reported that the parallel particle transport can lead to the reduction of impurity influx [21]. Recently in several tokamaks, the effect of the stochastic magnetic fields has been extensively studied using perturbation field supplied by external magnetic field coils in relation to edge localized mode (ELM) [22]. In Tore Supra tokamak, a significant reduction of the intrinsic impurity amount was found by the activation of ergodic divertor [23]. Reduction of highly ionized carbon has been also observed during ergodic divertor operation in TEXTOR [24]. This unique edge impurity behavior can be explained by the competition among several forces directly affecting the parallel particle motion [25].

In LHD the magnetic field structure of the ergodic layer can be well calculated, whereas the estimation of the stochastic magnetic field structure is not so simple. The magnetic field structure in the ergodic layer can be easily modified by changing the coil currents of LHD, which give large freedom for formation of the magnetic field configuration. The local island divertor (LID) coils can also control $m/n=1/1$ island width at plasma edge. The study of the edge impurity transport in the ergodic magnetic fields is significantly important further to understand the physical mechanism.

1.4. LHD and relevant diagnostics

Physical parameters of LHD are as follows;

Major radius: $3.5 \leq R \leq 4.1$ m (standard: $R=3.6$ m)

Average minor radius: $a=0.6$ m at $R=3.6$ m

Magnetic field strength at plasma center: $B_0 < 3.0$ T

Plasma volume: $V_p=30$ m³ at $R=3.6$ m.

Magnetic surface for confinement is formed by a pair of $l/m=2/10$ continuous helical and three pairs of poloidal coils, where l and m are the poloidal and toroidal pitch numbers. All the coils are made of superconductor. A cross sectional view of LHD is shown in Fig.1.1. The pairs of outer vertical (OV), inner vertical (IV) and inner shaping (IS) coil are seen in the figure. Ten pairs of local island divertor (LID) coils made of normal conductor are also set at the top and bottom ports of all vertically elongated plasma cross section. Helical coils (HC) produce the elliptical magnetic surface in LHD and the strong vertical field produced by HC is necessarily cancelled by OV coils. The position of the plasma axis, which can significantly determine the fundamental nature for confinement, is changed by the vertical field from the OV and IV coils. The shape of the elliptical plasma can be modified by the quadrupole field from the IS coils. The LID coils are mainly used for the cancellation and expansion of $m/n=1/1$ island, where m and n are poloidal and toroidal mode number.

In LHD the divertor structure is intrinsically formed seen in Fig.1.1 [26]. Divertor tiles are made of carbon, which is a major impurity in LHD at present. The vacuum vessel is made of stainless steel and the wall conditioning is normally done by He glow discharge. Boronization and titanium gettering are occasionally carried out according to the experimental purpose. Thick stochastic magnetic field lines region known as ergodic layer exist at outside of last closed flux surface (LCFS). Detailed feature of the ergodic layer is discussed in section 4.2.

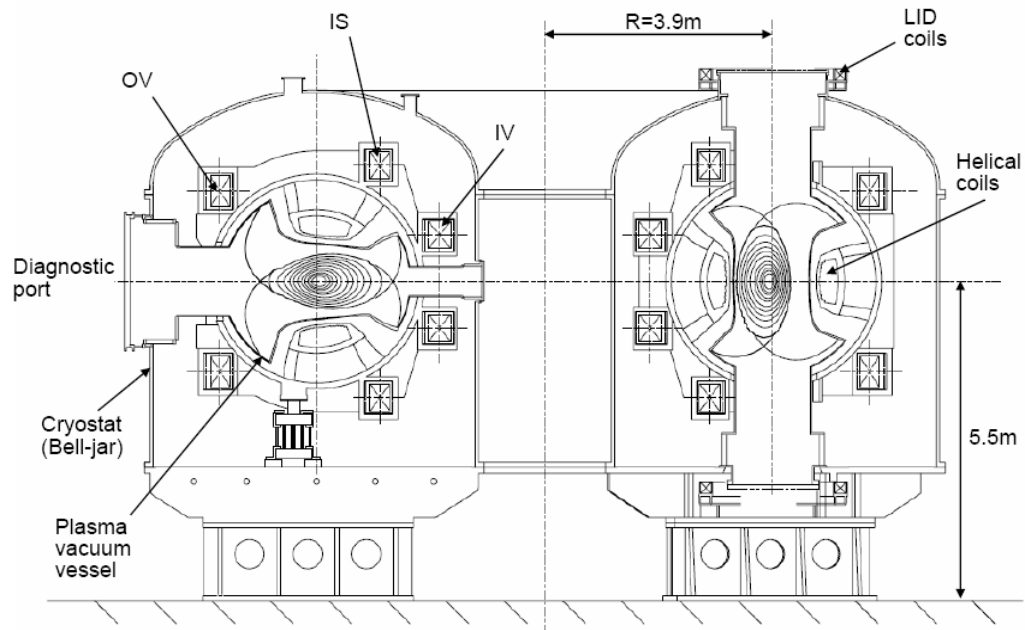


Fig. 1.1 Cross sectional view of LHD with magnetic field structure, coils position, vacuum vessel and cryostat.

A discharge is generally initiated by electron cyclotron heating (ECH) [27] and sustained by three negative ion based neutral beam injection (NBI) [28]. The discharge can be also initiated by NBI itself. Total ECH power produced by three gyrotrons at the characteristics frequencies of 84, 82.6 and 168 GHz. is $\sim 2.0\text{MW}$. Ion cyclotron resonance heating (ICRH) is mainly used for steady-state operation with total power of $\sim 2.7\text{MW}$ in maximum using 6 antennas. Three NBIs undertaking the main heating in LHD are aligned for tangential injection. The heating power of each beam is $\sim 4\text{--}5\text{MW}$ at energy of 180keV . Recently a low-energy beam based on positive ion is installed as a perpendicular injection.

LHD diagnostics [29] have been designed by the following key issues;

- (a) Multi-dimensional (2- or 3-dimensional) measurement to study non-axisymmetric toroidal plasma
- b) Diagnostics in the steady state operation.

The main physics issues considered during the design are as follows;

- (a) Energy and particle transports in LHD magnetic field configuration,
- b) Magnetohydrodynamic (MHD) equilibrium and stability,

- (c) Characteristics of the helical divertor, and
- (d) Confinement of energetic particles.

The main diagnostics are listed in Table 1.1. Here, the diagnostics relevant to the present work are briefly described.

Table 1.1 LHD plasma diagnostics

Diagnostics	Measurements
Magnetic probe	I_p, W_p
2mm interferometer	line-averaged electron density ($\langle n_e \rangle$)
FIR laser interferometer	$n_e(r)$
microwave reflectometer	n_e fluctuation
Thomson scattering	$T_e(r), n_e(r)$
Electron cyclotron emission (ECE)	$T_e(r)$
X-ray pulse height analyzer (PHA)	T_e , impurities
TOF neutral particle analyzer	T_i , ion energy spectrum $f(E)$
Charge exchange spectroscopy (CXS)	$T_i(r)$, plasma rotation ($V_p(r), V_t(r)$)
X-ray crystal spectroscopy	T_i, V_t
Bolometer	$P_{rad}(r)$
VUV and EUV spectroscopy	impurity, T_i
Visible spectroscopy	impurity, $n_0(H), Z_{eff}$
Soft X-ray diode array	MHD
CO ₂ laser scattering	micro-instability
Heavy ion beam probe (HIBP)	$\Phi_p(r), \Phi_p$ fluctuation
Langmuir probe	edge T_e, n_e, Φ_p
Divertor spectroscopy	recycling, particle influx
Li beam probe	n_e fluctuation
High energy particle diagnostics	fast ion energy spectra
visible/infrared camera	plasma-wall interaction

Spectroscopic diagnostics covering visible to X-ray ranges have been installed to monitor and study the impurity behavior in LHD plasmas [30]. Visible diagnostics consist of two 50cm UV-visible spectrometers, one 1.33m visible spectrometer, Z_{eff} profile measurement system, H_α and HeI monitors in visible range. One of the 50cm visible spectrometers has three gratings of 100, 1800 and 3600grooves/mm and another one has 150, 600 and 1200grooves/mm gratings. These two spectrometers can simultaneously observe the visible spectra from 26channels. The visible spectrometer

with 1.33m focal length has aberration-corrected mirror system and a grating of 1800grooves/mm with a reciprocal linear dispersion of 0.3nm/mm. This system creates extremely good spectral resolution and measures detailed spectral line profiles. Array of 100 optical fibers is used to transfer the visible light. Visible bremsstrahlung profile for Z_{eff} measurement is installed with a combination of 84 optical fibers (a core diameter: 300 μm), 80 photomultipliers and an interference filter having a center wavelength of 5215 \AA [31]. Recently, visible spectrometer for Z_{eff} profile measurement is also installed with 100 optical fibers (a core diameter: 100 μm).

VUV and EUV spectroscopy include an impurity monitor station consisting of three 20cm normal incidence spectrometers (300–2000 \AA) and five 20cm normal incidence monochromators, a 2.2m grazing incidence monochromator (100–1200 \AA), H α and HeI monitors, total radiation monitor and a soft x-ray monitor. The 20cm monochromators equipped with secondary electron multiplier (SEM) tubes observe the emissions from spectral lines of L $_{\alpha}$ (1215 \AA), CIII (977 \AA), CIV (1548 \AA), OV (630 \AA), and OVI (1031 \AA). The grazing incidence monochromator is routinely used to monitor the FeXVI (335 \AA) line. Radial profiles of edge impurity are measured by 3m VUV spectrometer with the use of view-angle adjustable mirrors set in front of an entrance slit and back illuminated CCD detector [32]. Two flat-field EUV spectrometers to cover 10–500 \AA , which is a part of the present study, is now completed and routinely used to observe the emission spectra from highly ionized impurities.

The X-ray pulse height analyzer with Si(Li) and Ge detectors is also installed to measure the heavy metallic impurity emission from the plasma core. Radial profile of line-integrated x-rays can be measured by scanning the line of sight of four Si(Li) detectors in a steady phase of LHD discharges [33]. A crystal spectrometer has been developed for the measurement of ion temperature and toroidal rotation velocity in the central part of LHD plasma using Doppler broadening and its shift of x-ray lines from He- and H-like Ar and Ti ions [34].

Electron temperature (T_e) and density (n_e) profiles are measured by Thomson scattering diagnostics [35] at a horizontally elongated plasma cross section. The backscattering system adopted as the Thomson scattering diagnostics observes the whole plasma region along a major radius (R) on the mid-plane under the severe port constraint

of the helical configuration. The system consists of 200 radial measurement points with a spatial resolution of 15–30mm, which depends on the radial position of laser scattering. The overall optical-electrical conversion efficiency can be very high by use of a large collection mirror (150×1.80cm), optical fibers with large core diameter (2mm), filter polychromators with high transmittance, avalanche photo detectors and Nd-YAG lasers (four 50Hz lasers: 0.5J/pulse, two 10Hz lasers: 2.5J/pulse). This high repetition system enables us to obtain high quality data of $T_e(r)$ and $n_e(r)$ of LHD. The spatial resolution in each point is very high due to the adoption of short scattering spatial length. The high repetition and high spatial resolution allow to observe the detailed information of magnetic islands seen in LHD magnetic surface [36]. The absolute value of the density is checked with line-integrated density measured by a 285GHz millimeter interferometer.

Electron density profile is also measured by 13 channels FIR laser interferometer at vertically elongated plasma cross section [37]. The FIR laser beam is generated by CH₃OH laser, which is pumped by CO₂ lasers, with a wavelength of 118.8 μ m. The frequency difference between the CH₃OH lasers for the probe beam and the reference beam is 1MHz. The power of CH₃OH laser is 150mW. Laser beam and optical components are enclosed and filled with dry air in order to reduce absorption by water vapor. A probe laser beam is split into 13 beams using beam splitter. The 13 probe beams pass through the LHD plasma vertically and are reflected back. Each probe beam is mixed with the reference beam and is detected by Schottky barrier diode. Thirteen beams can cover the whole region of the plasma with 90mm separation, while the laser beam width is about 50mm. The observed signal-to-noise ratio is 30–40dB/10kHz, and the phase fluctuation is approximately 1/100 fringes. Radial density profiles have been obtained with an Abel inversion technique. The observed density resolution is $4 \times 10^{17} \text{m}^{-3}$. Using its good temporal and spatial resolutions, particle diffusion coefficients are obtained with density modulation due to gas puffing [38].

Ion flux distribution is measured by an array of 16 dome-type Langmuir probes embedded in divertor carbon tiles and plasma stored energy is measured by diamagnetic loop in a usual way.

References

- [1] J. Wesson, *Tokamaks*, 3rd edition, Oxford University Press, (2004).
- [2] R. C. Isler, *Nucl. Fusion* **24**, 1599 (1984).
- [3] C De Michelis and M Mattioli, *Rep. Prog. Phys.* **47**, 1233 (1984).
- [4] P. C. Stangeby, *The Plasma Boundary of Magnetic Fusion Devices*, Institute of Physics Publishing, (2000).
- [5] X. Bonnin et al., *Suppl. Nucl. Fusion* **2**, 1028 (1992).
- [6] B. C. Stratton et al., *Phys. Rev. A* **31**, 2534 (1985).
- [7] R. Katai, S Morita and M. Goto, *Plasma Fusion Res.* **2**, 006 (2007).
- [8] B. C. Stratton et al., *Fusion Sci. Tech.* **53**, 431 (2008).
- [9] C. Jupen et al., *Physica Scripta.* **68**, 230 (2003).
- [10] K. Asmussen et al., *Nucl. Fusion* **38**, 967 (1998).
- [11] A. Thorne, U. Litzen and S. Johansson, *Spectrophysics*, Springer-Verlag, (1999).
- [12] W. L. Hodge et al., *Rev. Sci, Instrum.* **55**, 16 (1984).
- [13] J. A. R. Samson and D. L. Ederer, *Vacuum Ultraviolet Spectroscopy I*, Academic Press, (1998).
- [14] R. J. Fonck et al., *Appl. Opt.* **21**, 2115 (1982).
- [15] T. Kita et al., *Appl. Opt.* **22**, 512 (1983).
- [16] M. Koike et al., *Proceeding of SPIE* **4146**, 163 (2000).
- [17] M. Koike et al., *J. electron Spect. & Rel. Phenom.* **101-103**, 913 (1999).
- [18] I. Sakurai, Y. Tawara, C. Matsumoto, A. Furuzawa, S. Morita and M. Goto, *Rev. Sci. Instrum.* **77**, 10F328 (2006).
- [19] A. Iiyoshi et al., *Nucl. Fusion* **39**, 1245 (1999).
- [20] N. Ohyabu et al., *Nucl. Fusion* **34**, 387 (1994).
- [21] Ph Ghendrih et al., *Plasma Phys. Control. Fusion* **38**, 1653 (1996).
- [22] T. E. Evans et al., *Phys. Plasmas* **9**, 4957 (2002).
- [23] C. Breton et al., *Nucl. Fusion* **31**, 1774 (1991).
- [24] G. Telesca et al., *J. Nucl. Mater* **44**, 337 (2005).
- [25] Z. Tokar, *Phys. Plasmas* **6**, 2808 (1999).
- [26] N. Ohyabu et al., *J. Nucl. Mater.* **266-269**, 302 (1999).

- [27] S. Kubo et al., J. Plasma Fusion Res. **78**, 99 (2002).
- [28] O. Kaneko et al., Nucl. Fusion **43**, 692 (2003).
- [29] S. Sudo et al., Plasma Phys. Control. Fusion **45**, 1127 (2003).
- [30] S. Morita, M. Goto et al., Plasma Sci. Tech. **8**, 55 (2006).
- [31] H. Nozato, S. Morita, M. Goto et al., J. Plasma Fusion Res. Series **5**, 442 (2002).
- [32] S. Morita and M. Goto, Rev. Sci. Instrum. **74**, 2036 (2003).
- [33] S. Muto, S. Morita et al., Rev. Sci. Instrum. **72**, 1206 (2001).
- [34] S. Morita and M. Goto, Rev. Sci. Instrum. **74**, 2375 (2003).
- [35] K. Narihara et al., Rev. Sci. Instrum. **72**, 1122 (2001).
- [36] K. Narihara et al., Phys. Rev. Lett. **87**, 13002 (2001).
- [37] K. Kawahata et al., Rev. Sci. Instrum. **70**, 695 (1999).
- [38] K. Tanaka et al., Nucl. Fusion **46**, 110 (2006).

Chapter 2

Development of EUV spectrometers and their calibration

2.1. Spectrometer for 50-500Å (EUV_Long)

2.1.1. Introduction

Spectral emissions in the extreme ultra violet (EUV) wavelength range from magnetically confined high temperature plasmas can be used to estimate the radiation losses from impurities, to study the impurity transport phenomena, to understand the plasma-wall interaction and also to monitor over all discharge conditions [1]. The grazing incidence spectrometers with an array detector like micro-channel plate, photo diode array and charge couple device (CCD) detector are well served to these purposes due to the capability of providing spectral and temporal information simultaneously. Therefore, such spectrometers have been used in many tokamaks [1, 2] and other magnetically confined plasma devices [3, 4].

On the other hand, a flat focal plane is required in order to mount the multi-channel flat detectors. The flat focal plane has been recently achieved using a varied-line-spacing (VLS) grooves concave grating which focuses all diffracted rays onto the flat plane [5]. The use of the mechanically ruled VLS grating presents the same spectral resolution along the detector size and relatively easy alignment of the detector. When the VLS grating with 1200grooves/mm at the grating center is used, the flat-field EUV spectrometer measures a wavelength range of 50 to 500Å with good spectral resolution, which covers the important lines of partially ionized medium-Z impurities like Ne, Ar, Ti., Cr, Fe etc. These spectral lines mainly emitted from the plasma core can be considered as a local plasma diagnostics.

However, the line identification becomes frequently difficult, since so many lines closely exist in such a wavelength range. Furthermore, the 1st order original lines

overlap with many higher orders lines. It is well known that the holographic grating has a distinct advantage over the mechanically ruled grating from the standpoint of its ability to suppress overlapping higher orders light and to reduce the stray light level [6]. Recently, the VLS laminar-type holographic grating with flat-field focal plane has been newly developed by Shimadzu Co. Ltd [7, 8].

At first, the EUV spectrometer with the mechanically ruled 1200grooves/mm grating was constructed to measure LHD plasmas. Next, the grating was replaced by the VLS holographic grating to compare the spectral resolution and sensitivities between the two gratings. The relative sensitivities have been determined using EUV continuum radiation. The absolute sensitivity calibration is done with the combination of the EUV continuum and the branching ratio [9] of CIV lines (3p-3s: 5800Å/3p-2s: 312Å). In this section the comparison of the EUV spectrometer characteristics between the ruled and holographic gratings is presented with detailed technical explanations of the spectrometer. A new technique for the absolute calibration applied to the holographic grating EUV spectrometer is also presented.

2.1.2. Details on 1200grooves/mm flat-field EUV spectrometer

A schematic drawing of a flat-field EUV spectrometer is shown in Fig.2.1. It consists of a fixed entrance slit of 30µm width, a gold-coated concave VLS grating and CCD. Several masks are placed in front of the grating and at the back side of the grating to reduce the impinging scattered light. An electrical insulator is placed between the detector and the spectrometer. A pulse motor is used for the movement of the CCD detector along the focal plane to change a wavelength range to be measured. A laser light can be focused on the grating center as a zero-th order light to align the spectrometer view axis. The spectrometer is evacuated by a magnetically floating turbo molecular pump. The pressure of the spectrometer is generally kept in the order of 10^{-8} torr. A back-illuminated CCD (Andor DO420-BN) is used as a detector. The size of the CCD is 26.6×6.6mm² with a pixel size of 26×26µm² and the number of channels of 1024×255. Data are transferred with a time interval of 5ms in full vertical binning mode. An upper

half of the CCD is masked by a rectangular slit to reduce the EUV emission intensity. A mechanically ruled VLS 1200grooves/mm gold-coated grating (Hitachi 001-0266) is set up as the first step of the present study. The effective area of the grating is 26mm in groove length and 46mm in grooves distance. A blaze angle and wavelength are 3.2° and 1000\AA , respectively. The spectrometer was installed on a radial port perpendicular to the toroidal magnetic field of the LHD through a bellow flange at a distance of 9m from the plasma center.

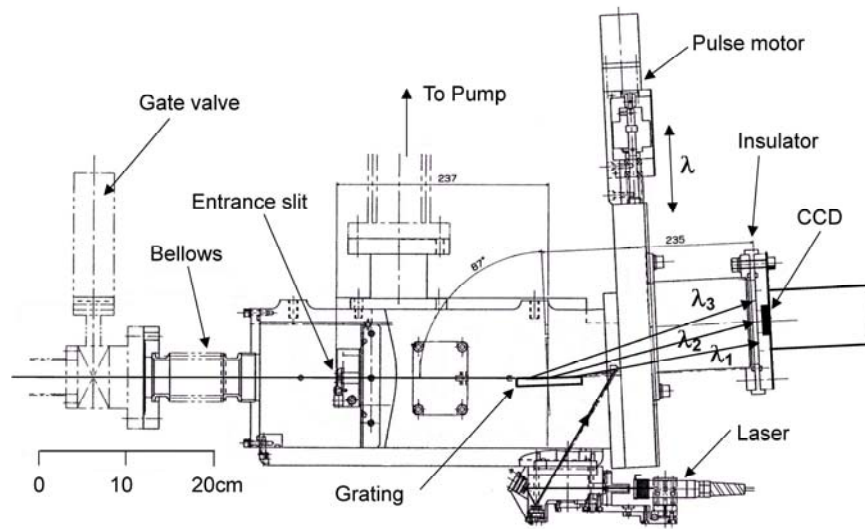


Fig. 2.1 Details of EUV flat-field spectrometer.

A schematic design specification of the EUV spectrometer is illustrated in Fig.2.2. Details of the grating design have been reported in different papers [4, 5, 10]. The 1200grooves/mm VLS concave grating covers a wavelength range of 50 to 500\AA at an angle of incidence of $\alpha=87^\circ$. A radius of curvature is 5649mm, then the distance between the grating center and the entrance slit is 237mm and the distance between the focal plane perpendicular to the grating surface and the grating center is 235mm. The angle of diffraction, β , determines the wavelengths to be measured.

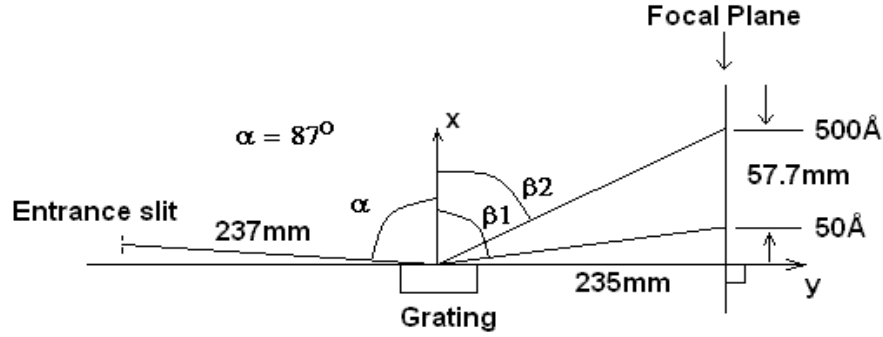


Fig. 2.2 Schematic diagram of EUV flat-field spectrometer with its parameters.

Focal curves at the detector position are calculated as a parameter of the angle of incidence, as shown in Fig.2.3. The x-y coordinate is indicated in Fig.2.2. The calculation is done in relation to the total light path for the mechanically ruled aberration corrected concave grating. The light path function [10] can be written as a power series of the groove coordinate and is then expressed as

$$F_{ij} = C_{ij} + [(m\lambda)/\sigma_0]M_{ij} , \quad (2.1)$$

where C_{ij} is the usual term corresponding to the equally spaced straight grooves and M_{ij} the aberration-corrected term related to varied spacing curved grooves. The complete aberration free image can be obtained when each key term of the light path function is kept either zero or minimum. The first two terms related with dispersion of the grating and horizontal focal condition are given as

$$C_{10} = -\sin \alpha - \sin \beta , \quad (2.2)$$

$$M_{10} = 1 , \quad (2.3)$$

$$C_{20} = \frac{1}{2} \left(\frac{\cos^2 \alpha}{r} - \frac{\cos \alpha}{R} \right) + \frac{1}{2} \left(\frac{\cos^2 \beta}{r'} - \frac{\cos \beta}{R} \right) \quad (2.4)$$

and

$$M_{20} = \frac{1}{R} \left(b_2 - \frac{\tan \theta}{2} \right) , \quad (2.5)$$

where α and β are the angles of incidence and diffraction, respectively, σ_0 the nominal groove spacing, R the grating radius, m the diffraction order, λ the wavelength, r and r'

the incidence and diffraction radial distances, respectively, θ the grooves angle with respect to the normal of grating. The value of b_2 , which is a ruling parameter, corresponds to a flat focal condition, taken from Ref. 5. The $\tan\theta$ is assumed to be zero since the value of θ is very small. The two terms, F_{10} and F_{20} , are solved together for different lambdas and the angles of incidence to get the focal curves. It is seen from the figure that the focal condition varies abruptly with variation of the angle of incidence. However, only the focal curve for the angle of incidence of 87° gives an approximately good straight focal condition in the wavelength range of 100 to 300\AA . Therefore, the vertical line at $y=235\text{mm}$ shown in the figure indicates an exact position of the CCD detector. From the focal curve it could be clearly understood that the approximately determined linear focusing sharply drops below 50\AA . The linear focusing is also lost gradually at wavelengths above 300\AA .

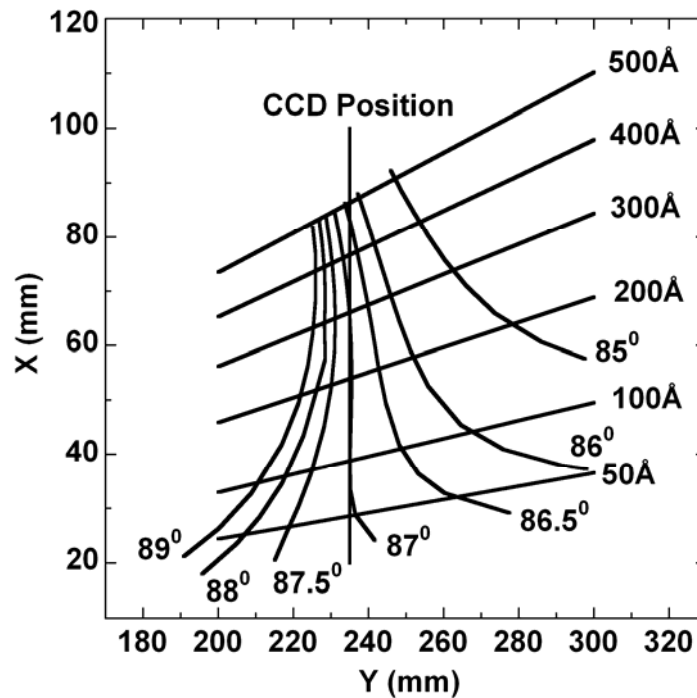


Fig. 2.3 Calculated focal curves as a parameter of angles of incidence. Positions of X and Y axes are indicated in Fig.2.2. A solid vertical line denoted with CCD position means a designed position of detector.

The most difficult and important point during the construction of the EUV spectrometer is setting of the grating angle. The exact position of the angle of incidence of the grating can be determined by checking the spectral resolution as a function of y-coordinate. For this purpose spectral emissions from the LHD plasmas were measured and the wavelengths were calibrated using well known emission lines from impurities like He, C and Ne. All spectra used to check spectral resolution were recorded with a full image mode in order to measure an exact spectral resolution avoiding an influence of the spectral line tilt.

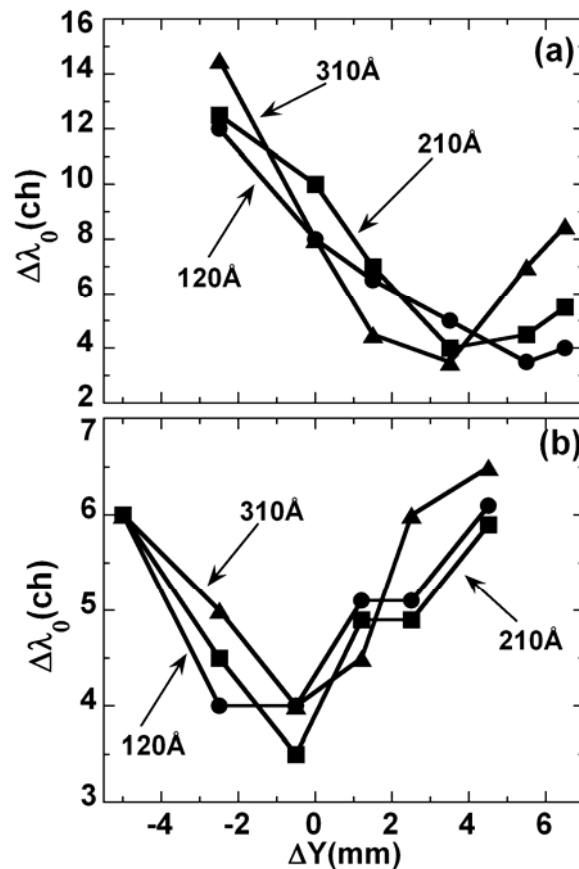


Fig. 2.4. Experimentally obtained spectral resolution $\Delta\lambda_0$ (full width at foot position of spectrum) (a) before and (b) after angle realignment of ruled grating as a function of distance from designed focal plane indicated in Fig.2.2. Data are plotted at three different wavelengths.

Figure 2.4 shows a plot of the full width at foot position of spectral lines, $\Delta\lambda_0$, as a function of displacement along the y axis. The position of $\Delta Y=0$ means the position of $Y=235\text{mm}$ expressed by the vertical line in Fig.2.3. The different values of ΔY are obtained by the use of insulator flange with different thicknesses. Data are plotted for typical three wavelengths of 120, 210 and 310Å. It is visible from Fig.2.4 (a) that the best focus position deviates from the regular position +5mm apart and the shorter wavelengths are focused at relatively larger Y coordinate. It indicates that the incidence angle is smaller than the designed value of 87°. Seeing Fig.2.3 we understand the true angle of incidence is 86.8°.

When the plot of Fig.2.4 (a) was obtained, we used a collimated laser light to adjust the angle of incidence of the grating. Then, we knew it was impossible to adjust the angle within an accuracy of 0.02–0.04°. The method to set the grating was changed to a new technique with a telescope. Two telescopes were set behind the detector position and the grating edge was monitored while translating and rotating the grating. The position of the grating was finally determined as a standard position of the entrance slit and grating center. This method excellently improved the accuracy of the grating angle setting. Figure 2.4 (b) shows the result after the realignment. The best focus position becomes identical for three wavelengths, close to the regular position. The spectral resolution of $\Delta\lambda_0$ is almost the same at different wavelengths with symmetric line shape. Thus, the alignment of the grating has been accurate enough and the CCD position has been also accurate within 0.5mm of the designed value.

The reciprocal linear dispersions are experimentally determined and compared with theoretical values, as revealed in Fig.2.5. The wavelength λ is given as a function of distance along focal plane (x-direction in Fig.2.2) by

$$m\lambda = \sigma_0(\sin \alpha + \sin \beta) \quad (2.6)$$

and

$$L = 235 \cot \beta, \quad (2.7)$$

where α , β , λ , m and σ_0 are as their usual meaning. The value of L is the distance along y-axis between the grating and focal plane. Using these two equations it is found that the theoretical reciprocal linear dispersion varies from 4.26 to 11.48Å/mm over the

corresponding wavelength range of 50 to 500Å. The total length in the spectral range is 57.7mm (see Fig.2.2). The angle of incidence on the focal plane of each spectral line varies from 6.96 to 20.18°. The experimental values expressed with closed circles are in a fairly good agreement with the calculated ones. For example, the dispersion is 7.62Å/mm at 200Å, which corresponds to 0.198Å/ch in the CCD image. However, there exists a very small discrepancy between them at longer wavelength side. The discrepancy is only 0.4Å/mm (0.01Å/ch) at 500Å and does not pose any problem in using the spectrometer. We believe that this discrepancy originated due to an angular deviation of the CCD detector from the designed focal plane. Small misalignment in the angle of incidence of the grating and the detector position will be other origins, which can give a little contribution to the error.

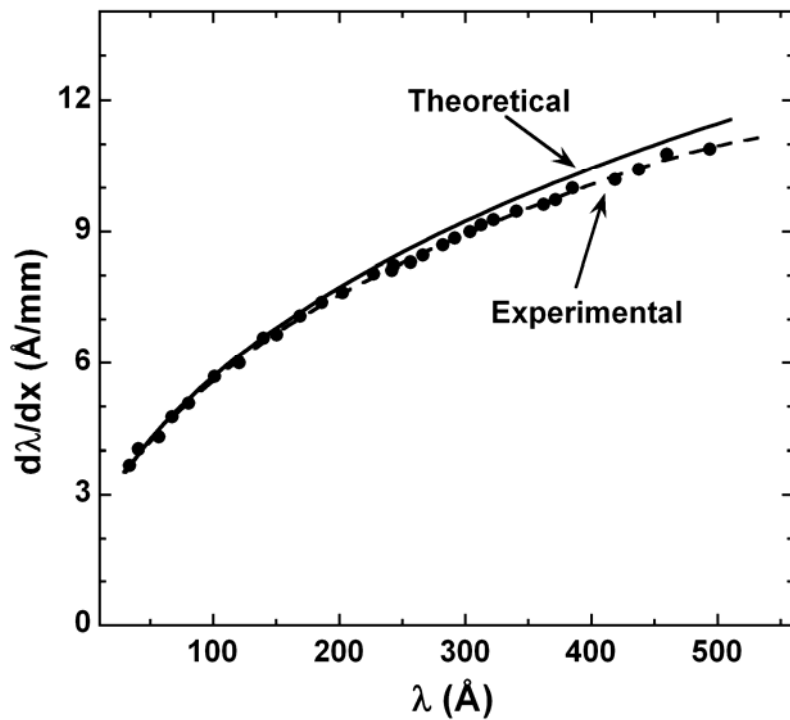


Fig. 2.5 Theoretical and experimental reciprocal linear dispersions as a function of wavelength. Experimental data are fitted with a dashed line.

2.2.3. Comparison between ruled and holographic gratings

The VLS laminar-type holographic grating [7, 8] having equivalent parameters to the ruled grating was mounted on the same spectrometer after removing the ruled grating for comparative study. The setting of the grating was performed to achieve the best resolution by the new method using the two telescopes as mentioned in the former section. In the present LHD discharges only the carbon is a main impurity because divertor plates are made of carbon. The amount of nitrogen is negligible except for the beginning of experimental campaign after long opening of the vacuum vessel, and the amount of oxygen is estimated to be less than 10^{-3} to the electron density.

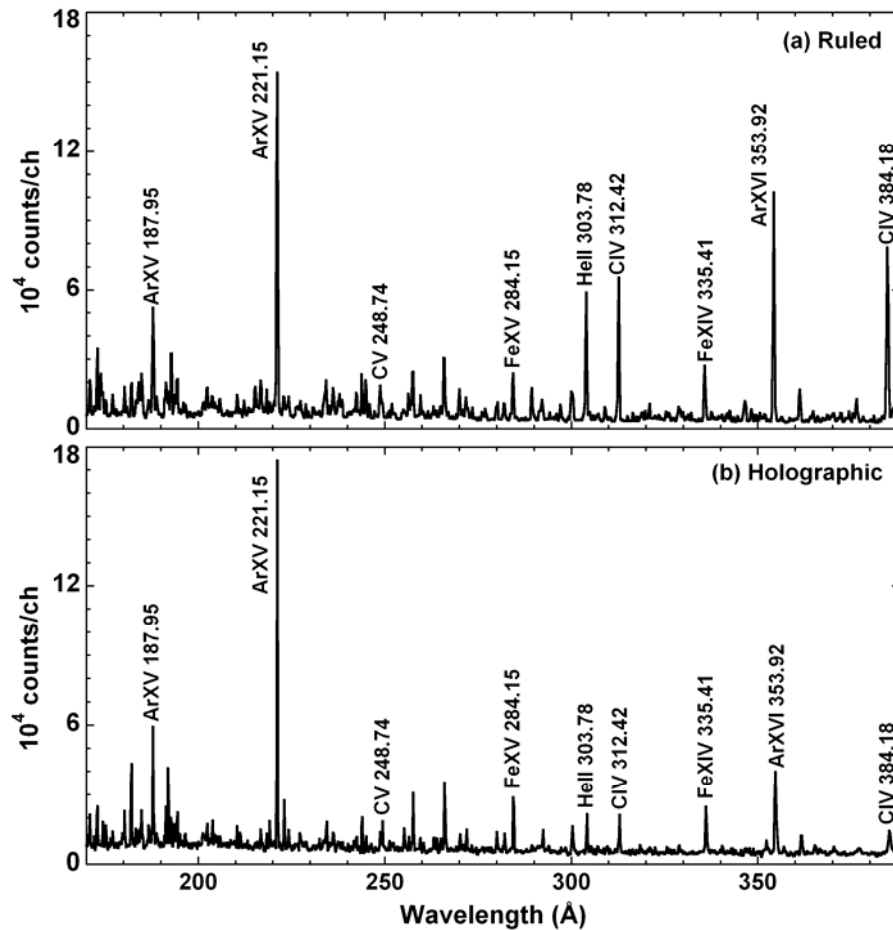


Fig. 2.6 Typical spectra with (a) ruled and (b) holographic gratings obtained from NBI-heated LHD discharges.

EUV spectra are observed from NBI-heated H₂ discharges in LHD. The exposure time per frame is 5ms and twenty frames are summed up to get better signal-to-noise ratio. The line-averaged electron density was around $4 \times 10^{19} \text{m}^{-3}$ in both discharges as measured by FIR interferometer diagnostics. Results are shown in Figs.2.6 (a) and (b) for ruled and holographic gratings, respectively. The spectrum from the holographic grating revealed in Fig.2.6 (b) is obtained after replacing the ruled grating by the holographic grating. Both spectra show resonance transitions of highly charged ions from carbon and iron which are the intrinsic impurity in LHD. The emissions from highly ionized argon are seen in the spectra. A small amount of argon is routinely puffed at beginning of discharges for the ion temperature measurement using a crystal spectrometer. The helium line originates in the helium glow discharge for vacuum wall cleaning. In this longer wavelength range of 170–390Å both spectra have no clear difference in relation to the spectral resolution.

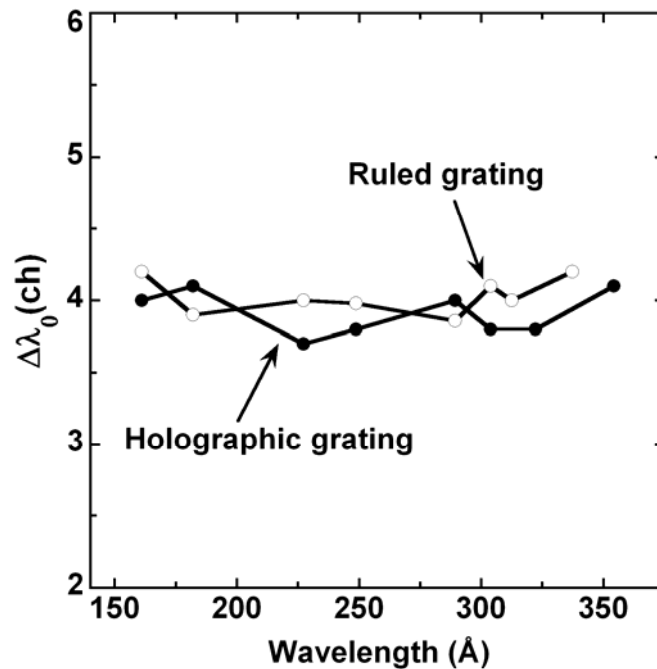


Fig. 2.7 Experimentally obtained spectral resolution $\Delta\lambda_0$ (full width at foot position of spectrum) for ruled and holographic gratings as a function of wavelength.

The wavelength dispersion and the spectral resolution for the holographic grating were also determined from the emission spectra of LHD plasmas. The same reciprocal linear dispersion as the ruled grating is, of course, confirmed. Figure 2.7 presents comparison of the spectral resolution $\Delta\lambda_0$ (full width at foot position) between the ruled and holographic gratings as a function of wavelength. It shows nearly constant $\Delta\lambda_0$ values of 4 channels independent of the wavelength for both gratings. Especially, the $\Delta\lambda_0$ of the 1st order line takes a value between 3.5 and 4.0 channels for the whole wavelength range in both gratings. The full width at half maximum (FWHM) of the spectral line, $\Delta\lambda$, estimated from a Gaussian fitting is 0.25Å at 192Å, which corresponds to 1.3 channels of the CCD detector. The Gaussian fitting of the spectral lines revealed unchanged spectral resolution across the detector, verifying that the spectral focus is certainly flat.

The capability of the two gratings was examined to check the contribution of the higher order light. The peak intensities of higher order light from CV (40.27Å), CVI (33.73Å) and FeXX (132.66Å) are plotted in Figs.2.8 (a) and (b) for ruled and holographic gratings, respectively. The relevant spectra are also shown in Figs.2.8 (c) and (d). The spectrum of Fig.2.8 (c) is measured during carbon impurity pellet injection in the LHD discharge and Fig.2.8 (d) is taken from a discharge with carbon limiter insertion in order to record higher carbon intensities. When the spectrometer is moved to the lower (upper) wavelength limit, the spectrum edge in longer (shorter) wavelength side is hidden behind the rectangular slit placed in front of the CCD, which is seen around 130–145Å (~100channels). In Figs.2.8 (a) and (b) all the intensities are normalized by their 1st order light. The second order light of CV from the holographic grating is only about 18 percent of the first order as shown in Fig.2.8 (b), whereas for the ruled grating the intensities from higher order light never decreases so quickly and maintains relatively strong intensities up to 8th order light, as revealed in Fig.2.8 (a). But the reduced second order light of CVI and FeXX in the ruled grating indicates a clear wavelength dependence on the higher order effect. This wavelength dependence is not evident for the holographic grating. Thus, the difference in the reflectivity of higher order light between the two types of the grating becomes very clear in the present work. This result confirms that the laminar-type holographic grating can suppress the higher order line spectra very efficiently compared with the ruled grating.

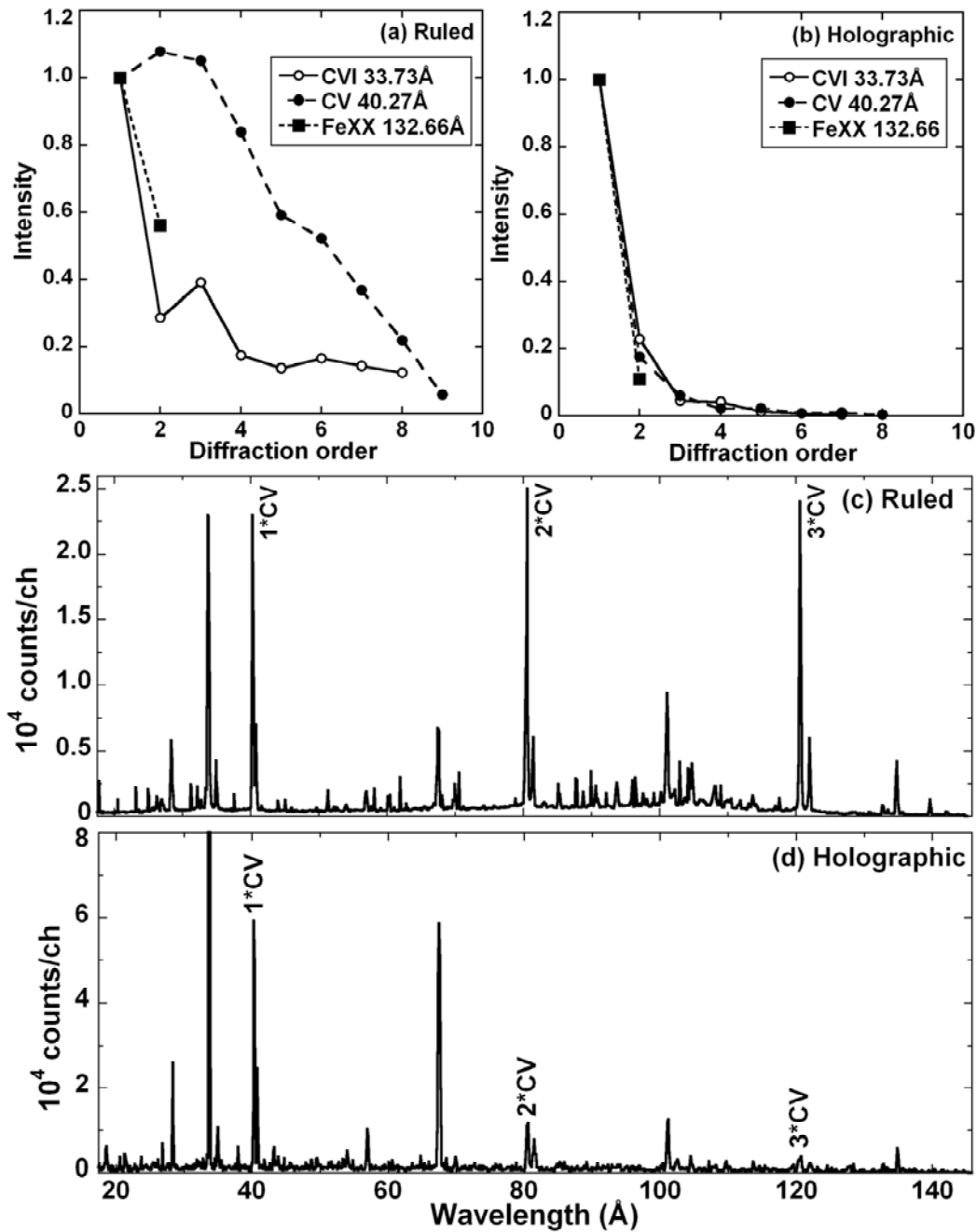


Fig. 2.8 Peak intensities of higher order light normalized to the 1st order light for (a) ruled and (b) holographic gratings. Raw spectra during carbon pellet injection and carbon limiter insertion are traced for (c) ruled and (d) holographic gratings, respectively, indicating higher order CV emissions.

2.1.4. Absolute intensity calibration

The conventional branching ratio method is a reliable technique to calibrate the EUV spectrometer absolutely. It determines an absolute emissivity of the vacuum ultra violet (VUV) spectral line using a branching pair of a VUV line and an absolutely calibrated visible line. Line emissions from partially ionized impurity ions from high-temperature plasmas have been used for the technique. Although several line pairs have been adopted so far for the absolute calibration, the line pair of 3p-3s/3p-2s transitions from lithium-like ions can give the simplest relation between the two transitions. However, the amount of impurities in recent magnetically confined plasmas has been greatly reduced because the vacuum wall was covered by carbon materials and an efficient discharge cleaning of the plasma facing component could be established. The status on the impurity content in LHD is also the same as other toroidal devices and the amount of low-Z impurities like nitrogen and oxygen and medium-Z impurities like chromium and iron are not normally visible. Therefore, it is difficult to get a sufficient number of lines pairs in order to fill a whole wavelength span of the spectrometer. Only the carbon emissions, however, became very strong since the divertor plates are made of carbon. The lithium-like ion of CIV, which has the strongest emission in VUV range, has been easily observed and could be successfully employed for the absolute calibration of our present instrument.

Recently, a relative intensity calibration of a high-resolution VUV spectrometer has been done using the continuum radiation in the field of astrophysics [11]. In this method a predicted free-free continuum radiation for an assumed electron temperature was compared with an experimental continuum. Then, a calibration curve against wavelength has been plotted from the ratio of the predicted to measured continuum intensities. The CCD detector used in the present study can be cooled by a Peltier device down to -70°C , and then the thermal noise is reduced to an extremely low level of 1count/sec/ch. The noise level is steady during a discharge. We can subtract the contribution of the noise from the raw data. Furthermore, the use of the holographic grating largely decreased the influence of the higher order light. The stray light in the EUV spectrometer is also completely deleted by setting many masks and slits. Thus, the

application of the continuum radiation from high-temperature plasmas to the spectrometer calibration can really give a very nice method also in the field of fusion plasma experiment. In fusion devices the electron temperature and density profiles have been measured from Thomson scattering diagnostic [12]. The continuum radiation can be accurately calculated from the measured profiles. The continuum radiation is generally composed of free-free radiation and free-bound radiation known as bremsstrahlung and radiative recombination, respectively. Here, the contribution from radiative recombination could be ruled out as the LHD plasma has a very high core electron temperature ($\geq 2\text{keV}$) and a relatively high edge temperature ($\geq 200\text{--}500\text{eV}$) at last closed flux surface in the moderate electron density range ($2\text{--}3 \times 10^{19}\text{m}^{-3}$). The free-free radiant flux [13] can be expressed as

$$E_{\lambda} = 1.89 \times 10^{-28} \frac{Z_{\text{eff}} n_e^2 g_{\text{ff}}}{T_e^{1/2} \lambda^2} \exp\left(-\frac{12400}{T_e \lambda}\right) [\text{W.cm}^{-3} \cdot \text{\AA}^{-1}], \quad (2.8)$$

where n_e is the electron density in cm^{-3} , Z_{eff} the effective ion charge, T_e the electron temperature in eV, g_{ff} the free-free gaunt factor and λ the wavelength in \AA . The free-free continuum in LHD has been usually measured in the visible and x-ray ranges in order to calculate the Z_{eff} [14] value and the electron temperature [15]. Reproducible discharges with a similar electron temperature and density were selected to scan the whole detectable wavelength range as the spectrometer covers only 200\AA at a time. Data obtained in every 5ms are accumulated to take a good signal-to-noise ratio and the final data were summed up ten temporal frames. The experimentally obtained continuum counts were compared with calculated values as a function of wavelength, which are integrated along the line-of-sight under considerations of the electron and density profiles. The experimental and calculated continuum radiations are shown for the ruled and holographic gratings in Figs.2.9 (a) and (b), respectively. The calculated continuum radiation traced with solid lines, which is normalized to the measured continuum at 312\AA , increases with decreasing wavelength because the electron temperature is high. However, the measured continuum for the ruled grating decreases with decreasing wavelength (see Fig.2.9 (a)). It means that the reflectivity of the ruled grating quickly decreases at shorter wavelength range, at least lower than 200\AA . In the holographic grating, on the contrary, the measured continuum radiation shows a similar tendency to the calculated one (see

Fig.2.9 (b)), although the experimental data in Fig.2.9 (b) are relatively scattered because of the limited number of discharges which are suitable to spectrometer calibration. The relative sensitivities of the conventional ruled grating and the newly developed holographic grating can be obtained from those data, as shown in Fig.2.10. Both data are also normalized at 312Å. The relative sensitivity is almost flat against the wavelength for the holographic grating, whereas it sharply reduced below 200Å for the ruled grating.

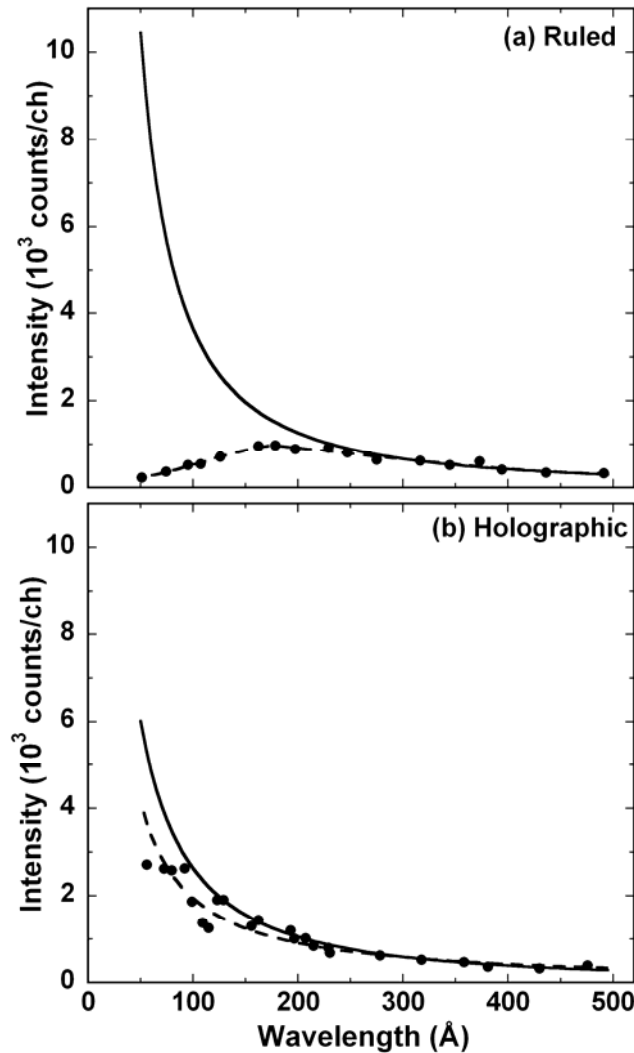


Fig. 2.9 Experimental EUV continuum line integrated intensities (solid circles) with fitting curve (dash line) and estimated EUV continuum (solid line) as a function of wavelength for (a) ruled and (b) holographic gratings.

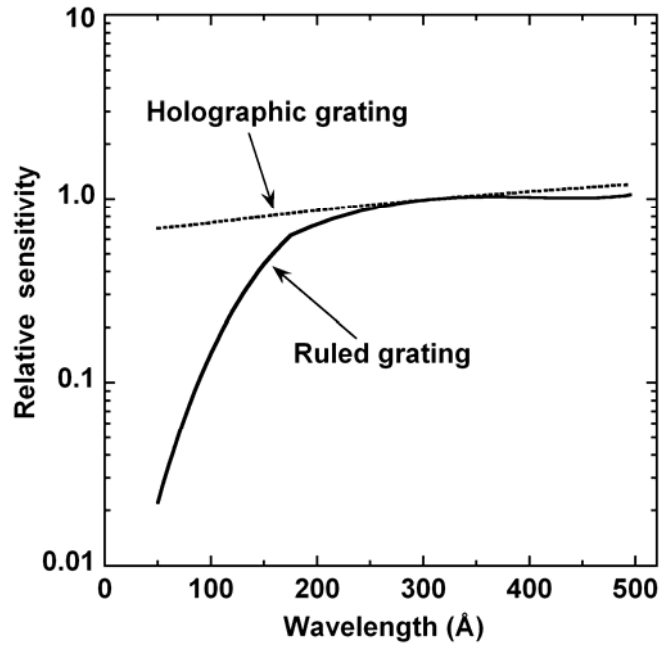


Fig. 2.10 Variation of relative sensitivities as a function of wavelength for ruled and holographic gratings.

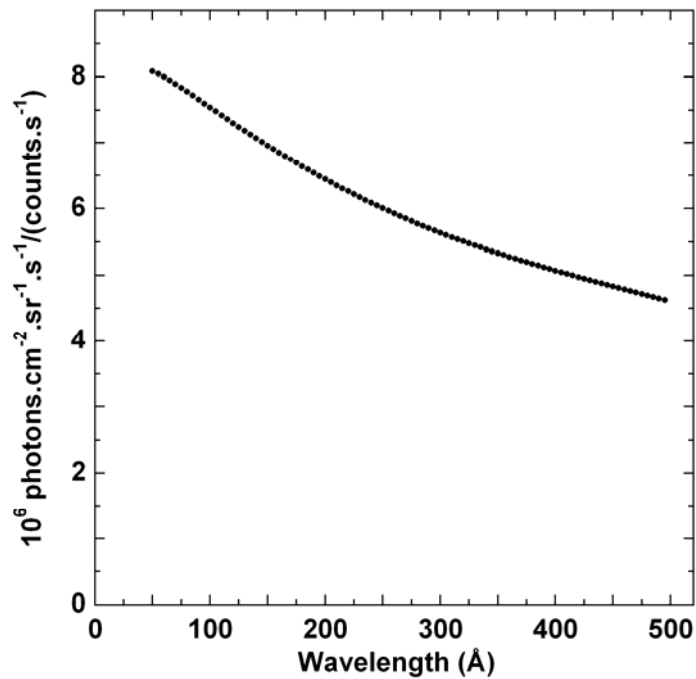


Fig. 2.11 Inverse absolute sensitivity of holographic grating EUV spectrometer as a function of wavelength.

In order to obtain the absolute sensitivity of the EUV spectrometer with the holographic grating the branching ratio method has been applied to the result of the relative sensitivity calibration mentioned above. The branching pair of visible doublet of 5801.33Å ($3p^2P_{3/2}-3s^2S_{1/2}$) and 5811.97Å ($3p^2P_{1/2}-3s^2S_{1/2}$) to EUV doublet of 312.42Å ($3p^2P_{3/2}-2s^2S_{1/2}$) and 312.45Å ($3p^2P_{1/2}-2s^2S_{1/2}$) lines was used in CIV Li-like ionic sequence. The transition probability values have been taken from online NIST atomic database [16]. These values are 3.17×10^7 and $4.63 \times 10^9 \text{s}^{-1}$ for visible and EUV transition, respectively. The visible lines absolutely calibrated with a standard tungsten lamp are measured by a 50cm visible spectrometer with an 1800grooves/mm grating and a CCD detector. The two visible lines of CIV 5801.33Å and 5811.97Å are well resolved and fitted by a Gaussian profile to calculate the total counts of the lines. The contribution of the background counts and their nearby lines is eliminated from the raw data. The CIV doublet of 312.42Å and 312.45Å in the EUV range can not be resolved because of the low spectrometer resolution. The inverse absolute sensitivity of the EUV spectrometer is thus obtained in combination with the branching method and the free-free continuum radiation measurement, as shown in Fig.2.11. The absolute intensity of the EUV emissions can be easily recorded by multiplying the CCD counts by the inverse sensitivity of the figure. The advantage of this method is that the sensitivity curve can be obtained continuously against the wavelength, whereas the branching method gives only scattered values. This method is also applicable to high temperature plasmas with low impurity content.

2.1.5. Summary

Spectroscopic characteristics of newly developed 1200grooves/mm holographic grating used for a flat-field EUV spectrometer, which covers a wavelength range of 50–500Å, have been studied by comparison with a conventional 1200grooves/mm ruled grating. The incidence angle of the grating, critical for optimum spectral resolution, can be accurately determined by moving the CCD detector position and checking the spectral resolution with theoretically calculated focal curves. The best resolution obtained for

both gratings with above method was quite good (e.g., $\sim 0.24\text{\AA}$ at 200\AA) to resolve emitted line spectra reasonably. However, the holographic grating can sufficiently suppress higher order spectra in comparison with the ruled grating.

The free-free continuum radiation has been applied to find the relative sensitivities of the EUV spectrometer. It has been found that the sensitivity of the ruled grating deteriorates at a wavelength lower than 150\AA , but the holographic grating indicates a constant sensitivity against the wavelength. The spectral characteristics of the holographic grating, such as extremely weak higher order emission contribution and high sensitivity at lower wavelength range, which became clear in the present study, was suitable to achieve absolute sensitivity calibration using the bremsstrahlung continuum. The EUV spectrometer with the holographic grating is thus absolutely calibrated with a combination of the bremsstrahlung continuum and the branching ratio technique using CIV lines which is used for determination of the absolute value in the present sensitivity calibration. As a result, the absolute calibration curve was obtained continuously against the wavelength. It could be an excellent alternative to overcome the large uncertainty on the wavelength dependence in typical absolute intensity calibrations measured discretely against the wavelength.

2.2. Spectrometer for 10-130Å (EUV_Short)

2.2.1. Introduction

Plasma radiation emitted in the wavelength range of 10 to 130Å plays an important role towards the core radiation loss from high temperature fusion plasmas [17]. This wavelength range contains strong resonance line emissions from H- and He-like ions of low-Z intrinsic impurities like boron, carbon and oxygen. The element of boron is generally introduced by boronization as a vacuum wall conditioning technique, while the carbon and oxygen are the intrinsic impurities released from metallic vacuum wall and divertor plates made of carbon in the fusion devices. It also contains line emissions from highly ionized medium- and high-Z impurities, e.g., iron and tungsten. The tungsten is now considered as a candidate of plasma-facing components in the next-generation fusion device. On the other hand, in the Large Helical Device (LHD), which has a central electron temperature around 2–3keV in NBI (neutral beam injection) discharges, line emissions from H- and He-like ions of carbon mainly released from carbon divertor plates significantly contribute in the total radiation loss. Another intrinsic impurity, i.e., iron, sometimes appears according to the operation scenario. The extrinsic impurities like neon, argon, titanium, molybdenum and tungsten etc. are also injected into the LHD plasma using methods of gas puffing and impurity pellet injection [18, 19] to study the characteristics of high-Z discharges [20, 21] and the spectral structure of such elements [22–24]. The highly ionized spectrum emitted from such medium- and high-Z impurities frequently forms a very complex spectral structure in the extreme ultraviolet (EUV) range of 10 to 130Å.

Therefore, the development of an EUV spectrometer having good spectral resolution and minimal irregular scattered stray light is required to measure and identify such spectral lines. In this context, a flat-field EUV spectrometer with a varied-line-spacing (VLS) grooves ruled grating has been developed to observe the wavelength range of 10 to 130Å. Higher order line emissions also make difficult the identification of the line spectra. On this basis, a very recently developed laminar-type holographic grating [7], which possesses the capability to suppress the higher order line emissions and stray

light [25], has been later replaced instead of the ruled grating for the comparative study. The relative sensitivity has been evaluated by comparing between the experimentally obtained continuum and calculated bremsstrahlung continuum using measured n_e and T_e profiles. The absolute intensity calibration is done at longer wavelength side of 90 to 120Å by comparing with line emissions from another absolutely calibrated EUV spectrometer with 1200grooves/mm grating [26].

In this section the development of a flat-field EUV spectrometer having the 2400grooves/mm grating has been described and the result on the comparative studies of the spectral characteristics on ruled and holographic gratings have been explained. Details on absolute intensity calibration are also presented.

2.2.2. Details on 2400grooves/mm flat-field EUV spectrometer

The present EUV spectrometer, which is called EUV_Short, aimed at the spectroscopic measurement in the wavelength range of 10 to 130Å has been principally developed to monitor closely existing spectral lines from high temperature fusion plasma. The spectrometer consists of a fixed entrance slit having 30µm in width, a gold coated concave VLS 2400grooves/mm grating and linear-imaging detector. A laser light, which can be passed through grating center as a zero-th order light, is attached to align the line of sight of the spectrometer. The amount of impinging scattered light is reduced by placing several masks in front and back sides of the grating. The detector has been mounted to the spectrometer through an electrical insulator and can be moved using a pulse motor along the focal image plane to change the detectable wavelength range. A back-illuminated vacuum ultraviolet (VUV) sensitive charge coupled device (CCD) (Andor DO420-BN) is adopted as the detector. The size of the CCD is 26.6×6.6mm² with 1024×255pixels and each pixel size is 26×26µm. It can be cooled down -70°C using Peltier device. The thermal noise is then reduced to an extremely low level of 1count/sec/channel in the full vertical binning mode. The upper half of the CCD is masked by a rectangular slit to reduce the amount of EUV intensity and increase the time resolution. The spectrum has been taken at every 5ms in the full vertical binning mode.

The spectrometer has been installed on a horizontal port perpendicular to the toroidal direction of the LHD through a bellow flange and gate valve at a distance of 9m from the plasma center. It is evacuated up to the order of 10^{-8} torr by a magnetically floating turbo molecular pump.

At first, a mechanically ruled gold coated VLS concave grating (Hitachi 001-0471) was installed inside the spectrometer for the present study. The schematic drawing and design specifications of the EUV spectrometer are shown in Fig.2.12. The radius of grating curvature, nominal spacing at grating center and angle of incidence (α) are 15920mm, 2400grooves/mm and 88.65° , respectively. The effective ruled area of the grating is 46mm in ruled width and 26mm in ruled height. The blaze angle and wavelength are 1.9° and 300\AA , respectively. The nominal groove density of 2400grooves/mm permits wavelength coverage of 10 to 130\AA as indicated in Fig.2.12. The distance of the entrance slit to the grating center is 237mm. The variable line spacing of the grating can focus the image onto a flat focal plane at a distance of 235mm perpendicular to the grating axis. The angle of incidence on the focal plane varies from 4.19 to 14.41° for the 10 to 130\AA range. The CCD is mounted on a precision translation stage set at the focal plane. The stage can be moved by the pulse motor in the interval of $X=17.2$ to 60.4mm , which corresponds to the wavelength interval of 10 to 130\AA .

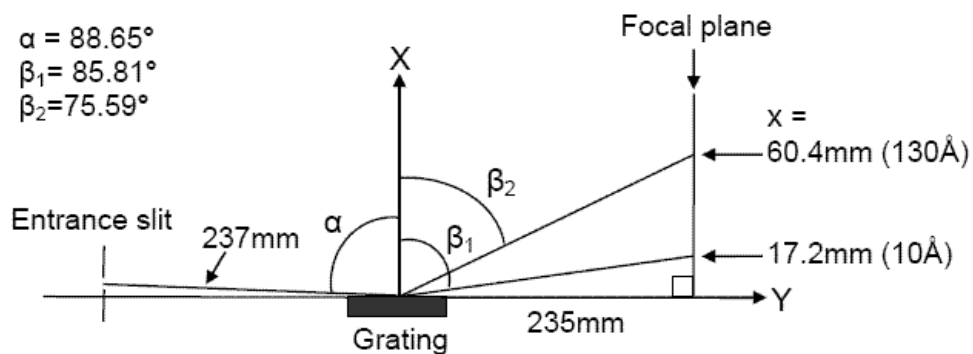


Fig. 2.12 Schematic drawing and design specifications of 2400grooves/mm EUV flat-field spectrometer.

The focal curves calculated for the aberration corrected VLS concave grating having 2400 grooves/mm at grating center are illustrated in Fig.2.13. The curves are drawn as a parameter of angle of incidence ($=\alpha$) in Fig.2.12. This graph clearly indicates that the focal condition is changed abruptly with the angle of incidence, but a flat focal region with an excellently focused image does exist at the wavelength range of 20 to 100Å for $\alpha=88.65^\circ$ at $Y=235$ mm. The exact CCD position is then shown in the figure by a solid vertical line at $Y=235$ mm. The wavelength in 100 to 140Å can be observed with a slightly defocused spectral image, as shown in Fig.2.13. The calculation also suggests that the spectral image focusing is not worse even in 10 to 20Å range. The precise grating position and angle alignments, which are very important to achieve the best resolution, were done using a technique with telescopes as mentioned in [26].

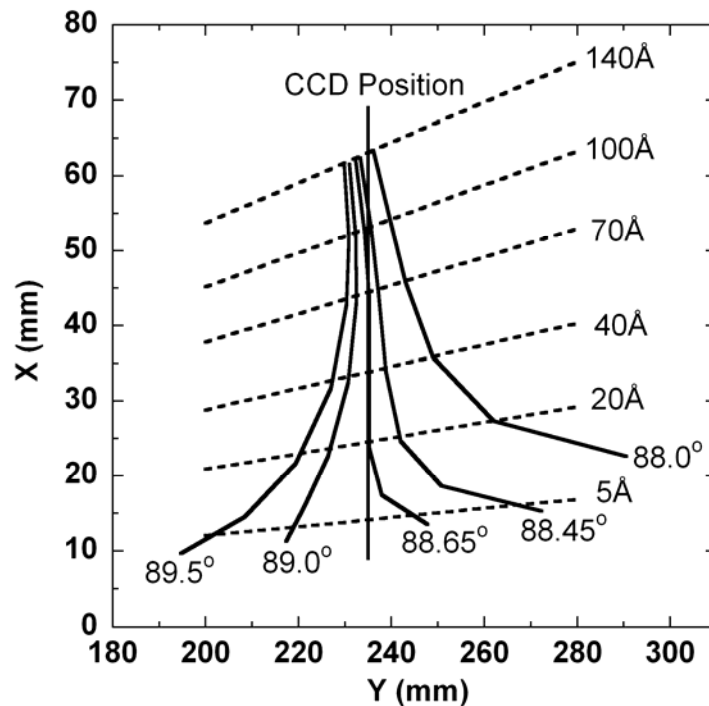


Fig. 2.13 Calculated focal curves (solid lines) of 2400grooves/mm VLS concave grating as a parameter of angle of incidence. Focal curves denoted with each incidence angle are indicated by solid curves. Definition of vertical (X) and horizontal (Y) axes is shown in Fig. 2.11. Solid vertical line denoted with CCD position indicates design position of linear image focus. Dashed lines indicate the wavelength position denoted with each wavelength in Å.

The reciprocal linear dispersions are experimentally determined and compared with calculated ones, as plotted in Fig.2.14. Experimental reciprocal dispersion ($d\lambda/dx$) is evaluated using emission lines from LHD plasmas. Experimentally obtained values are plotted with closed circles and fitted with a dashed line. The 4th order polynomial is used for the fitting curve. The dispersion varies with the wavelength, e.g., 1.28 and 4.29Å/mm at 10 and 130Å for the first order light, respectively. A fairly good agreement is seen between the experimental and calculated curves. The experimental curve, however, slightly deviates from the calculated curve at longer wavelength side. This deviation is very small, i.e., 0.07Å/mm at 130Å. It does not give any serious influence to the practical use of the spectrometer, because the deviation is smaller than single channel of the CCD. We believe that this deviation mainly arises from the small angular deviation of the CCD meaning the displacement from the designed position. Small misalignment of the grating angle and the detector positions might be the additional factor which can give a contribution to the error.

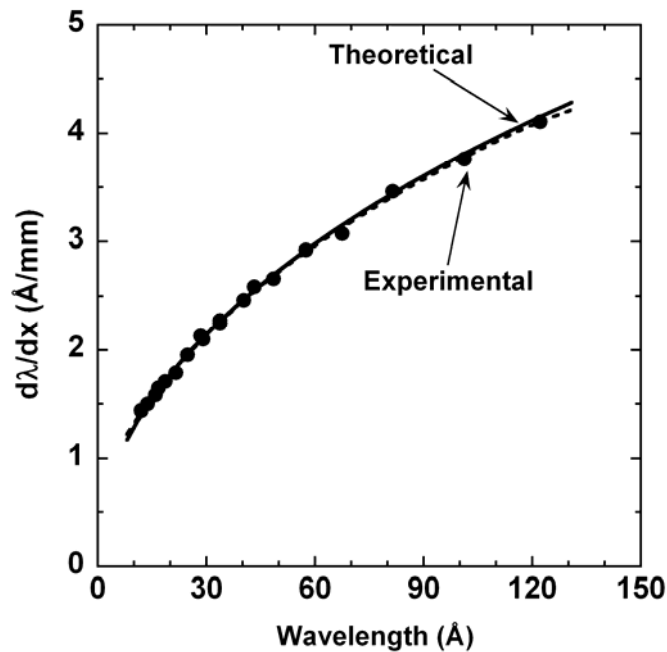


Fig. 2.14 Experimental and theoretical reciprocal linear dispersions as a function of wavelength. Experimental data plotted with solid circles are fitted with dashed line. Theoretical values are traced with solid curve.

2.2.3. Comparison between ruled and holographic gratings

After initial data collection using EUV emissions from the LHD plasma, the ruled grating was replaced by a laminar-type holographic grating. This grating, having essentially the same parameters as the ruled grating, has been very recently developed by Shimadzu Co. Ltd [27]. The grating has been aligned by the same technique as the ruled grating. After the precise grating alignment, the spectral resolution was checked, but, the resolution was not good when the CCD detector was set at the designed position. Results are shown in Fig.2.15. The value of $\Delta\lambda_0$ is the full width at foot position of each spectral line and ΔY is the shift from the designed position of $Y=235\text{mm}$. The value of $\Delta Y=0$ mm in the figure then means the designed position of the detector. It is clearly seen that the best position is recoded at $\Delta Y=0.15\text{--}0.25\text{mm}$ ($Y=236.5\text{--}237.5\text{mm}$). As a result, the detector was finally placed at 236.5 mm. The values of $\Delta\lambda_0$ at 18\AA are relatively large compared to 33 and 67\AA cases. This reflects the original defocus of the spectrometer system at shorter wavelength range (see Fig.2.13). However, this small displacement of the CCD position hardly affects the reciprocal linear dispersion at all. For example, the $d\lambda/dx$ is 2.27 and $2.21\text{\AA}/\text{mm}$ at 33.73\AA for the ruled and holographic gratings, respectively.

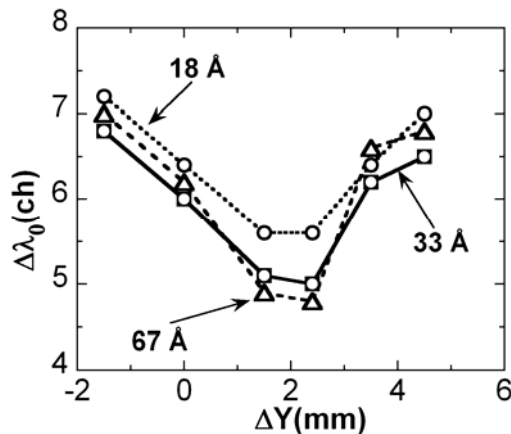


Fig. 2.15 Experimentally obtained spectral resolution $\Delta\lambda_0$ (full width at spectral foot position) at three wavelengths of 18\AA (open circles + dotted line), 33\AA (open squares + solid line) and 67\AA (open triangles + dashed line) for holographic grating as a function of distance from designed linear focal position. Value of $\Delta Y=0$ ($\equiv Y=235\text{mm}$) means detector surface is set just on the designed linear focal position (also see Fig.2.12).

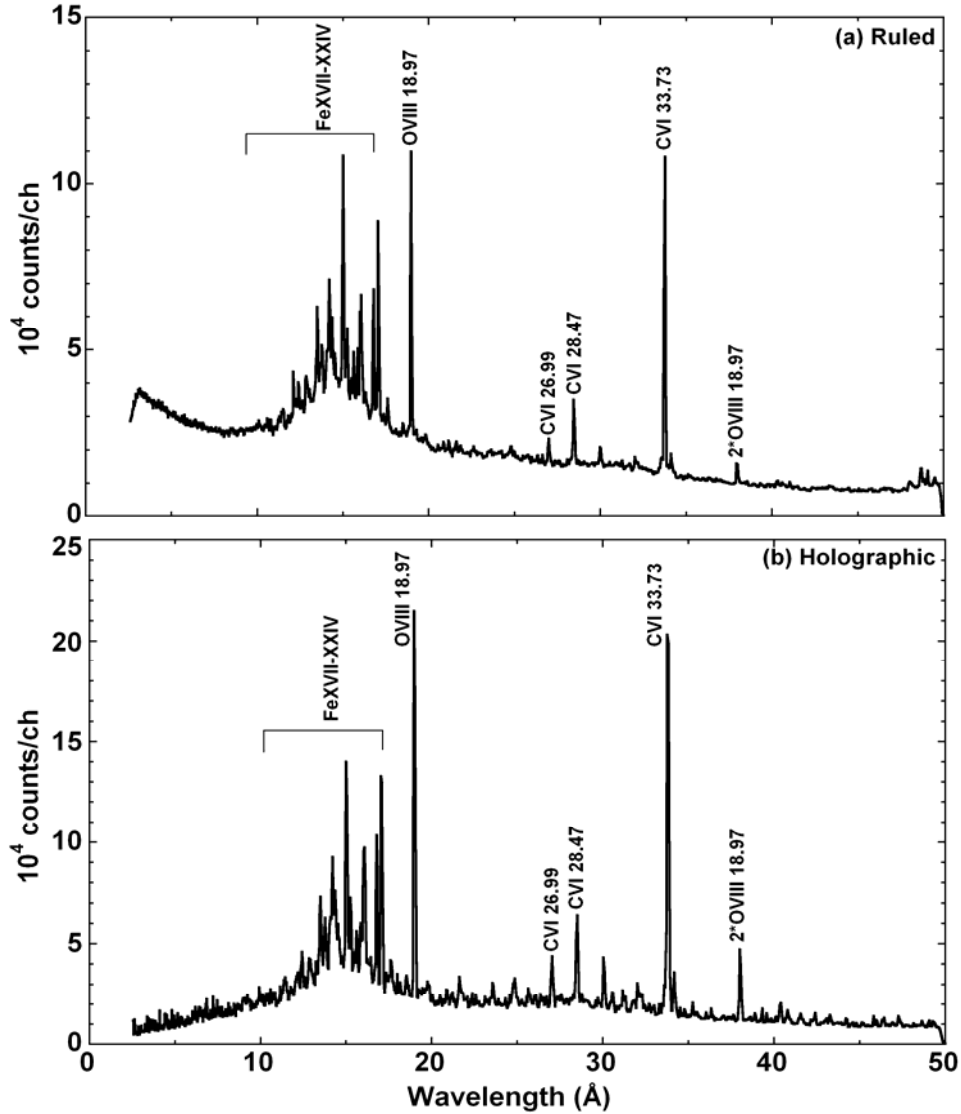


Fig. 2.16 Typical EUV spectra with (a) ruled and (b) holographic 2400grooves/mm gratings from NBI-heated LHD plasmas.

Figures 2.16 (a) and (b) show typical examples of the spectrum from the ruled and holographic gratings recorded at the shortest wavelength range of 3 to 50Å, respectively. Both spectra are obtained from solid hydrogen pellet fueled NBI discharges with line-averaged electron density of $9 \times 10^{19} \text{ m}^{-3}$. Here, it should be noted that both discharges are similar but not identical. Ten frames (5ms exposure/frame) are summed up for getting better signal-to-noise ratio. Spectral lines of H-like carbon (CVI) and oxygen (OVIII) are successfully observed along with a blended transition band of iron spectrum consisting of

L-shell $n=3-2$ transition arrays from FeXVII (Ne-like) to FeXXIV (Li-like). Details on the line analysis of the spectra are presented in the next section. It can be clearly seen from both spectra that the spectrometer is still working below 10\AA , because the background stray light including the zero-th order light is well suppressed. Unfortunately, no clear line emissions have been observed below 10\AA at present, since the spectrometer sensitivity becomes very dark at such short wavelength range. A large amount of high-Z impurity will be then required in order to see the spectrum in range of 3 to 10\AA . Nevertheless, this result strongly suggests that the present EUV spectrometer has an excellent capability for spectroscopic diagnostics in the core region of high-temperature plasmas. We also find from the two spectra that the behavior of the continuum is clearly different, especially below 13\AA . This suggests the different sensitivity between the two gratings.

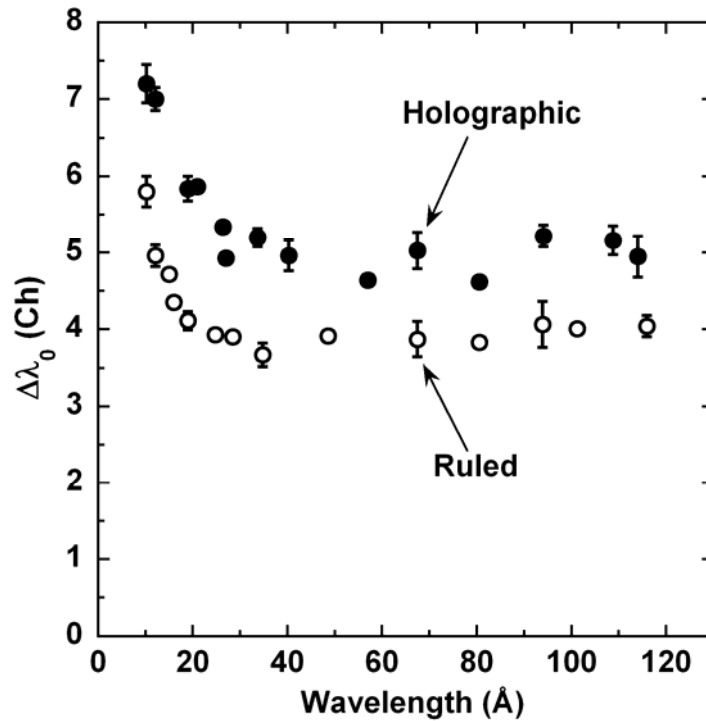


Fig. 2.17 Experimentally obtained spectral resolution $\Delta\lambda_0$ for ruled and holographic gratings as a function of wavelength.

The spectral resolution has been checked for both gratings using the emission spectrum from Ne in Ne-puffed discharges and from boron, carbon, titanium and molybdenum injected using an impurity pellet injector [18]. The comparison of the spectral width, $\Delta\lambda_0$ (full width at foot position of a spectral line), between the ruled and holographic gratings are plotted as a function of wavelength in Fig.2.17. The error bars in the plot are estimated by the variation of $\Delta\lambda_0$ derived from several discharges. The spectral width for the ruled grating is better than for the holographic grating in the whole wavelength range. The $\Delta\lambda_0$ mainly ranges in 3.6 to 4.0ch and 4.6 to 5.2ch for the ruled and holographic gratings, respectively, except for the data point at the short wavelength side. Examples of the Gaussian fitting for the ruled and holographic gratings are shown in Figs.2.18 (a) and (b), respectively. The CVI (33.73Å) is used for the fitting. The full width at half maximum (FWHM) of spectral line, $\Delta\lambda$, is 1.4ch (0.08Å) for the ruled grating and 2.2ch (0.13Å) for the holographic grating. Converting into the resolving power, $\lambda/\Delta\lambda$, it becomes 422 and 259 for the ruled and holographic gratings, respectively. Both values are quite better compared to a conventional grazing incidence spectrometer generally used for plasma diagnostics [28]. However, it should be pointed out that the spectral resolution for the newly developed laminar-type holographic grating is unfortunately not better compared to one for the ruled grating. It can be suggested that the holographic grating is still in development stage. Therefore, it is needed further improvement in design and fabrication technique to achieve the similar spectral resolution of the ruled grating. At least, however, we can argue that the spectral resolution is basically determined by the accuracy of each groove distance of the grating, whereas the surface figure and roughness determine the reflectivity. Taking into account the background of the grating fabrication, the distance between each groove is well defined for the ruled grating, although the surface figure of each groove is well defined and the surface roughness is smooth for the holographic grating. This can be easily considered that the production of the accurate groove distance is much easier for the ruled grating because the distance can be well controlled by external feedback during the groove fabrication. In contrast to this, the production of well defined groove distance in the holographic grating becomes very difficult for the grating with larger grooves density

such as 2400grooves/mm. This is the possible reason why the ruled grating has better spectral resolution.

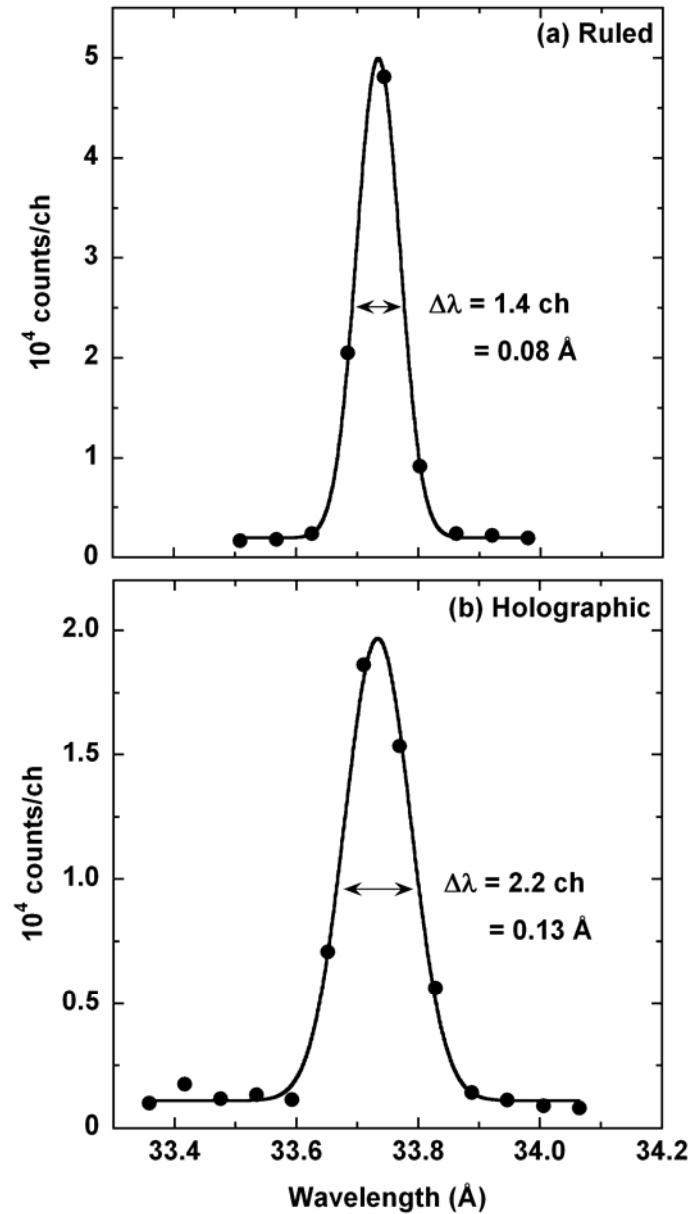


Fig. 2.18 Examples of Gaussian fitted line profile (solid curve) of CVI (33.73Å) show spectral resolution (FWHM: full width at half maximum) $\Delta\lambda$ for (a) ruled (b) holographic gratings (solid circles: experimental data). Determined spectral resolution at FWHM, $\Delta\lambda$, is expressed in units of channel and Å.

To examine the contribution from higher order light, the H-like resonance line of CVI (33.73Å) and its higher order light are illustrated in Figs.2.19 (a) and (b) for the ruled and holographic gratings, respectively. The EUV emission spectra recorded after the carbon pellet injection is used to increase the carbon spectral intensities at higher orders. Here, all the intensities are normalized by their 1st order light at 33.73Å. From the figure it can be seen that contributions from the second order light are only 4% and 11% to the 1st order light for the ruled and holographic gratings, respectively. The intensity of the third order light is very less and not well apparent in the figures. The contribution of higher order light for OVIII (18.97Å) (see Figs.2.16 (a) and (b)) is also similar to the CVI case. Namely, the contributions of the second order light are 7% and 18% to the 1st order light for the ruled and holographic gratings, respectively. This result concludes that the higher order light can be well suppressed in this short wavelength range by both gratings with slightly higher percentage of contribution from the holographic grating than the ruled grating. Holographic grating is generally hard to blaze properly.

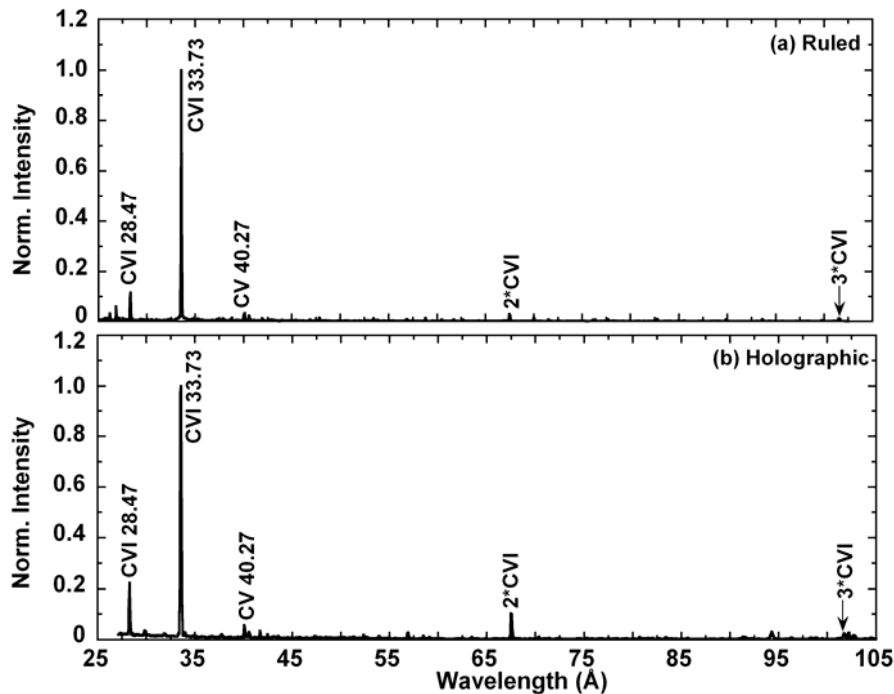


Fig. 2.19 EUV spectra from LHD discharges obtained for (a) ruled and (b) holographic gratings representing higher order CVI emissions. All the data are normalized to the first order light of CVI at 33.73Å

2.2.4. Absolute intensity calibration

Absolute intensity calibration of the EUV spectrometer is usually performed in this wavelength range using synchrotron radiation [29], which is a primary standard technique. However, there exist several technical difficulties in use of the synchrotron radiation such as the small emission volume and polarization of the light source. Therefore, the spectrometer calibration has been done in situ using the plasma emissions from LHD. The relative sensitivity of the spectrometer has been determined using EUV continuum [26] since the conventional branching ratio technique [30] can not be applied in such a lower wavelength region due to the absence of several suitable branching pairs. Here, it should be noticed that the technique using the EUV continuum requires two important things; (i) negligible higher order contribution and (ii) minimal overall noise including stray light. It has become clear in the last section that the higher order contribution is negligible. The thermal noise of the CCD is very low (~ 1 count/s/ch) since it is cooled by a Peltier device down to -20°C in the regular operation. The stray light has been almost reduced by introducing many masks and slits. This is checked by the density dependence of the EUV continuum. The EUV continuum is generally composed of bremsstrahlung and radiative recombination in magnetically confined fusion devices. However, the intensity of the radiative recombination can be ignored in steady discharges as compared to the bremsstrahlung intensity. The experimental continuum is compared with the theoretical bremsstrahlung continuum calculated from measured n_e and T_e profiles, which are routinely measured in LHD using Thomson scattering diagnostic system. The bremsstrahlung continuum is taken from a few similar stable discharges to scan the whole wavelength range of the spectrometer. Ten temporal frames, which mean a total integration time of 50ms, are summed up as the final data with good signal-to-noise ratio. The theoretically calculated values are integrated along line-of-sight of the spectrometer taking into account the electron density and temperature profiles. Figures 2.20 (a) and (b) are the results on the experimental and calculated bremsstrahlung continuum against the wavelength for ruled and holographic gratings, respectively. Both data are normalized at 93.92\AA . The closed circles indicate the experimental bremsstrahlung continuum. The data are fitted with a dash line. The calculated

bremsstrahlung continuum is shown with a solid line. The experimental continuum increases with decreasing wavelength for both gratings suggesting the T_e -dependence of the bremsstrahlung emission. But, the different slopes indicate different sensitivities of the gratings. Any analysis is not carried out below 20\AA because many unresolved lines are appeared in 10 to 20\AA range. The relative sensitivities of the both gratings have been thus derived from these results. It is presented in Fig.2.21. The two sensitivities are normalized at 93.92\AA . The relative sensitivity for the ruled grating has an almost constant value below 70\AA . In contrary, it gradually decreases with decreasing wavelengths for the holographic grating.

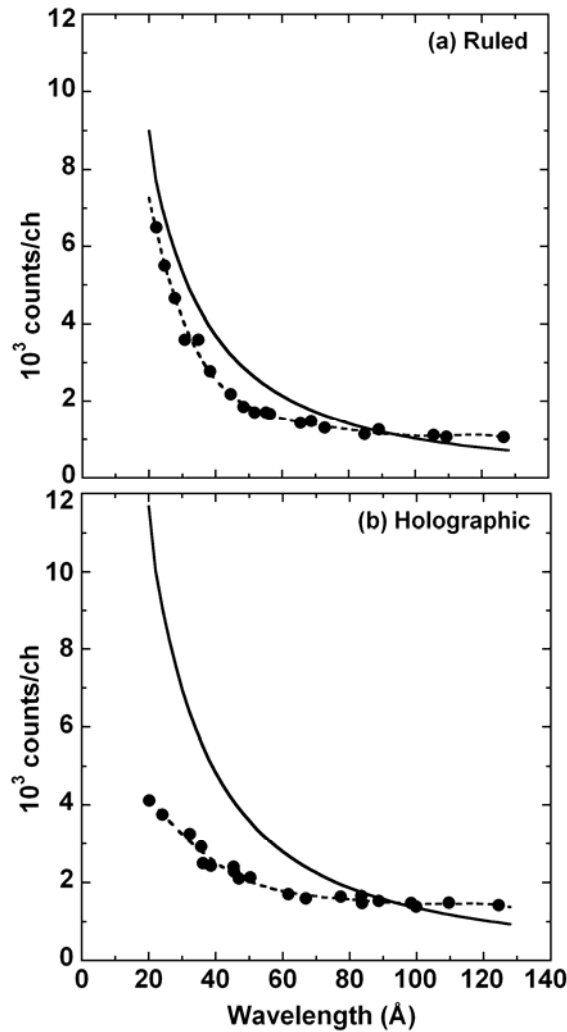


Fig. 2.20 Calculated (solid curve) and experimental (solid circles fitted with dashed curve) EUV bremsstrahlung continuum as a function of wavelength for (a) ruled and (b) holographic gratings.

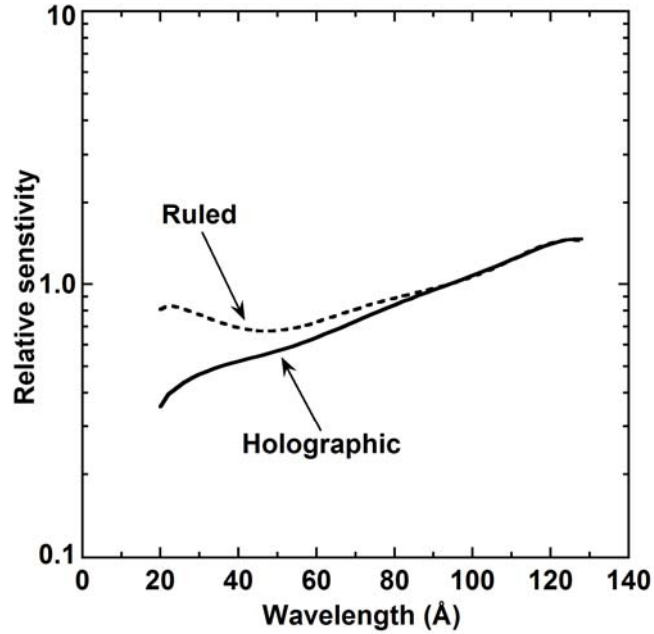


Fig. 2.21 Variation of relative sensitivities against wavelength for ruled (dashed curve) and holographic (solid curve) gratings. Both data are normalized at 93.92Å. It should be noted that absolute sensitivity is much different between ruled and holographic gratings.

The longer wavelength side (50 to 130Å) of the present spectrometer (EUV_Short) is overlapped with an absolutely calibrated EUV spectrometer (called as EUV_Long) [26] with 1200grooves/mm grating used for monitoring 50 to 500Å range. This enables us to carry out the absolute intensity calibration of this newly developed spectrometer. For this purpose, isolated strong line emissions from FeXVIII and FeXIX are selected in 90 to 120Å range. The result is plotted in Fig.2.22, which shows the absolute sensitivity (inverse of the absolute intensity calibration factor) for the both gratings. The error bars in the plot are estimated by the variation of the sensitivity derived from several different discharges. The holographic grating is three times more sensitive than the ruled grating in the whole wavelength range, except for the shorter wavelength below 30Å. It suggests that the holographic grating has a well defined surface structure and roughness compared to the ruled grating.

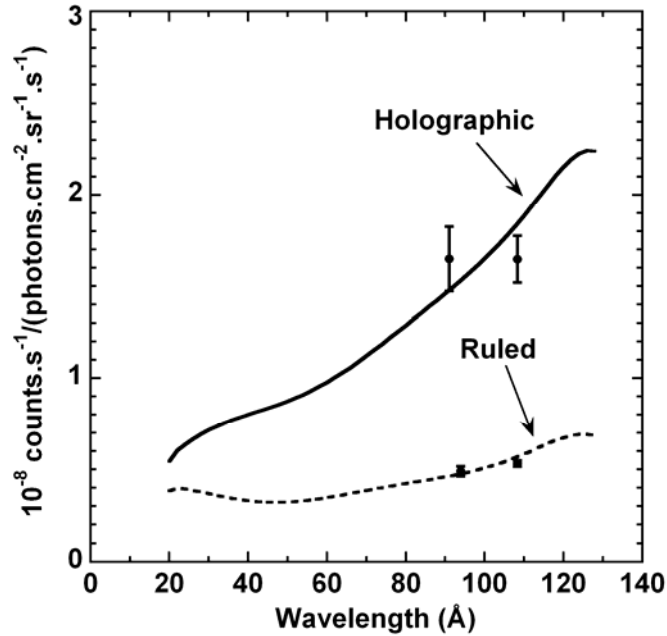


Fig. 2.22 Absolute sensitivity of 2400grooves/mm EUV spectrometer with ruled (dashed curve) and holographic (solid curve) gratings as a function of wavelength. Data points (solid circles) with error bars are obtained from absolutely calibrated 1200grooves/mm EUV spectrometer. Please note that spectrometer sensitivity is the inverse of calibration factor.

Relative calibration is done by comparing the calculated and measured bremsstrahlung continuum. Therefore the experimental error has several sources, such as, electron density (n_e) and temperature (T_e) values, effective charge (Z_{eff}) of the plasma, free-free Gaunt factor (g_{ff}) and its variation with wavelength. The measured T_e and n_e values were taken from Thomson diagnostics and Z_{eff} was measured using visible continuum radiation. The contribution in error from these sources does not vary with wavelength. Only the variation of g_{ff} with the wavelength and scattered light give the error as a function of wavelength. In the calculation of the continuum, we have neglected the variation of g_{ff} with the wavelength. The g_{ff} value slowly increases with the wavelength and weakly depends on T_e . In LHD the continuum emission comes through the radial location with different n_e and T_e . As the calculation was carried out under the consideration of measured n_e and T_e profiles, the overall contribution from g_{ff} becomes 25%. Except for the smaller values of n_e and T_e in the plasma edge, the error in the

measurement in the n_e and T_e are 7 and 10%, respectively. As shown in Fig.2.22 the statistical error in the measurement of intensities of the emission line has also been included. Considering all these sources, maximum error becomes around 54% in the calibration.

2.2.5. Summary

A flat-field spectrometer with a VLS ruled concave 2400grooves/mm grating (EUV_Short) has been developed to measure the EUV spectra in 10 to 130Å wavelength range. The angle of incidence of 88.65° gives an excellent spectral resolution of 0.08Å at 33.73Å indicating a good spectroscopic performance for studying the spectral structure of medium- and high-Z impurities in fusion plasmas. To make clear the superior capabilities of the holographic grating in viewpoints of suppression of the stray light and higher order light, a comparative study has been done between the ruled and holographic gratings. It is found that the both gratings can efficiently suppress the stray light and higher order light, although percentage of suppression differs between both gratings.

Relative sensitivity determined from EUV continuum indicates gradual drop with decreasing wavelength in 20 to 130Å for the holographic grating, but almost constant value in 20 to 70Å for the ruled grating. The absolute calibration is done by comparing with another absolutely calibrated EUV spectrometer with 1200grooves/mm for 50 to 500Å measurement (EUV_Long) in the overlapping range of 50 to 130Å. As a result, it is found that the absolute sensitivity of the holographic grating is three times brighter than that of the ruled grating, although the spectral resolution of the holographic grating is not so good compared to the ruled grating.

2.3. Spectroscopic evaluation on a ruled and two holographic gratings to monitor 10-30Å

2.3.1. Introduction

Spectra of $n=3-2$ transitions from partially L-shell-ionized medium-Z impurities ($16 \leq Z \leq 27$) appeared in fusion plasmas are emitted in 10–30Å range. This wavelength range also includes several spectral lines of high-Z impurities such as Mo and W of which the use is planned in ITER. These spectra have not been actively observed until now mainly due to the technical difficulty. Recently, flat-field extreme ultraviolet (EUV) spectrometers [25, 27, 31], which have an easy coupling of CCD detector on its flat focal plane, have been employed to observe emission spectra in such a short wavelength range because it can easily measure wider wavelength interval with good spectral resolution compared to conventional grazing incidence spectrometer and crystal spectrometer [32].

In Large Helical Device (LHD) [33], on the other hand, two EUV spectrometers have been recently developed for 10–500Å measurement where emission spectra from various intrinsic and extrinsic impurities exist [26, 34]. As a result, the spectrometer with varied-line-spacing 1200grooves/mm for 50–500Å measurement could be operated very well replacing the ruled grating by the holographic grating. On the other hand, when the ruled grating with varied-line-spacing 2400grooves/mm (Hitachi 001-0471) for 10–130Å measurement was replaced by the holographic grating (Shimadzu 30-001), it was visible that further good spectral resolution was required in the 10–30Å range where many spectral lines closely exist, whereas the stray light was very less. A new holographic grating has been desired for the improvement of the spectral resolution in the 10-30Å range. The new holographic grating (Shimadzu 30-003) has been recently developed with modified grating parameters. The groove depth and the duty ratio (\equiv groove top width to groove spacing) for the new holographic grating are replaced by 7.0 ± 2 nm and 0.40 ± 0.2 , respectively. The parameters for the old one were 8.5 ± 2 nm and 0.35 ± 0.2 , respectively.

Details on the flat-field EUV spectrometer for 10–130Å range have been discussed in section 2.2.2. Here, a comparative study on the spectral characteristics of

spectrometer with three different gratings are presented for the detection of $\Delta n=1$ transitions in 10–30Å range. The spectral characteristics of the newly designed holographic grating are also presented with the comparison to computationally simulated spectral resolution.

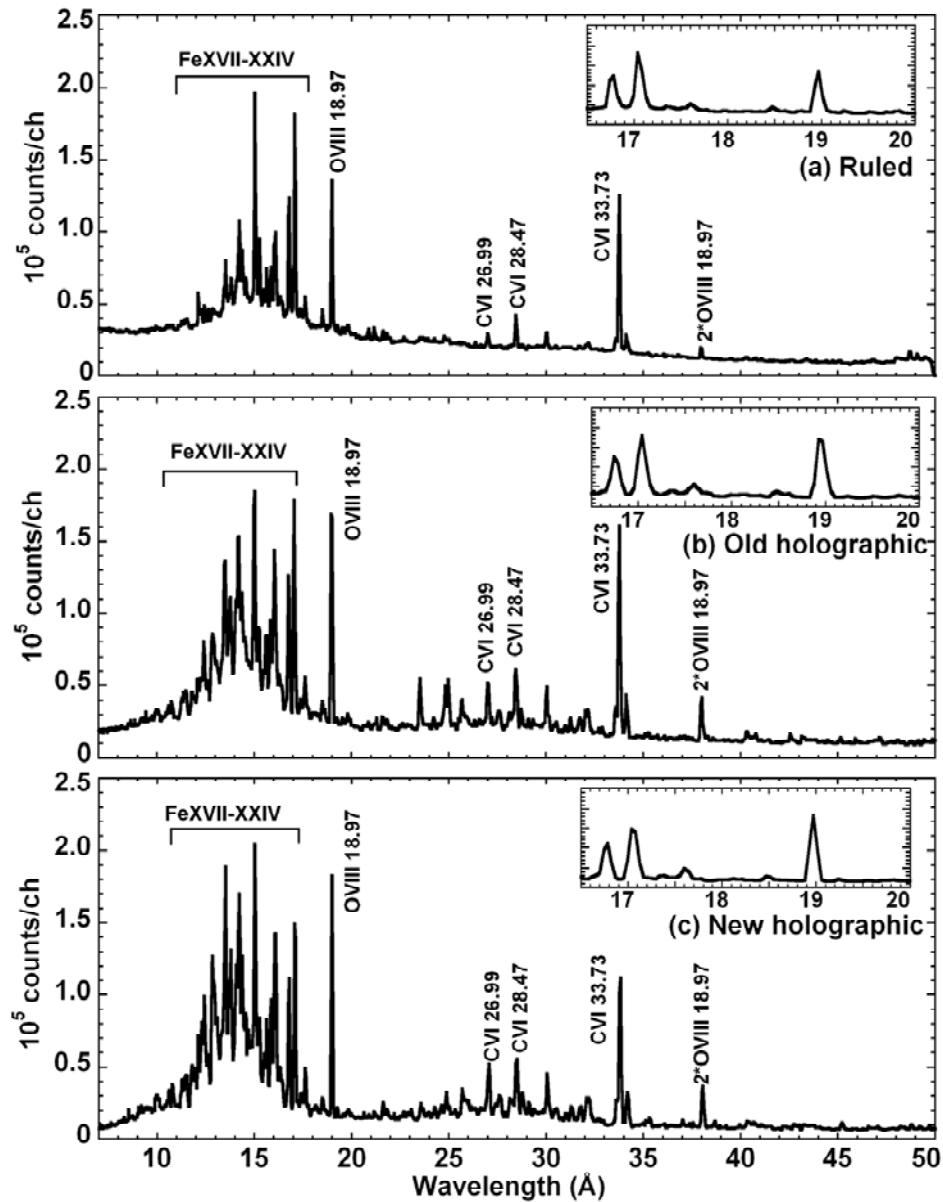


Fig. 2.23 Typical spectra from LHD discharges obtained with (a) ruled, (b) old holographic and (c) new holographic gratings. Spectra expanded in 16.5–20.0Å range are also shown in the inset for comparison of spectral resolution.

2.3.2. Comparative studies on a ruled and two holographic gratings

Emission spectra from LHD plasmas have been routinely observed to monitor the overall impurity behavior and to study the relation to the plasma performance. EUV spectra from partially L-shell ionized medium-Z impurity have been also observed during the experiment. Figure 2.23 shows a typical example of the EUV spectra with $\Delta n=1$ transitions from iron in the wavelength range of 7–50Å. Each spectrum is obtained using three different gratings with varied-line-spacing 2400grooves/mm, i.e., (a) ruled, (b) old holographic and (c) new holographic gratings. The data were recorded by replacing the grating. Spectra were taken from H₂ pellets fueled LHD plasmas with line-averaged electron density of $7\text{--}9\times 10^{19}\text{ m}^{-3}$. The density is higher in the case of ruled grating. The central electron temperature ranges in 700–850eV. The exposure time of CCD is 5ms and the data are summed up over 10 frames to improve the signal-to-noise ratio. K_{α} lines of H-like carbon and oxygen are also observed along with $n=3\text{--}2$ transitions of FeXVII (Ne-like) to FeXXIV (Li-like). The higher order light is well suppressed for all the gratings. Spectral line at 18.97Å of OVIII shows the contribution of second order light is only 7% and 18% for ruled and both holographic gratings, respectively. The spectra are expanded in 16.5–20.0Å range at the inset. The difference in the spectral resolution is apparent for the three gratings.

Absolute sensitivity has been compared among three gratings, as shown in Fig.2.24. The method of the absolute calibration based on the bremsstrahlung continuum can be found in [26, 34]. The sensitivity calibration is not done at wavelengths lower than 20Å due to the presence of many spectral lines as revealed in Fig.2.23. It is found that absolute intensity calibration factors, i.e., inverse of absolute sensitivity, of both holographic gratings are nearly the same and the holographic gratings are roughly three times brighter than the ruled grating. This result suggests that the holographic gratings have well-defined surface condition and roughness.

Figure 2.25 shows the spectral width, $\Delta\lambda_0$ (full width at foot position of a spectral line), of all three gratings as a function of wavelength. Here, the $\Delta\lambda_0$ is given by the relation of $N=I_0\times\Delta ch/2$, where N is the total counts of the line, I_0 the peak intensity and Δch the full width at foot position. The widths are estimated using spectral emissions

from B, C, O, Ne, Ti and Fe. The $\Delta\lambda_0$ of the ruled grating is better than both holographic gratings in 20–130Å range. But the $\Delta\lambda_0$ of the newly developed holographic grating noticeably improves towards shorter wavelength, i.e. at lower than 40Å, compare to the old holographic grating. The spectral resolution of the new holographic grating becomes then equal to one of the ruled grating at wavelength range lower than 20Å. In terms of full width at half maximum (FWHM) of a spectral line, $\Delta\lambda$, the values become 0.083Å and 0.090Å at 18.97Å for the ruled and new holographic gratings, whereas it is fairly large for the old holographic grating, i.e., 0.130Å.

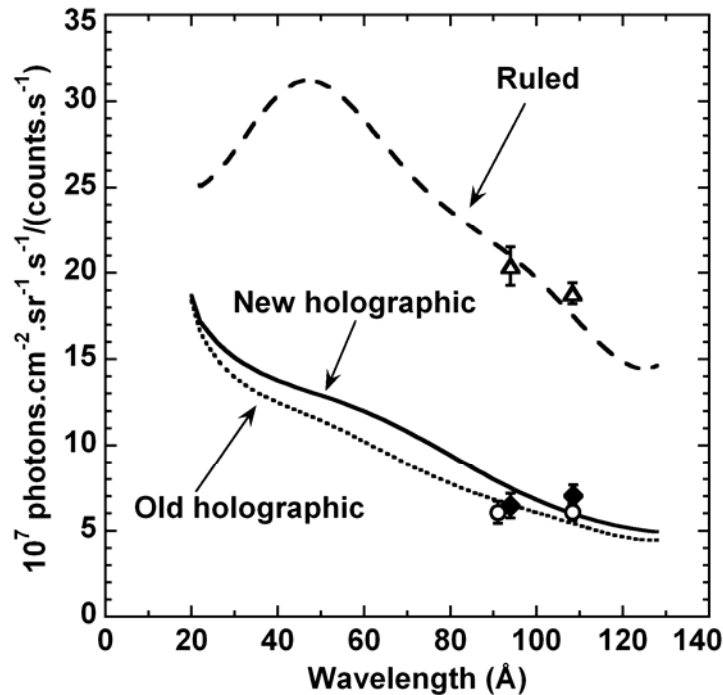


Fig. 2.24 Inverse absolute sensitivities as a function of wavelength for ruled (dashed line), old holographic (dotted line) and new holographic (solid line) gratings determined from the measured bremsstrahlung continuum intensity. Two spectral lines of FeXVIII and XIX (open triangles: ruled, open circles: old and solid diamonds: new) are used for absolute calibration compared with absolutely calibrated another EUV spectrometer.

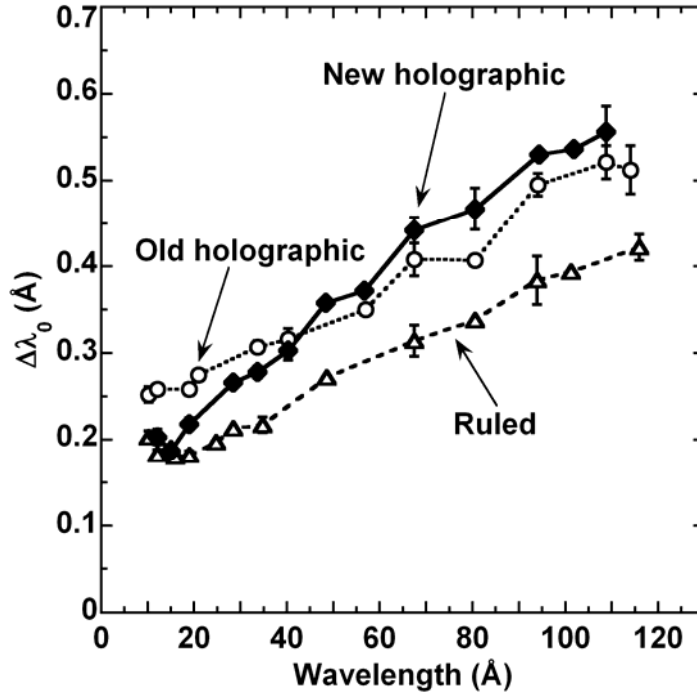


Fig. 2.25 Experimentally obtained spectral resolution ($\Delta\lambda_0$, full width at foot position of spectrum) for ruled (open triangles), old holographic (open circles) and new holographic (solid diamonds) gratings as a function of wavelength.

This improved spectral resolution for the new holographic grating is visible in computationally simulated spectral resolution, as depicted in Fig.2.26. Here, the spectral resolution of $\Delta\lambda$ is plotted with wavelength for the old and new holographic gratings. The simulated value of the new holographic grating shows better spectral resolution in 10–70Å range except around 20Å. This better spectral resolution has been achieved with the modification of the designed laminar-type grating parameters, such as line-spacing variation, groove depth and duty ratio. As shown in Fig.2.27, the local line-spacing varies from –15.7% to +21.1% against the central line-spacing of 2400grooves/mm for the old holographic grating. In the case of the new holographic grating the line-spacing variation is modified by 0–0.4% compared to the old one. This modification in local line-spacing is also plotted in the figure. As mentioned in section 2.3.1, these changes in parameters are really effective to improve the spectral resolution of the holographic grating. But the present new design has been only partially reflected in the wavelength

region shorter than 40\AA (see Fig.2.25). It is believed that the manufacturing constraint on the accuracy in the varied-line-spacing groove distance, which mainly defines the spectral resolution, becomes severe in the case of the holographic grating compared to the ruled grating. As a result, the spectral resolution could not well achieve the designed value. However, any practical problems do not appear in the present fusion plasma spectroscopy at the long wavelength side of $40\text{--}130\text{\AA}$, because spectral lines do not exist closely. Overall, it can be rightly argued that the present newly developed holographic grating is more suitable to monitor $\Delta n=1$ transition in $10\text{--}30\text{\AA}$ compare to the ruled and old holographic gratings.

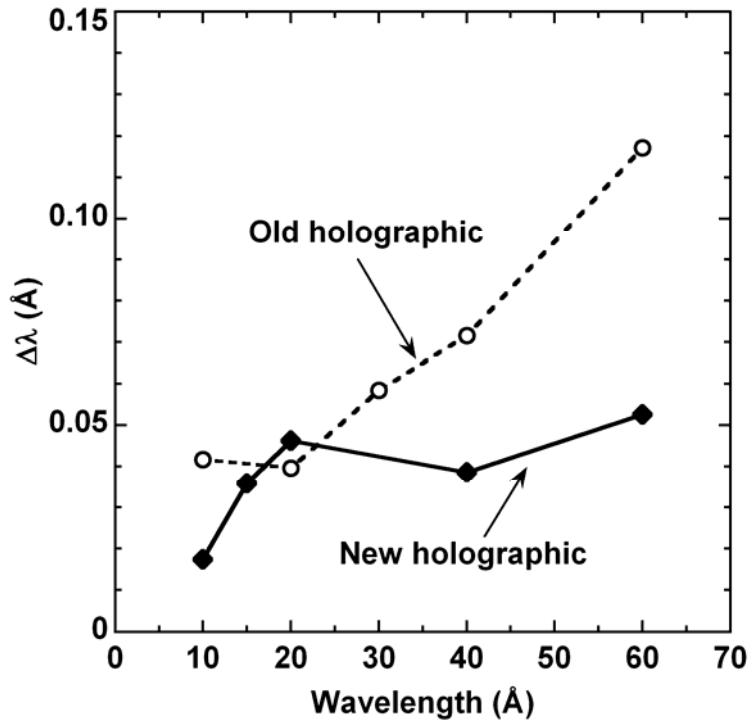


Fig. 2.26. Computationally simulated spectral resolution ($\Delta\lambda$, full width at half maximum of spectrum) for old holographic (open circles) and new holographic (solid diamonds) gratings as a function of wavelength.

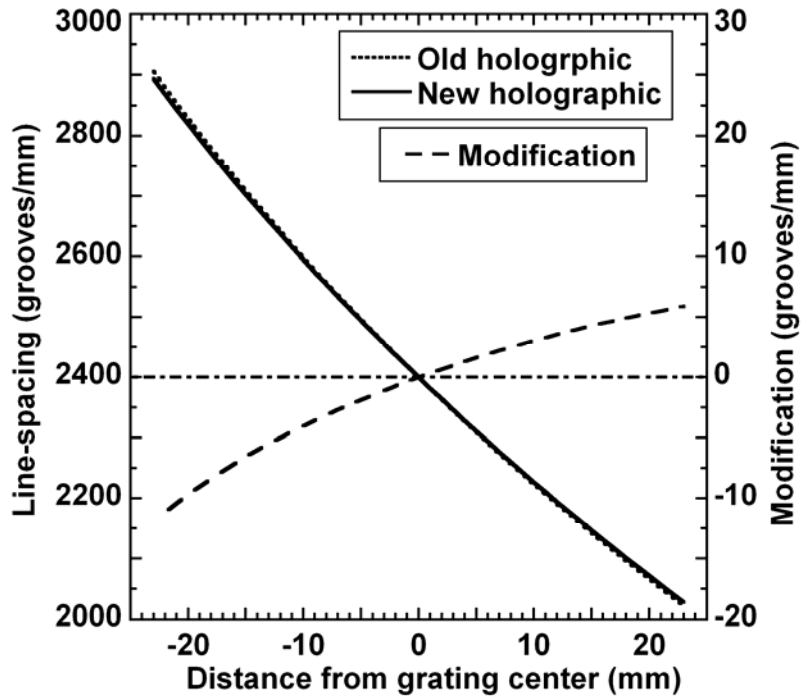


Fig. 2.27 Local groove line-spacing as a function of distance from grating center for old (dotted line) and new (solid line) holographic gratings. Modification from old holographic grating is traced with dashed line.

2.3.3. SUMMARY

Comparative studies of a flat-field EUV spectrometer with a ruled and two holographic gratings demonstrated that the newly developed holographic grating will be better choice to diagnose fusion plasmas in 10–30Å ranges. It possesses brighter sensitivity than the ruled grating having nearly similar spectral resolution. As a result, closely existed but relatively weaker spectral lines of n=3-2 transitions from partially L-shell-ionized medium-Z impurities can be successfully monitored.

2.4. Comparison between 1200 and 2400grooves/mm gratings

The spectral resolution of the spectrometer generally increases with an increase in the groove density of the grating, but at the expense of spectral range and brightness. This contradictory aspect can be resolved by choosing the grating suitable to the experimental purpose. In this section typical characteristics of the two EUV spectrometers with 1200 and 2400grooves/mm gratings are presented with the comparative study. We have defined the spectrometer with 2400grooves/mm grating as EUV_Short, which covers 10 to 130Å wavelength range and the spectrometer with 1200 grooves/mm grating as EUV_Long, which covers 50 to 500Å wavelength range. These two spectrometers overlap the wavelengths in 50 to 130Å. Examples of EUV spectra in 50 to 130Å are shown in Figs.2.28 (a) and (b) for EUV_Short and EUV_Long, respectively. The twenty frames corresponding to integration time of 100 ms is summed up in the figures. Both spectra are recorded from the same NBI discharge simultaneously. Line emissions mainly consist of several $\Delta n=0$ transition of Fe XVIII and Fe XIX. Those lines are identified as 93.92 (2s2p⁶ ²S_{1/2}-2s²2p⁵ ²P_{3/2}) and 103.94Å (2s2p⁶ ²S_{1/2}-2s²2p⁵ ²P_{1/2}) from F-like FeXVIII and 91.01 (2s2p⁵ ¹P₁-2s²2p⁴ ¹D₂) and 108.35Å (2s2p⁵ ³P₂-2s²2p⁴ ³P₂) from O-like FeXIX.

Figures 2.29 (a) and (b) show the comparison of spectral resolution, $\Delta\lambda$, in FWHM and absolute sensitivity for the two spectrometers, respectively. The data from EUV_Short (EUV_Long) are plotted with solid (open) circles and solid (dashed) line in Figs.2.29 (a) and (b), respectively. The absolute sensitivity in Fig.2.29 (b) are reproduced from Fig.2.11 for EUV_Short with holographic grating and from section 2.1.4 for EUV_Long. It is evident from the figures that the sensitivity of the EUV_Long spectrometer is nearly ten times higher than that of the EUV_Short spectrometer. But, the spectral resolution is obviously poor in case of the EUV_Long because of its lower grooves density. For example, spectral resolutions of EUV_Short and EUV_Long spectrometers are 0.21 and 0.35Å at 108.35Å, respectively. Therefore, it can be simply concluded that the EUV_Short spectrometer with 2400grooves/mm grating is well suitable for the study of spectral structure in high-Z impurities and the EUV_Long spectrometer with 1200grooves/mm grating is better for monitor as impurity diagnostics

at least in the 50 to 130Å range. Although the EUV_Long spectrometer can be used below 50Å in principle, the spectral resolution becomes much worse [26]. It is then out of use for plasma spectroscopy. As a result, the 10 to 50Å range can only be diagnosed by the present newly developed EUV_Short spectrometer with 2400grooves/mm grating.

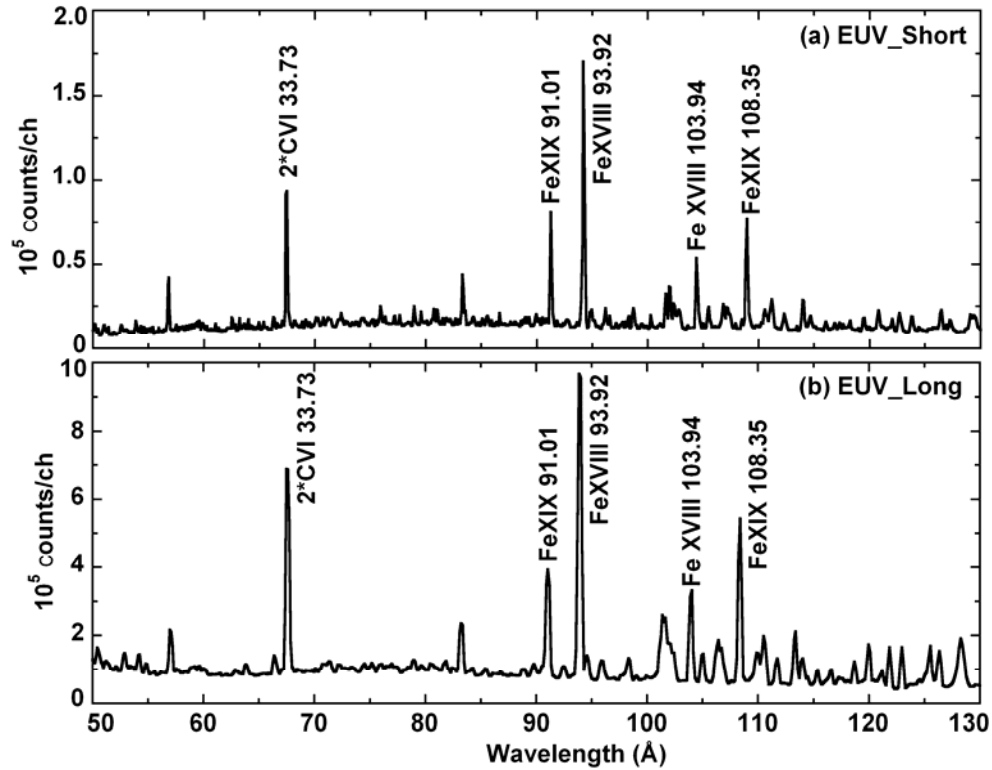


Fig. 2.28 Comparison between EUV Spectra in 50 to 130Å simultaneously recorded from two flat-field spectrometers of (a) EUV_Short (2400grooves/mm for 10 to 130Å measurement) and (b) EUV_Long (1200grooves/mm for 50 to 500Å measurement).

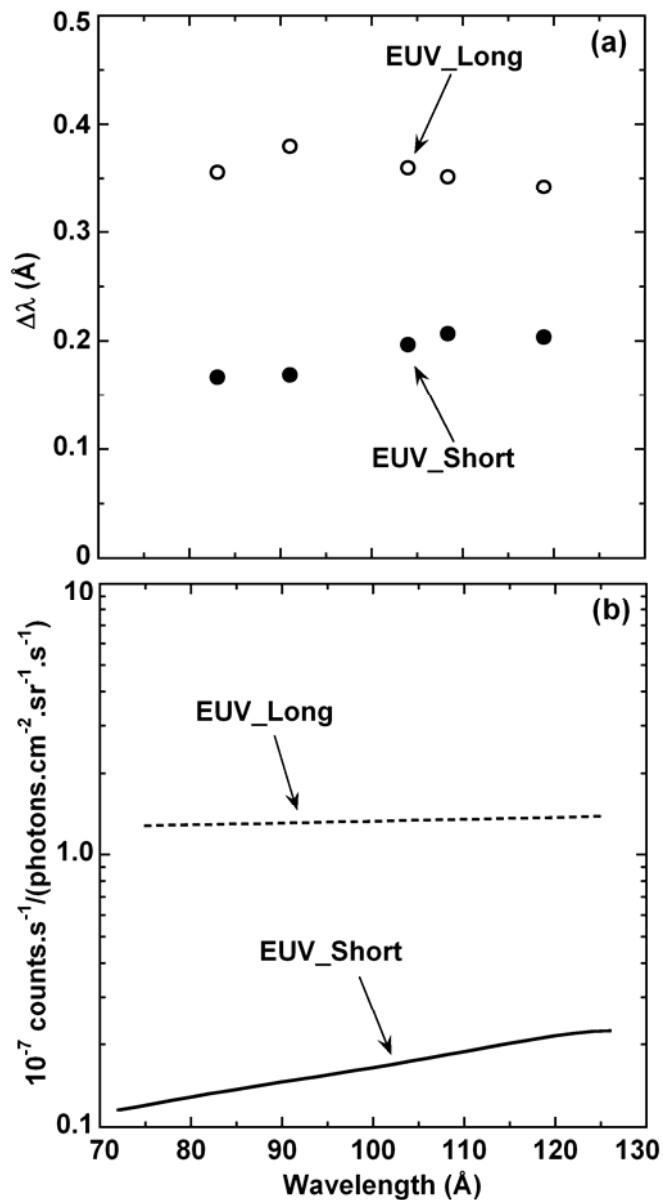


Fig. 2.29 Comparison of (a) spectral resolution (FWHM) and (b) absolute sensitivity between two EUV spectrometers; EUV_Short (2400grooves/mm for 10 to 130Å measurement) and EUV_Long (1200 grooves/mm for 50 to 500Å measurement). Solid (open) circles in (a) and solid (dashed) curve in (b) represent data from EUV_Short (EUV_Long).

REFERENCES

- [1] R. J. Fonck et al., *Appl. Opt.* **21**, 2115 (1982).
- [2] T. Kawachi et al., *Rev. Sci. Instrum.* **66**, 1042 (1995).
- [3] K. Kondo et al., *Jpn. J. Appl. Phys.* **27**, 1287 (1988).
- [4] M. Yoshikawa et al., *Nucl. Instrum. Methods A* **467-468**, 1533 (2001).
- [5] T. Kita et al., *Appl. Opt.* **22**, 512 (1983).
- [6] M. Koike et al., *Proceeding of SPIE* **4146**, 163 (2000).
- [7] M. Koike et al., *J. electron Spect. & Rel. Phenom.* **101-103**, 913 (1999).
- [8] J. H. Underhood et al., *Proceeding of SPIE* **3150**, 40 (1997).
- [9] K. Sato et al., *Appl. Opt.* **23**, 3336 (1984).
- [10] T. Harada and T. Kita, *Appl. Opt.* **19**, 23 3987 (1980).
- [11] U. Feldman et al, *Astron. Astrophys.* **441**, 1211 (2005).
- [12] K. Narihara et al., *Rev. Sci. Instrum.* **72**, 1122 (2001).
- [13] K. Kadota et al., *Nuclear Fusion* **20**, 2, 209 (1980).
- [14] S. Morita et al., *Physica Scripta*, **T91**, 48 (2001).
- [15] S. Muto, S. Morita et al., *Rev. Sci. Instrum.* **72**, 1206 (2001).
- [16] Yu. Ralchenko et al., *NIST Atomic Spectra Database (version 3.1.1)*, Online, (2007), http://physics.nist.gov/PhysRefData/ASD/lines_form.html.
- [17] C De Michelis, and M Mattioli, *Rep. Prog. Phys.* **47**, 1233 (1984).
- [18] H. Nozato, S. Morita, M. Goto et al., *Rev. Sci. Instrum.* **74**, 2032 (2003).
- [19] R. Katai, S. Morita, M. Goto et al., *Jpn. J. Appl. Phys.* **46**, 3667 (2007).
- [20] S. Morita, M. Goto et al., *Plasma Sci. Tech.* **6**, 2440 (2004).
- [21] S. Morita et al., *Nucl. Fusion* **43**, 899 (2003).
- [22] R. Katai, S. Morita, and M. Goto, *J. Quant. Spect. Rad. Trans.* **107**, 120 (2007).
- [23] R. Katai, S. Morita, and M. Goto, *Plasma Fusion Res.* **2**, 006 (2007).
- [24] M. B. Chowdhuri, S. Morita, M. Goto et al., *Plasma Fusion Res.* **2**, S1060 (2007).
- [25] N. Nakano, et al., *Appl. Opt.*, **23**, 2386 (1984).
- [26] M. B. Chowdhuri, S. Morita, M. Goto et al., *Rev. Sci. Instrum.* **78**, 023501 (2007).
- [27] M. Koike et al., *Rev. Sci. Instrum.* **74**, 1156 (2003).
- [28] W. L. Hodge et al., *Rev. Sci. Instrum.* **55**, 16 (1984).

- [29] M. May et al., Rev. Sci. Instrum **74**, 2011 (2003).
- [30] M. Daltrini, and M. Machida, IEEE Trans. Plasma Sc. **33**, 1961 (2005).
- [31] P. Beiersdorfer et al., Rev. Sci. Instrum. **77**, 10F306 (2006).
- [32] I. Sakurai, Y. Tawara, C. Matsumoto, A. Furuzawa, S. Morita and M. Goto, Rev. Sci. Instrum. **77**, 10F328 (2006).
- [33] S. Morita, T. Morisaki, M. Goto et al., Nucl. Fusion **47**, 1033 (2007).
- [34] M. B. Chowdhuri, S. Morita and M. Goto., Appl. Opt. **47**, 135 (2008).

Chapter 3

EUV spectra and line analysis

3.1. Details on Mo and W spectra observed by EUV_Long

3.1.1. Introduction

Next generation fusion device will produce further heat load onto the first wall and divertor plates, and it may give rise to a serious damage to such plasma facing components. It is widely known that the high-Z materials instead of carbon become favorable to the plasma facing material, because such materials have less sputtering yield in addition to their high melting point [1]. At present, the use of tungsten [2] and molybdenum [3] is planned in ITER as a candidate for the plasma facing components. Then, the spectroscopic study on the high-Z impurities becomes important in the next generation fusion device. The spectral lines of the high-Z elements, however, have not been well investigated until now, e.g., even their wavelengths. Most of the spectral lines from the high-Z elements are at least emitted in extreme ultraviolet (EUV) and soft X-ray ranges when the electron temperature is greater than 1–2keV. An extensive study is necessary on the line analysis of the high-Z elements in addition to a theoretical work on atomic physics.

For this purpose molybdenum and tungsten have been injected in Large Helical Device (LHD) plasmas using an impurity pellet injector [4]. The emission spectra have been monitored with a flat-field EUV spectrometer [5] to identify their wavelengths and to analyze their time behaviors as a function of electron temperature. In this paper results on possible identification of the spectral lines emitted from highly ionized tungsten and molybdenum are presented with EUV spectra in wavelength range of 20–500Å. The wavelengths of spectral lines identified here are also compared with previous experimental and calculated values.

3.1.2. Experimental Setup

Data are recorded from LHD discharges with magnetic field strength of 2.64T and average plasma major and minor radii of 3.75m and 60cm, respectively. Three tangential negative-ion-based neutral beam injection (NBI) devices were used to initiate and heat the plasma up to an electron temperature (T_e) of 2.5keV. Line-average electron densities were in the range of $1-4 \times 10^{19} \text{m}^{-3}$. Cylindrical carbon impurity pellets involving thin tungsten and molybdenum wires [6] have been injected perpendicularly to the toroidal plasma axis at the equatorial plane. The pellet size used in the present experiment was 0.8mm in diameter and 0.8mm in length and the wire size was 0.2mm in diameter and 0.5mm in length. The EUV emission spectra from the injected materials were measured by a flat-field EUV spectrometer with a 1200grooves/mm laminar-type holographic grating. The distance between the grating center and the entrance slit is 237mm and the distance between the focal plane perpendicular to the grating surface and the grating center is 235mm. A back-illuminated vacuum ultraviolet (VUV) sensitive charge coupled device (CCD) detector was mounted at the focal position. The size of the CCD is $26.6 \times 6.6 \text{mm}^2$ with a pixel size of $26 \times 26 \mu\text{m}^2$ and the number of channels of 1024×255 . The CCD detector was cooled down to -20°C to suppress the thermal noise and operated in 'full-binning mode' to take the signal output with a time interval of 5 ms. The spectral resolution of the spectrometer is 0.16\AA at 70\AA . The first and higher order emissions from CVI and other intrinsic impurity lines were used as a marker for the wavelength calibration. The whole spectra ($20-500 \text{\AA}$) were recorded from several discharges by moving the CCD detector since the spectrometer can measure only a wavelength interval of 160\AA at a time. The charge states of measured lines are mainly determined by temporal variations of the line intensities after the pellet injection and during temperature decay phase at the end of discharges.

3.1.3. EUV Spectra and Analysis

3.1.3.1. Molybdenum

Figure 3.1 revealed the EUV spectrum from highly ionized molybdenum in the wavelength range of 20–165Å. The last 25Å between 140 and 165Å was composed of another similar discharge. The highest ionization state of Na-like Mo (MoXXXII; I.E.–1719.32eV) has been observed in this experiment where the central electron temperature was 2.5keV at the pellet injection. The central electron temperature rapidly drops to nearly 1.8keV after the impurity pellet injection and recovered to 2.2keV with decrease in the electron density. The Mo emissions begin to appear at 25ms after the pellet injection and are continuously observable during the following 500ms. A complicated structure is seen at 65–90Å. This unresolved spectral array mostly consists of charge stages of MoXXIV–MoXXVIII, but the precise identification is now impossible. These charge states belong to K-like through P-like molybdenum ions and the lines therefore mainly have transitions among $n=3$ with $\Delta n=0$. The result of the detailed wavelength identification for Mo lines is presented in Table 3.1 with their transitions. The numerical values followed \pm sign indicate the accuracy in wavelength measurement. It was estimated from the maximum deviation of weighted peak position of a spectral line in different temporal frames. The theoretically calculated and predicted values are also indicated in the table. The brackets following the values show their references. The calculated values are based on ab initio energy level calculation. The predicted values are based on the extrapolation of experimentally measured energy levels at low-Z elements followed by the ab initio energy level calculation. Only the MoXXVIII $3p^2(^3P)3d^4P_{3/2}-3p^3^4S_{3/2}$ transition at 81.947Å had not been observed yet, but it has been newly observed in this study, which is presented as 81.87Å in the Table 3.1. As mentioned in table several strong 3d-3p transitions from MoXXIV to MoXXVIII are the major contributor of the unresolved spectral array around 65–90Å.

On the other hand, several other isolated lines are also seen at shorter and longer wavelength sides of the unresolved spectral array in Fig.3.1 including several forbidden transitions from MoXV and MoXVI [12]. For example two electric quadruple transitions

(E2) of $3d^9 4s\ 1,3D_2-3d^{10}\ 1S_0$ in the Ni-like MoXV can be clearly seen at 57.92 and 58.83Å. The strongest isolated lines are emitted at 115.98 ($3p\ 1P_1-3s^2\ 1S_0$) and 127.9Å ($3p\ 2P_{3/2}-3s\ 2S_{1/2}$) as a resonance transition of Mg-like MoXXXI and Na-like MoXXXII. These charge states exist in the central region of the LHD plasma under the present experimental condition. The intensities of these resonance lines reached to the maximum value after 75ms of the pellet ablation and frequently saturated in the 16 bit CCD counts. The identification of relatively weak spectral lines below 50Å was not done in the present study because the spectral resolution of the spectrometer rapidly drops at such shorter wavelength range [5]. These spectra likely consist of 4f-3d transitions of MoXV to MoXVI and 4p-3d transitions of MoXVI to MoXIX [3]. Since these charge states exist in a very narrow radial location near the plasma edge where the electron temperature is relatively low, the molybdenum emissions become weak compare to the other lines from higher charge states.

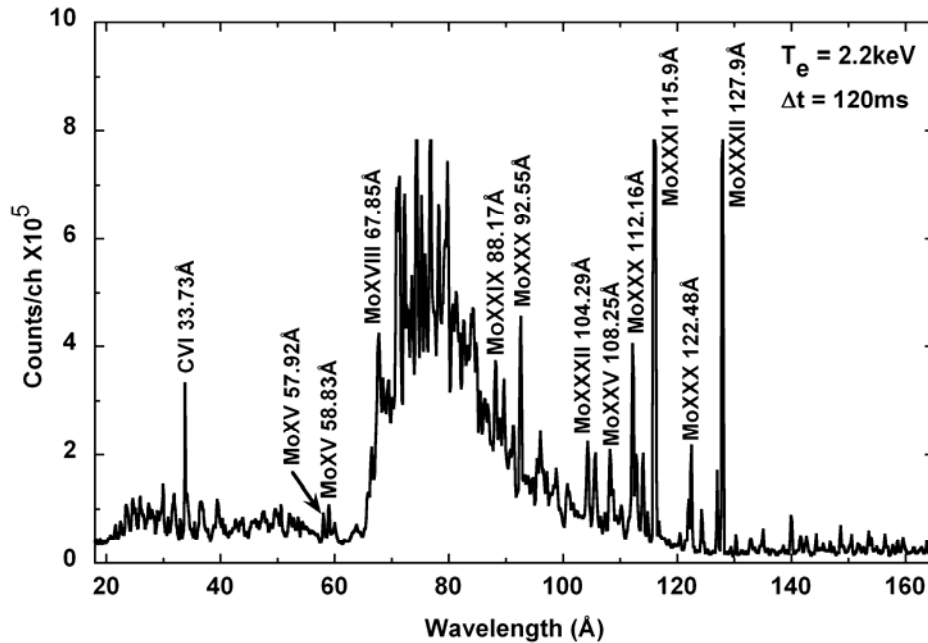


Fig. 3.1 Mo spectrum in 20–165Å.

Table 3.1 Observed transitions of Mo ions in 65–90Å.

Ionization stages	Transitions	Wavelengths (Å)			
		Present experiment	Previous experiment	Calculated	Predicted
MoXXIV	$3p^6 3d^2 D_{3/2} - 3p^5 3d^2 ({}^3F) {}^2D_{3/2}$	70.83±0.02	70.8 [9]	68.9 [10]	
	$3p^6 3d^2 D_{5/2} - 3p^5 3d^2 ({}^3P) {}^2P_{3/2}$	71.34±0.03	71.24 [9]	70.1 [10]	
	$3p^6 3d^2 D_{5/2} - 3p^5 3d^2 ({}^3F) {}^2D_{5/2}$	72.22±0.02	72.12 [9]	70.2 [10]	
	$3p^6 3d^2 D_{3/2} - 3p^5 3d^2 ({}^1S) {}^2P_{1/2}$	73.50±0.05	73.300 [8]		
	$3p^6 3d^2 D_{5/2} - 3p^5 3d^2 ({}^3F) {}^2F_{7/2}$	75.17±0.02	75.0 [10]	74.1 [10]	
	$3p^6 3d^2 D_{3/2} - 3p^5 3d^2 ({}^3F) {}^2F_{5/2}$	77.38±0.05	77.354 [8]		
MoXXV	$3p^6 {}^1S_0 - 3p^5 3d {}^1P_1$	74.40±0.02	74.2 [9]	73.1 [10]	
MoXXVI	$3p^5 {}^2P_{3/2} - 3p^4 ({}^1D) 3d {}^2P_{1/2}$	72.61±0.04	72.7 [10]	69.5 [10]	
	$3p^5 {}^2P_{3/2} - 3p^4 ({}^3P) 3d {}^2P_{3/2}$	75.82±0.06	75.2 [10]	72.8 [10]	
	$3p^5 {}^2P_{3/2} - 3p^4 ({}^3P) 3d {}^2D_{5/2}$	76.85±0.05	76.73 [9]	73.4 [10]	
	$3p^5 {}^2P_{3/2} - 3p^4 ({}^1D) 3d {}^2S_{1/2}$	78.16±0.05	78.4 [10]	75.7 [10]	
	$3p^5 {}^2P_{3/2} - 3p^4 ({}^1S) 3d {}^2D_{3/2}$	79.34±0.06	79.3 [10]	76.5 [10]	
	$3p^5 {}^2P_{1/2} - 3p^4 ({}^3P) 3d {}^2P_{1/2}$	84.29±0.02	84.069 [8]		
MoXXVII	$3p^4 {}^3P_2 - 3p^3 ({}^2P) 3d {}^3P_2$	79.74±0.02	79.761 [8]		
	$3p^4 {}^1D_2 - 3p^3 ({}^2D) 3d {}^1F_3$	80.67±0.06	80.403 [8]		
	$3p^4 {}^3P_2 - 3p^3 ({}^2D) 3d {}^3D_3$	81.20±0.04	81.302 [8]		
MoXXVIII	$3p^3 {}^4S_{3/2} - 3p^2 ({}^3P) 3d {}^4P_{3/2}$	81.87±0.04	Not observed		81.947 [11]
	$3p^3 {}^2D_{3/2} - 3p^2 ({}^1D) 3d {}^2D_{5/2}$	82.54±0.06	82.773 [8]		82.821 [11]
	$3p^3 {}^2D_{5/2} - 3p^2 ({}^3P) 3d {}^2F_{7/2}$	83.21±0.05	83.308 [7]		
	$3p^3 {}^4S_{3/2} - 3p^2 ({}^3P) 3d {}^4P_{5/2}$	83.89±0.03	83.756 [7]		
	$3p^3 {}^2P_{1/2} - 3p^2 ({}^1D) 3d {}^2P_{3/2}$	84.67±0.05	84.771 [8]		

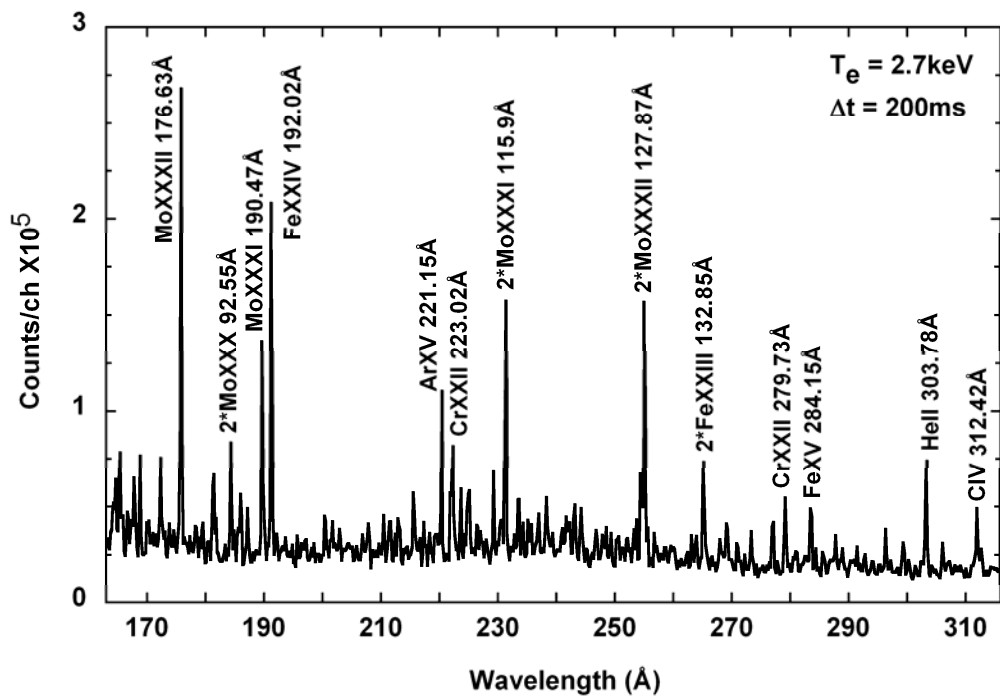


Fig. 3.2 Mo spectrum in 165–315Å.

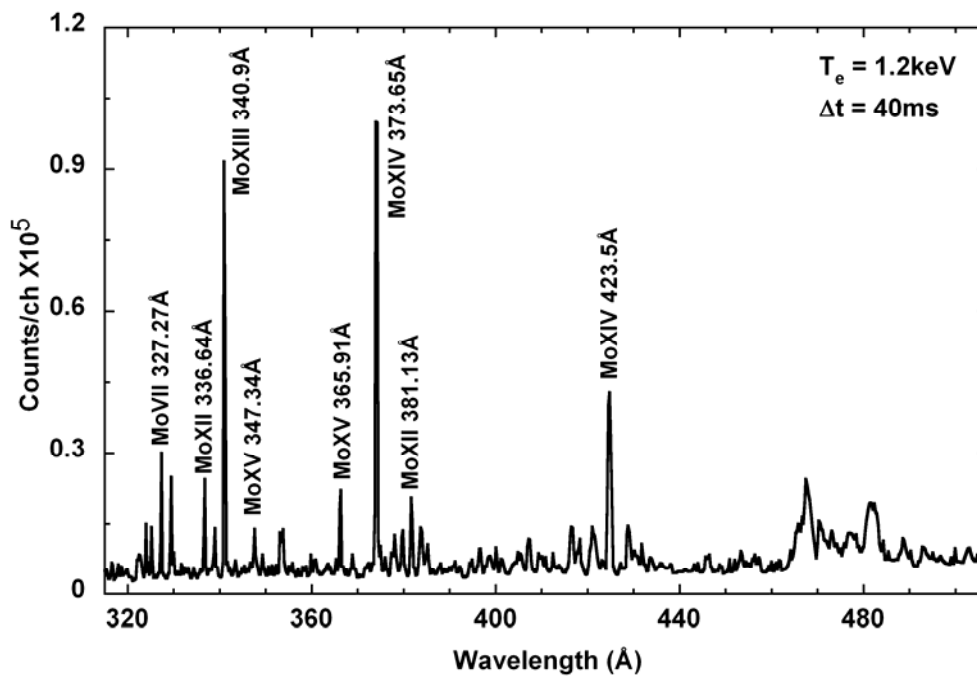


Fig. 3.3 Mo spectrum in 315–500Å.

A molybdenum EUV spectrum in wavelength range of 165–315Å is shown in Fig.3.2, which contains several other impurity lines. Such impurity lines are useful for the wavelength calibration. In the figure, then, the spectrum containing several impurity lines was specially selected for good understanding, although the discharge condition was slightly different from the previous one. The 3p-3s doublet (127.9, 176.63Å, $3p\ ^2P_{3/2, 1/2}-3s\ ^2S_{1/2}$) in resonance transition of Na-like MoXXXII are apparent with strong intensities in Figs.3.1 and 3.2. A similar type of transition is also seen in Fig.3.2 from Li-like FeXXIV at 192.02Å ($2p\ ^2P_{3/2}-2s\ ^2S_{1/2}$). Other resonance transitions are clearly appeared at 221.15Å for Be-like ArXV ($2s2p\ ^1P_1-2s^2\ ^1S_0$), 223.02 and 279.73Å for Li-like CrXXII ($2p\ ^2P_{3/2, 1/2}-2s\ ^2S_{1/2}$) and 284.15Å for Mg-like FeXV ($3s3p\ ^1P_1-3s^2\ ^1S_0$).

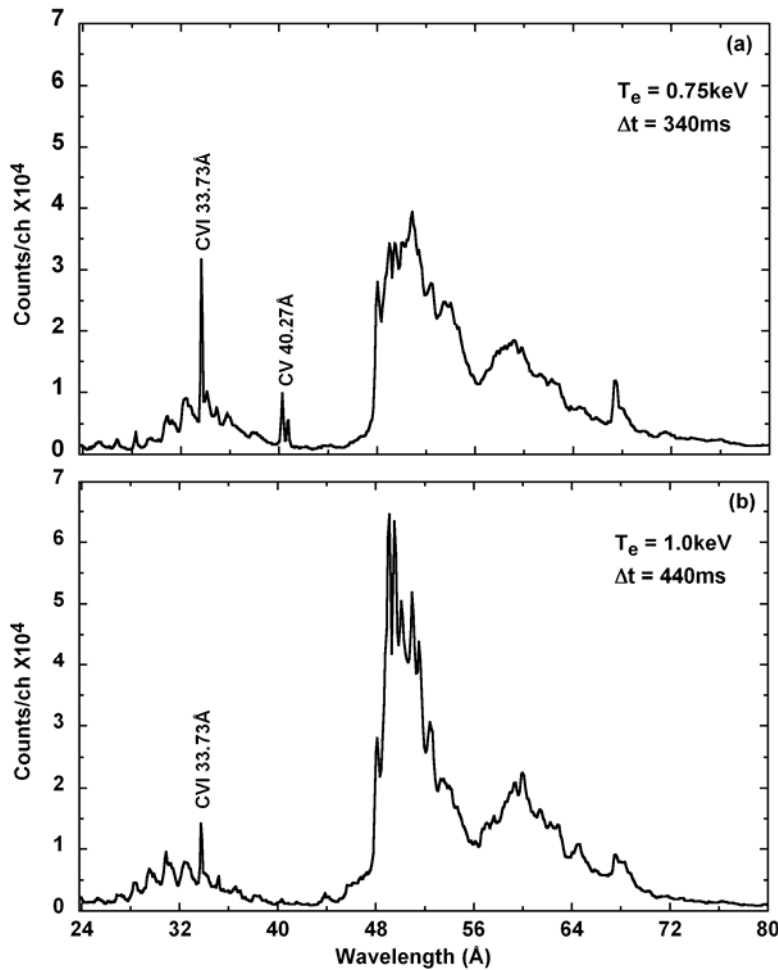


Fig. 3.4 W spectra in 24–80Å at (a) $\Delta t=340\text{ms}$ and (b) $\Delta t=440\text{ms}$ after pellet injection.

Strong resonance lines from lower charge states molybdenum ions of Zn-like MoXIII (340.91\AA , $4s4p\ ^1P_1-4s^2\ ^1S_0$) and Cu-like MoXIV (373.65 , 423.5\AA $4p\ ^2P_{3/2, 1/2}-4s\ ^2S_{1/2}$) are recorded as revealed in Fig.3.3. These relatively low ionized states of molybdenum immediately appear after the impurity pellet ablation.

3.1.3.2. Tungsten

Tungsten lines from different ionization stages in EUV and soft X-ray ranges have been identified with reference to theoretically calculated and experimentally observed values [2, 13–19]. After the carbon pellet containing the tungsten material was injected, the central electron temperature rapidly decreased from 2.20 to 0.75keV due to the ionization and radiation losses and then recovered up to 1.20keV. Figure 3.4 shows tungsten spectra in wavelength range of 24–80Å. The spectrum in Fig.3.4 (a) is recorded at $\Delta t=340\text{ms}$ after the injection where the central electron temperature had the lowest value of 0.75keV. On the contrary the spectrum in Fig.3.4 (b) is recorded at $\Delta t=440\text{ms}$ with higher electron temperature of 1.00keV. Three blended transition bands are visible around 33, 50 and 60Å.

The band around 33Å consists of charge states in WXXII–WXXX with ionization potentials of 594.5–1179.9eV, respectively. As evidently seen in Fig.4 the peak position of this band shifts from 34 to 31Å as the electron temperature increases from 0.75 to 1.00keV, whereas the peak positions of the blended band at 50 and 60Å do not move against such a temperature difference. The spectral lines near 34Å from low-temperature plasma after 340ms of the pellet injection peaked at 34Å are emitted from charge states of WXXII to WXXVI and those near 31Å from high-temperature plasma after 440ms are dominated by higher ionization stages, e.g., WXXIX; $4d^95p\ ^1P_1-4d^{10}\ ^1S_0$, 29.4Å. Most of these lines have been identified and listed in Table 3.2. Theoretically calculated values were determined by ab initio calculation on mean wavelength averaged over large number of transitions using Unresolved Transition Array (UTA) formula. Only the transition of $4d^95p\ ^1P_1-4d^{10}\ ^1S_0$ at 29.4Å was predicted as isoelectronic extrapolation of Pd-like transition observed for lower Z elements. The transitions of WXXII to WXXVI

belong to $\Delta n=1$ radiative decay with the configurations of $4d^9 4f^k 5p-4d^{10} 4f^k$ and $4f^{k-1} 5g-4f^k$, where $k=3-7$. Three observed lines identified as 32.50, 35.86 and 38.13Å are blended with two transitions as indicated in the Table 3.2, because of inadequate spectral resolving power of the present spectrometer at such an extremely short wavelength range. The theoretically calculated line at 33.59Å (WXXV; $4d^9 4f^4 5p-4d^{10} 4f^4$) can not be identified since another strong CVI (33.73Å) line exists in the same wavelength position.

Table 3.2 Observed transitions of W ions in 24–40Å.

Ionization stages	Transitions	Wavelengths (Å)			
		Present experiment	Previous experiment	Calculated	Predicted
WXXII	$4d^9 4f^7 5p-4d^{10} 4f^7$	38.13±0.07	Not measured	37.57 [18]	
	$4f^6 5g-4f^7$			37.95 [18]	
WXXIII	$4f^6-4f^5 5g$	35.86±0.07		35.93 [18]	
	$4d^9 4f^6 5p-4d^{10} 4f^6$			36.21 [18]	
WXXIV	$4d^9 4f^5 5p-4d^{10} 4f^5$	34.90±0.06		34.85 [18]	
	$4f^4 5g-4f^5$	34.12±0.06		34.06 [18]	
WXXV	$4f^3 5g-4f^4$	32.50±0.05		32.43 [18]	
WXXVI	$4d^9 4f^3 5p-4d^{10} 4f^3$	32.50±0.05		32.37 [18]	
	$4f^2 5g-4f^3$	30.90±0.03		30.94 [18]	
WXXIX	$4d^9 5p \ ^1P_1-4d^{10} \ ^1S_0$	29.51±0.03			29.40 [19]
	Not identified	28.32±0.05			
		26.87±0.04			
		25.36±0.05			

In the blended bands around 50 and 60Å several lines are strongly appeared on the top of the pseudo-continuum when the electron temperature recovers up to 1.00keV as indicated in Fig.3.4 (b). The isolated lines observed here are estimated to be from WXXVIII, WXXIX and WXXX, taking into account the ionization potentials and previous works. The transitions identified here are listed in Table 3.3. K. Asmussen et al. [2] and J. Sugar et al. [15–17] tabulated many observed, calculated and predicted wavelengths in these band structures and their transitions are also listed in the Table 3.3 as previous works. The transition at 48.02Å measured in the present study was originally observed in ORMAK tokamak [13] and considered to be from Au [16], but did not appear in PLT tokamak [14]. It is finally identified here as the tungsten line, since any gold material is not used inside the LHD vacuum chamber. This line is then in good agreement with the predicted wavelength (47.94Å) of WXXVIII $4d^9 4f^2 \ ^2F_{7/2}-4d^{10} 4f^2 \ ^2F_{5/2}$

[16]. The emissions around 60Å are likely to be from triplet transitions of WXXIX $4d^9 4f-4d^{10}$ and WXXVIII $4d^9 4f^2-4d^{10} 4f$ [17].

Table 3.3 Observed transitions of W ions in 50–70Å.

Ionization stages	Transitions	Wavelengths (Å)			
		Present experiment	Previous experiment	Calculated	Predicted
WXXVIII	$4d^9 4f(^1P)4f^2 G_{7/2}-4d^{10} 4f^2 F_{7/2}$	52.31±0.03	52.35 [13]		52.35 [16]
	$4d^9 4f(^1P)4f^2 G_{7/2}-4d^{10} 4f^2 F_{5/2}$	51.42±0.02	51.457 [16]	51.245 [16]	51.455 [16]
	$4d^9 4f(^1P)4f^2 G_{9/2}-4d^{10} 4f^2 F_{5/2}$	50.87±0.02	50.895 [16]	50.7 [16]	50.891 [16]
	$4d^9 4f(^1P)4f^2 D_{3/2}-4d^{10} 4f^2 F_{5/2}$	49.44±0.02	49.4 [2],	48.919 [16]	49.405 [16]
	$4d^9 4f(^1P)4f^2 D_{5/2}-4d^{10} 4f^2 F_{7/2}$		49.403 [16]	48.874 [16]	49.402 [16]
	$4d^9 4f^2 F_{7/2}-4d^{10} 4f^2 F_{5/2}$	48.02±0.02	47.94 [13]		47.94 [16]
WXXIX	$4d^9 4f^3 D_1-4d^{10} ^1S_0$	59.88±0.02	59.852 [15]	59.736 [15]	59.851 [15]
	$4d^9 4f^1 P_0-4d^{10} ^1S_0$	49.00±0.02	48.9 [2], 48.948 [15]	49.295 [15]	48.944 [15]
WXXX	$4d^8(^1G)4f^2 P_{3/2}-4d^9 2D_{5/2}$	49.99±0.03	49.938 [17]	50.034 [17]	49.936 [17]
	Not identified	67.96±0.05			
		65.87±0.05			
		64.53±0.04			
		62.13±0.05			
		61.19±0.05			
		59.17±0.04			
		57.54±0.03			
		56.73±0.04			
		53.32±0.04			

3.1.4. Summary

EUV spectra of molybdenum and tungsten have been investigated and several transitions have been newly identified. Carbon pellets containing such materials were injected in LHD for the observation. Molybdenum spectra are observed in 20–500Å and the pseudo-continuum lines are identified and listed with previous works in wavelength range of 65–90Å. Some forbidden transitions from MoXV and MoXVI are also identified around 55Å. Although several weak lines are observed below 50Å, those can not be analyzed due to a poor spectral resolution of the present spectrometer.

Three blended spectral bands are observed for the tungsten spectrum in 24–80Å. The spectral band at 33Å shifted to shorter wavelength range when the electron temperature increased from 0.75 to 1.00keV. These spectra are identified as $\Delta n=1$ transition of

WXXII–WXXVI having $4d^9 4f^k 5p-4d^{10} 4f^k$ and $4f^{k-1} 5g-4f^k$, where $k=3-7$. Isolated lines were seen on the top of the pseudo-continuum in 50–70Å when the electron temperature increased up to 1.00keV. Those are identified as $\Delta n=0$ transitions of WXXVIII–WXXX. These tungsten lines observed here are also listed in the table with previous works. In the future a detail analysis on EUV spectra will be studied below 50Å using an EUV spectrometer with better resolution.

3.2. Details on low and medium-Z spectra observed by EUV_Short

EUV spectra from low-Z impurities, such as boron, carbon and nitrogen, and medium-Z impurities like Ti and Fe were observed from the LHD plasmas. Data was acquired using EUV_Short spectrometer for 10-130Å range [20]. The data are taken with an exposure time of 5ms in the full vertical binning mode of the CCD detector with good signal-to-noise ratio. The wavelength is precisely calibrated using strong BIV, BV, CV, CVI, NVII, OVIII, NeIX and NeX spectral lines emitted from the LHD plasmas.

In figure 3.5 we present highly ionized low-Z impurities spectrum around 20 to 65Å from the LHD plasma. The spectrum is recorded just after a BN compound is injected into the LHD plasma using an impurity pellet injector [4]. The spectrum is dominated by strong K-shell emissions from H- and He-like ions of such low-Z impurities. The unresolved doublet of H-like NVII are apparent at 20.91 ($3p^2 P_{1/2, 3/2}-1s^2 S_{1/2}$) and 24.78Å ($2p^2 P_{1/2, 3/2}-1s^2 S_{1/2}$). He-like NVI consists of resonance (28.79Å; $1s2p^1 P_1-1s^2^1 S_0$) and inter-combination (29.08Å, $1s2p^3 P_2-1s^2^1 S_0$) lines. The strong resonance lines from H-like BV (48.59Å, $3p^2 P-1s^2 S$) and He-like BIV (60.31Å, $1s2p^1 P_1-1s^2^1 S_0$) are also recorded in addition to the intrinsic carbon emissions (CVI: 33.73Å and CV: 40.27Å).

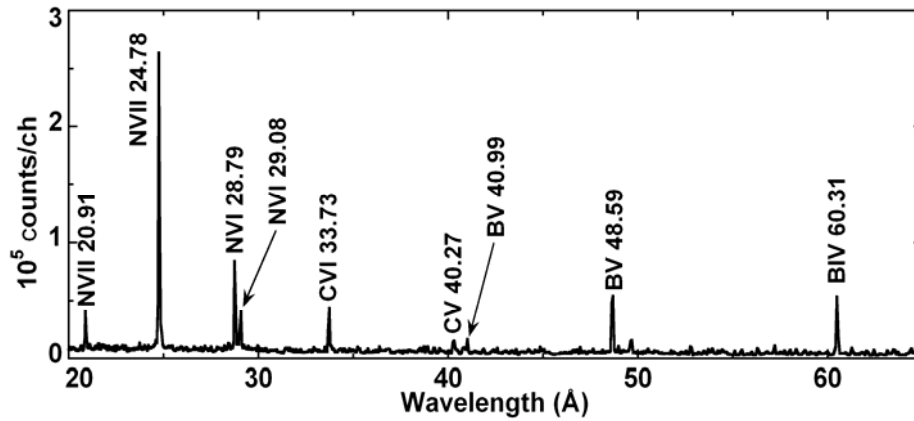


Fig. 3.5 EUV spectrum in 20 to 65Å of H- and He-like ions from low-Z impurities in LHD with boron-nitride impurity pellet injection.

Spectrum from the intrinsic iron impurity is revealed in Fig.3.6. The L-shell iron spectrum with $n=3-2$ transition around 10 to 20Å has been extensively studied for considerably long time from solar active region [21, 22], EBIT [23, 24] and tokamak [25, 26], where the spectra are recorded mainly using a crystal spectrometer. However, the wavelength range which can be simultaneously observed is very limited in the crystal spectrometer case because of the Bragg reflection geometry. On the contrary, the flat-field EUV spectrometer can cover the full spectrum of the L-shell iron emissions. Recently, a flat-field EUV spectrometer has been implemented to acquire the L-shell iron spectrum from the EBIT [27]. S. B. Utter et al. reported L-shell spectrum of Ne-like FeXVII in a range of 11.3 to 18.2Å using the flat-field spectrometer with a resolving power ($\lambda/\Delta\lambda$) of 70 at 15.26Å [27]. The present spectrometer yields better spectral resolution ($\lambda/\Delta\lambda \sim 200$ at 18.97Å of OVIII) and can adequately resolve the spectrum around 10 to 20Å.

A typical result on the full spectrum in $n=3-2$ transitions from L-shell partially ionized iron measured with the present EUV spectrometer is shown in Fig.3.6 (a). The spectrum is summed up over twenty temporal frames (100ms integration) to improve the signal-to-noise ratio of relatively weak spectral lines. This spectrum represents the charge state distribution of iron ions in the LHD plasma. Along with the L-shell iron lines, the strong K-shell emission from H-like oxygen (18.97Å, 2p-1s) is also evident. In

order to determine the exact wavelength, the neon spectrum is also recorded as shown in Fig.3.6 (b). The wavelength in the figure is then determined by the interpolation of the OVIII, NeIX and NeX lines. The observed wavelengths are tabulated along with the transitions in Table 3.4. The wavelengths from previous works are also mentioned in the table as noted in [7, 23, 24, 28].

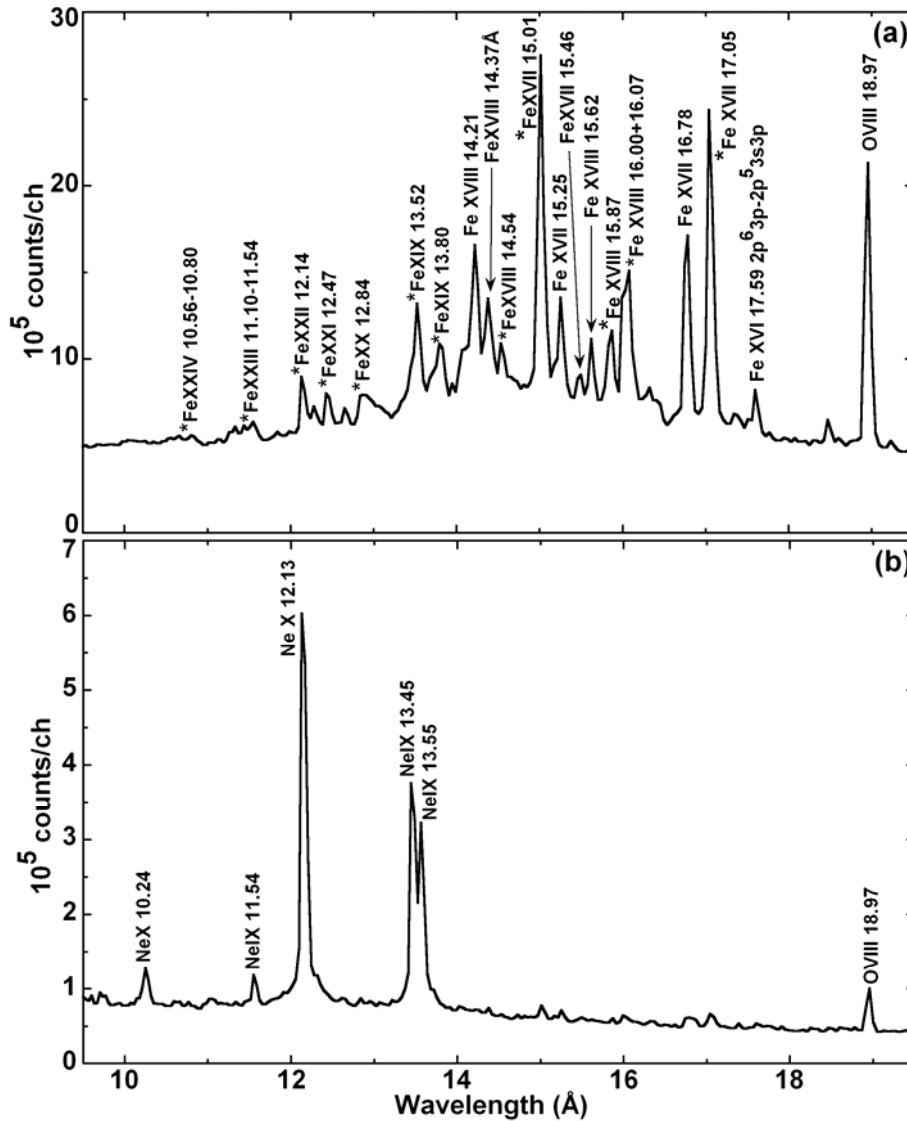


Fig. 3.6 FeXVII-XXIV EUV spectrum of n=3-2 transitions from L-shell partially ionized iron in LHD plasma ($n_e=9\times 10^{19}m^{-3}$, $T_e=0.7keV$). Symbols denoted with * indicate blended lines as discussed in text. Ne EUV spectrum in (b) is shown as marker of wavelength.

Table 3.4 Observed n=3-2 transitions of L-shell partially ionized Fe ions in 10 to 20Å. Only dominant transitions are listed here, but many other possible transitions exist in the same isoelectronic sequence, e.g., FeXXIII. Those are not listed here.

Wavelengths (Å)		Ionization stages	Transitions
Present work	Previous works		
10.56-10.80	10.619 [7]	Fe XXIV	3p-2s
	10.663 [7]		
11.10-11.54	11.018 [7]	Fe XXIII	2s3p-2s ²
	11.442 [7]		2s3d-2s2p
	11.525 [7]		2p3d-2p ²
12.14	12.095 [7]	Fe XXII	2s2p(³ P)3d ² F _{5/2} -2s2p ² ² D _{5/2}
	12.145 [28]	Fe XXI	2p3d ³ P ₁ -2p ³ ³ P ₀
12.47	12.436 [7]	Fe XXI	2p3d ¹ F ₃ -2p ² ¹ D ₂
	12.465 [7]		2p3d ³ D ₁ -2p ² ³ P ₂
12.84	12.836 [7]	Fe XX	2s ² 2p ² (¹ D)3d ² P _{3/2} -2s ² 2p ³ ² D _{5/2}
	12.846 [24]		2s ² 2p ² (³ P)3d ⁴ P _{3/2} -2s ² 2p ³ ⁴ S _{3/2}
	12.857 [28]		2s ² 2p ² (¹ D)3d ² D _{3/2} -2s ² 2p ³ ² D _{3/2}
13.52	13.497 [24]	Fe XIX	2s ² 2p ³ (² D)3d ³ P ₂ -2s ² 2p ⁴ ³ P ₂
	13.518 [24]		2s ² 2p ³ (² D)3d ³ D ₃ -2s ² 2p ⁴ ³ P ₂
13.80	13.795 [28]	Fe XIX	2s ² 2p ³ (⁴ S)3d ³ D ₃ -2s ² 2p ⁴ ³ P ₂
	13.825 [23]	Fe XVII	2s2p ⁶ 3p ¹ P ₁ -2s ² 2p ⁶ ¹ S ₀
14.21	14.203 [24]	Fe XVIII	2s ² 2p ⁴ (¹ D)3d ² D _{5/2} -2s ² 2p ⁵ ² P _{3/2}
14.37	14.373 [28]	Fe XVIII	2s ² 2p ⁴ (³ P)3d ² D _{5/2} -2s ² 2p ⁵ ² P _{3/2}
14.54	14.536 [28]	Fe XVIII	2s ² 2p ⁴ (³ P)3d ² F _{5/2} -2s ² 2p ⁵ ² P _{3/2}
	14.551 [28]		2s ² 2p ⁴ (³ P)3d ⁴ P _{3/2} -2s ² 2p ⁵ ² P _{3/2}
15.01	14.985 [24]	Fe XIX	2s ² 2p ³ (⁴ S)3s ³ S ₁ -2s ² 2p ⁴ ³ P ₂
	15.014 [23]	Fe XVII	2p ⁵ 3d ¹ P ₁ -2p ⁶ ¹ S ₀
15.25	15.261 [23]	Fe XVII	2p ⁵ 3d ³ D ₁ -2p ⁶ ¹ S ₀
15.46	15.451 [23]	Fe XVII	2p ⁵ 3d ³ P ₁ -2p ⁶ ¹ S ₀
15.62	15.623 [28]	Fe XVIII	2s ² 2p ⁴ (¹ D)3s ² D _{5/2} -2s ² 2p ⁵ ² P _{3/2}
15.87	15.826 [28]	Fe XVIII	2s ² 2p ⁴ (³ P)3s ⁴ P _{3/2} -2s ² 2p ⁵ ² P _{3/2}
	15.869 [28]		2s ² 2p ⁴ (¹ D)3s ² D _{3/2} -2s ² 2p ⁵ ² P _{1/2}
16.00	16.003 [28]	Fe XVIII	2s ² 2p ⁴ (³ P)3s ² P _{3/2} -2s ² 2p ⁵ ² P _{3/2}
	16.024 [28]		2s ² 2p ⁴ (³ P)3s ² P _{1/2} -2s ² 2p ⁵ ² P _{1/2}
16.07	16.071 [24]		2s ² 2p ⁴ (³ P)3s ⁴ P _{5/2} -2s ² 2p ⁵ ² P _{3/2}
16.78	16.780 [23]	Fe XVII	2p ⁵ 3s ¹ P ₁ -2p ⁶ ¹ S ₀
17.05	17.051 [23]	Fe XVII	2p ⁵ 3s ³ P ₁ -2p ⁶ ¹ S ₀
	17.096 [23]		2p ⁵ 3s ³ P ₂ -2p ⁶ ¹ S ₀

Most of the lines of the iron spectrum observed here are blended with a few lines. The spectrum was taken when the ruled grating was set in the EUV spectrometer with relatively high spectral resolution than holographic grating. The blended lines are denoted with * in the figure. Detailed explanation on the blended lines is also summarized in Table 3.4. All the possible $n=3-2$ transitions from L-shell partially ionized iron are recorded in the present spectrum. The spectrum is measured from a low electron temperature ($T_e=0.7\text{keV}$) and high electron density ($n_e=9\times 10^{19}\text{m}^{-3}$) plasma produced by several solid H_2 pellet injections, since the iron emission is generally weak in LHD discharges because of its small amount. Then, the intensities from Be-like FeXXIII and Li-like FeXXIV become very weak due to the low electron temperature in addition to the reduction of the spectrometer sensitivity below $\sim 13\text{\AA}$. It is difficult to inject a pure iron impurity pellet at present from a viewpoint of machine protection due to its magnetism.

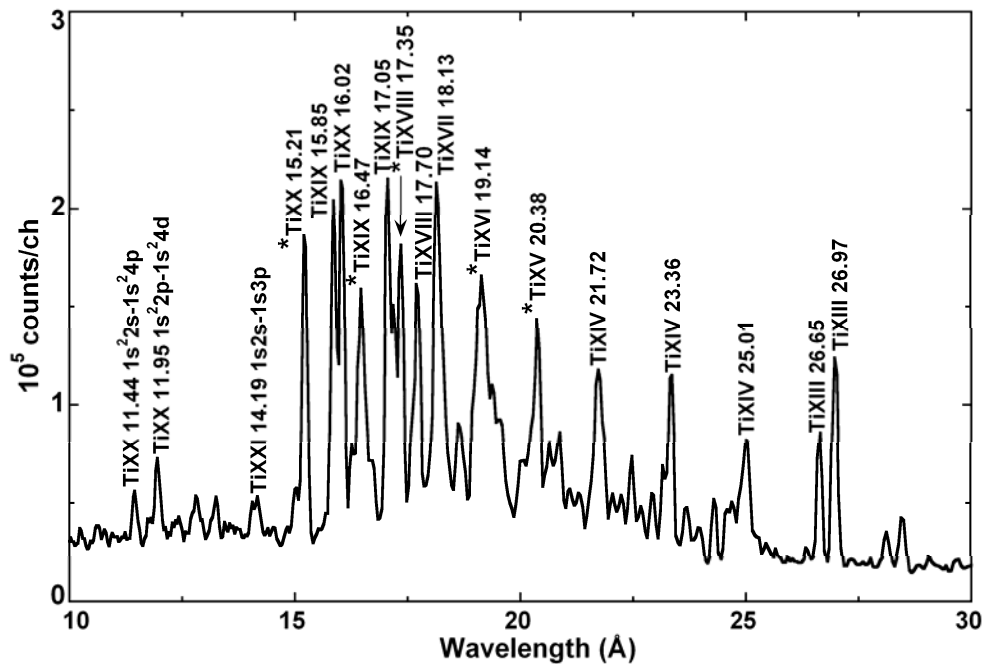


Fig. 3.7 TiXIII-XX EUV spectrum of $n=3-2$ transitions from L-shell partially ionized titanium in LHD plasma with Ti impurity pellet injection ($n_e=1.8\times 10^{19}\text{m}^{-3}$, $T_e=2.3\text{keV}$). Symbols denoted with * indicate blended lines as discussed in text.

Table 3.5 Observed n=3-2 transitions of L-shell partially ionized Ti ions in 10 to 30Å. Only dominant transitions are listed here, but many other possible transitions exist in the same isoelectronic sequence, e.g., TiXIX. Those are not listed here.

Wavelength (Å)		Ionization stages	Transitions
Present work	Previous works		
15.21	15.212 [28]	Ti XX	$3p^2P_{3/2}-2s^2S_{1/2}$
	15.255 [28]		$3p^2P_{1/2}-2s^2S_{1/2}$
15.85	15.865 [28]	Ti XIX	$2s3p^1P_1-2s^2^1S_0$
16.02	16.056 [28]	Ti XX	$3d^2D_{5/2}-2p^2P_{3/2}$
16.47	16.430 [28]	Ti XIX	$2s3d^3D_2-2s2p^3P_1$
	16.440 [7]	Ti XX	$3p^2S_{1/2}-2s^2P_{1/2}$
	16.514 [7]	Ti XIX	$3s^3D_3-2p^2P_{3/2}$
17.05	17.076 [7]	Ti XIX	$2s3d^1D_2-2s2p^1P_1$
17.35	17.354 [28]	Ti XIX	$2p3d^1P_1-2p^2^1S_0$
	17.365 [7]	Ti XVIII	$3d^2D_{5/2}-2p^2P_{3/2}$
17.70	17.715 [7]	Ti XVIII	$2s2p(^3P)3d^2F_{5/2}-2s2p^2D_{3/2}$
18.13	18.127 [7]	Ti XVII	$2p3d^3D_1-2p^2^3P_0$
19.14	19.112 [7]	Ti XVI	$2s^22p^2(^3P)3d^4P_{5/2}-2s^22p^3^4S_{3/2}$
	19.210 [7]	Ti XVI	$2s2p(^1D)3d^2F_{7/2}-2s^22p^3^2D_{5/2}$
20.38	20.389 [7]	Ti XV	$2s^22p^3(^2P)3d^1F_3-2s^22p^4^1D_2$
	20.418 [7]	Ti XV	$2s^22p^3(^2D)3d^3D_3-2s^22p^4^3P_2$
21.72	21.732 [7]	Ti XIV	$2s^22p^4(^1D)3d^2D_{5/2}-2s^22p^5^4P_{3/2}$
23.36	23.328 [7]	Ti XIV	$2s^22p^4(^3P)3d^4P_{1/2}-2s^22p^5^2P_{3/2}$
25.01	25.025 [7]	Ti XIV	$2s^22p^4(^3P)3s^4P_{5/2}-2s^22p^5^2P_{3/2}$
26.65	26.641 [7]	Ti XIII	$2s^22p^5(^2P_{1/2})3s(1/2,1/2)_1-2s^22p^6^1S_0$
26.97	26.960 [7]	Ti XIII	$2s^22p^5(^2P_{3/2})3s(1/2,3/2)_1-2s^22p^6^1S_0$

Titanium spectrum measured with the holographic grating EUV spectrometer is shown in Fig.3.7. A titanium impurity pellet (cylinder size: 0.5mm^φ×0.3mm^l) is injected into the low-density ($n_e=1.8\times 10^{19}m^{-3}$) and high-temperature ($T_e=2.3keV$) NBI plasma using an impurity pellet injector [4] to record the titanium spectrum. All the possible n=3-2 transitions from Ne-like TiXIII to Li-like TiXX are clearly seen in the spectrum. The blended lines are also denoted with * in the figure. The wavelength is determined using the same method as iron. The n=4-2 transitions are excellently detected at shorter

wavelength side (TiXX 4p–2s: 11.451Å, 11.462Å and 4d–2p: 11.957Å) without increase in the background stray light. The detailed description of the observed spectral lines is summarized in Table 3.5. This charge state distribution spectrum based on the n=3-2 transition, which is newly observed with the present 2400grooves/mm EUV spectrometer, will contribute to the spectroscopic diagnostics and impurity transport study in addition to the atomic physics.

References

- [1] G. Federici et al., Nucl. Fusion **71**, 1967 (2001).
- [2] K. Asmussen et al., Nucl. Fusion **38**, 967 (1998).
- [3] M. J. May et al., Nucl. Fusion **37**, 881 (1997).
- [4] H. Nozato, S. Morita, M. Goto et al., Rev. Sci. Instrum. **74**, 2032 (2003).
- [5] M. B. Chowdhuri, S. Morita, M. Goto et al., Rev. Sci. Instrum. **78**, 023501 (2007).
- [6] R. Katai, S. Morita, M. Goto et al., Jpn. J. Appl. Phys **46**, 36667 (2007).
- [7] Yu. Ralchenko et al., NIST Atomic Spectra Database (version 3.1.1), Online, (2008), http://physics.nist.gov/PhysRefData/ASD/lines_form.html.
- [8] C. Jupen et al., Physica Scripta. **68**, 230 (2003).
- [9] A. Wouters et al., J. Opt. Soc. Am. B **5**, 1520 (1988).
- [10] M. Finkenthal et al., J. Phys. B: At. Mol. Phys. **18**, 4393 (1985).
- [11] J. Sugar et al., J. Opt. Soc. Am. B **8**, 22 (1991).
- [12] J. Sugar et al., Phys. Rev. A **51**, 835 (1995).
- [13] R. C. Isler et al., Phys. Letters **63A**, 295 (1977).
- [14] E. Hinnov and M. Mitterli, Phys. Letters **66A**, 109 (1978).
- [15] J. Sugar et al., J. Opt. Soc. Am. B **10**, 799 (1993).
- [16] J. Sugar et al., J. Opt. Soc. Am. B **10**, 1321, (1993).
- [17] J. Sugar et al., J. Opt. Soc. Am. B **10**, 1977 (1993).
- [18] M. Finkenthal et al., Phys. Letters A **127**, 255 (1988).
- [19] J. Sugar and V. Kaufman, Phys. Rev. A **21**, 2096 (1980).
- [20] M. B. Chowdhuri, S. Morita and M. Goto, Appl. Opt. **47**, 135 (2008).
- [21] J. H. Parkinson, Astron. Astrophys. **24**, 215 (1973).
- [22] K. J. H. Phillips et al., Astrophys. Suppl. Ser. **138**, 381 (1999).
- [23] G. V. Brown et al., Astrophys. J. **502**, 1015 (1998).
- [24] G. V. Brown et al., Astrophys. J. Suppl. Ser. **140**, 589 (2002).
- [25] P. Beiersdorfer et al., Phys. Rev. A **64**, 032705 (2001).
- [26] K. J. H. Phillips et al., Astron Astrophys. **324**, 381 (1997).
- [27] S. B. Utter et al., Rev. Sci. Instrum. **70**, 284 (1999).
- [28] R. L. Kelly, J. Phys. Chem. Ref. Data **16**, 1 (1987).

Chapter 4

Analysis on carbon behaviors in LHD

4.1. CIII to CVI behavior during recombining phase

4.1.1. Introduction

For the study of impurity behaviour in high-temperature plasmas, impurity densities in each charge state are usually analyzed using spectral absolute intensities measured from spectroscopic diagnostics in combination with one-dimensional impurity transport code [1]. It evaluates radial profiles of ion density and emissivity in all charge states based on measured electron density and temperature profiles. In general, the impurity transport studies have been done during the steady state phase of discharges using either of intrinsic or extrinsic impurity particles [2-5]. When the impurity time behaviour is analyzed at the transient phase, especially the plasma termination phase, the time duration is very short in the case of tokamaks because of the abrupt disruption after the current termination. Even if the toroidal current is controlled for the smooth termination of the plasma, the magnetic field topology and resultant magnetic surface structure change so much as a function of time. In the stellarator cases, on the other hand, the magnetic field for the confinement is externally supplied and maintains steadily even during the transient phase of the discharges. The temporal evolution of the impurity emissions from such plasmas can be easily computed under the presence of steady magnetic surface.

In the Large Helical Device (LHD) the helical magnetic field for plasma confinement produced by superconducting magnetic coils makes possible the steady state operation. The analysis is therefore possible on the transient period at initial and final phases of the discharges. Therefore, the temporal behavior of edge carbon emissions is studied during the recombination phase of the LHD discharges through a comparison

between the experimental and calculated radiated powers from different ionization stages of carbon.

It is well known that the enhancement of particle and energy transport by the stochastic magnetic field structure at the plasma edge, such as ergodic layer in the LHD, should lead to a reduction of impurity content in the plasma [6]. During the recombining phase, the electron temperature quickly decreases due to the absence of the heating source and the plasma gradually shrinks inside the last closed flux surface (LCFS) before the termination. Then, the role of ergodic layer on edge impurity transport is likely to be different during recombining and steady state phases of the discharges. In this context, carbon emissions from different ionization stages have been analyzed with electron density during steady state and recombining phases of plasmas to examine the role of ergodic layer on the behaviour of edge carbon emissions.

4.1.2. Experimental Setup

The experiment has been conducted with inwardly shifted configuration of $R_{ax}=3.6\text{m}$ and $B_0=2.75\text{T}$. A discharge is initiated by electron cyclotron heating (ECH) and the plasma is sustained by three negative-ion-based neutral beam injection (NBI) devices. Several spectroscopic diagnostics covering visible to X-ray wavelength ranges have been installed to monitor and study the impurity behaviour of LHD discharges. In the present study, emissions from different ionization stages of carbon have been measured using two extreme ultraviolet (EUV) spectrometers [7, 8] and two vacuum ultraviolet (VUV) monochromators [9]. Two absolutely calibrated EUV spectrometers cover 10–130Å (EUV_Short) and 50–500Å (EUV_Long) wavelength range, respectively. Back-illuminated VUV sensitive charge couple device (CCD) detectors are mounted with two EUV spectrometers and operated in full binning mode. Data from the CCD have been acquired in every 5 ms. Four resonance transitions of CIII (977Å, $2s2p\ ^1P-2s^2\ ^1S$), CIV (1548Å, $2p\ ^2P-2s\ ^2S$), CV (40.27Å, $1s2p\ ^1P-1s^2\ ^1S$) and CVI (33.73Å, $2p\ ^2P-1s\ ^2S$) are mainly monitored for this study. The CV and CVI emissions are measured using the EUV_Short spectrometer with a spectral resolution of $\sim 0.10\text{Å}$ at 40Å. The resonance

transitions from Li- (CIV) and Be-like (CIII) carbon ions are observed using two 20cm normal incidence VUV monochromators equipped with electron multiplier tube detectors. The signal is acquired with time interval of 100 μ s. The two VUV monochromators were absolutely calibrated using the carbon emissions by comparing the raw signals with the absolutely calibrated EUV_Long spectrometer for 50–500Å. Two experimental intensity ratios of 2s3p–2s² (386.4Å) to 2s2p–2s² (977Å) transitions from CIII and of 3p–2s (312.4Å) to 2p–2s (1548Å) transitions from CIV were adopted for the calibration. Electron temperature and density profiles measured with Thomson diagnostics and line-integrated electron density measured with FIR diagnostics are used for the present analysis.

4.1.3. Description of Calculation

Analysis on temporal behaviors of carbon emissions in different ionization stages are based on the calculation of the line-integrated emissivity using one-dimensional impurity transport code [1]. The time behavior of the impurity density profile is calculated by the following equation with the ionization balance of an impurity ion;

$$\frac{\partial n_q}{\partial t} = -\frac{1}{r} \frac{\partial}{\partial r} (r\Gamma_q) + \alpha_{q-1} n_{q-1} n_e + \beta_{q+1} n_{q+1} n_e - (\alpha_q + \beta_q) n_q n_e, \quad (4.1)$$

where n_q and Γ_q are the ion density and particle flux of qth charge state, respectively. The parameters of α and β represent the ionization and recombination rate coefficients, respectively. The empirical transport model [10], of which the validity was confirmed in LHD, using the diffusion coefficient D and convective velocity V is given by

$$\Gamma_q = -D_q(r) \frac{\partial n_q}{\partial r} + V_q(r) n_q, \quad (4.2)$$

$$\text{and } V_q(r) = V(a) \frac{r}{a}. \quad (4.3)$$

Here, a , D_q and V_q are the plasma radius, diffusion coefficient and convective velocity, respectively.

After the charge state calculation, the emissivity and brightness profiles of emission line were evaluated. The emissivity of transition from level j to i , $\epsilon(j, i)$, is expressed by the relation of $\epsilon(j, i) = N_q(j)A(j, i)$, where $A(j, i)$ is the transition probability and $N_q(j)$ is the density of the upper level j in charge state q . The emissivity is calculated from the level population in the upper level. The level population is generally determined by the collisional and radiative processes among several quantum levels [11]. However, the coronal model is assumed in the present case for the simplicity. This assumption really gives a good agreement with the C-R model calculation, at least, for the H- and He-like systems. Therefore, the relation can be written as $\epsilon(j, i) = N_q(j)A(j, i) = n_q n_e Q(i, j)$, where $Q(i, j)$ is the excitation rate coefficient for the transition of i to j . The excitation rate coefficient for individual line has been taken from calculated results by Itikawa et al. [12].

4.1.4. Results and Discussions

4.1.4.1 Temporal evolution of carbon emissions during recombining phase

A typical waveform of NBI discharge used in the present impurity study is shown in Fig.4.1. The time evolution of carbon emissions has been analyzed at the recombining phase from 2.45s to the end of the plasma termination, where the electron temperature, T_e , quickly decreases due to the absence of the heating source while the n_e stays constant. The central electron temperature, $T_e(0)$, measured by Thomson scattering diagnostic was available until $t=2.62$ s. The CV and CVI emissions, on the other hand, dropped to zero at 2.628s, and the CIII and CIV emissions disappeared at 15 ms later because of their low ionization energies (I.E.) (CIII: 48eV, CIV: 64eV, CV: 392eV and CVI: 490eV). Extrapolation of the measured T_e was therefore necessary to calculate the emissivity of the carbon emissions in different ionization stages. The T_e was calculated from magnetic energy and line-averaged electron density $\langle n_e \rangle$. The measured and extrapolated $T_e(0)$ and plasma radius r_b at horizontally elongated plasma cross section are plotted in Fig.4.2.

The $T_e(0)$ and the plasma radius gradually decrease, and after $t=2.55s$ the $T_e(0)$ begins to drop quickly. The CIII and CIV emissions also start to increase rapidly at $t=2.55s$.

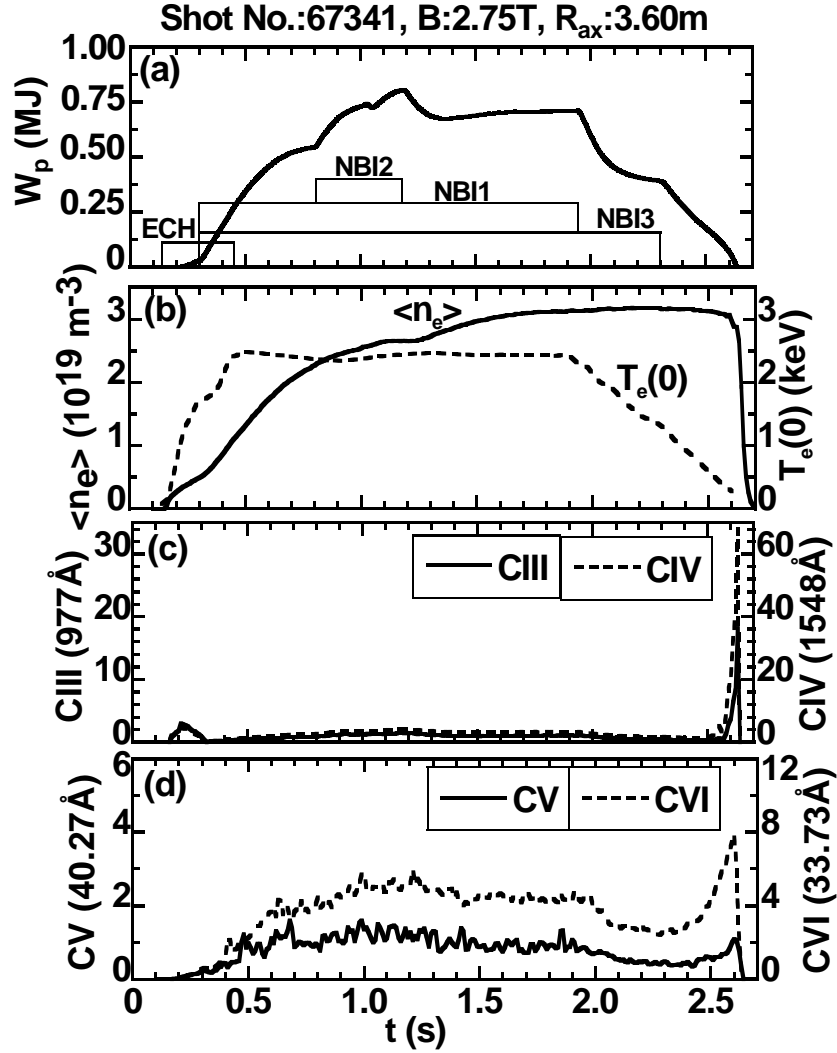


Fig. 4.1 Typical discharge for the present analysis; (a) plasma stored energy and NBI heating pulses, (b) line-averaged electron density (solid line) and central electron temperature (dashed line), (c) CIII (solid line) and CIV (dashed line) emissions and (d) CV (solid line) and CVI (dashed line) emissions. All carbon emissions have unit of 10^{14} photons.cm⁻².sr⁻¹.s⁻¹. Data between $t=2.45$ to $2.65s$ are used for analysis.

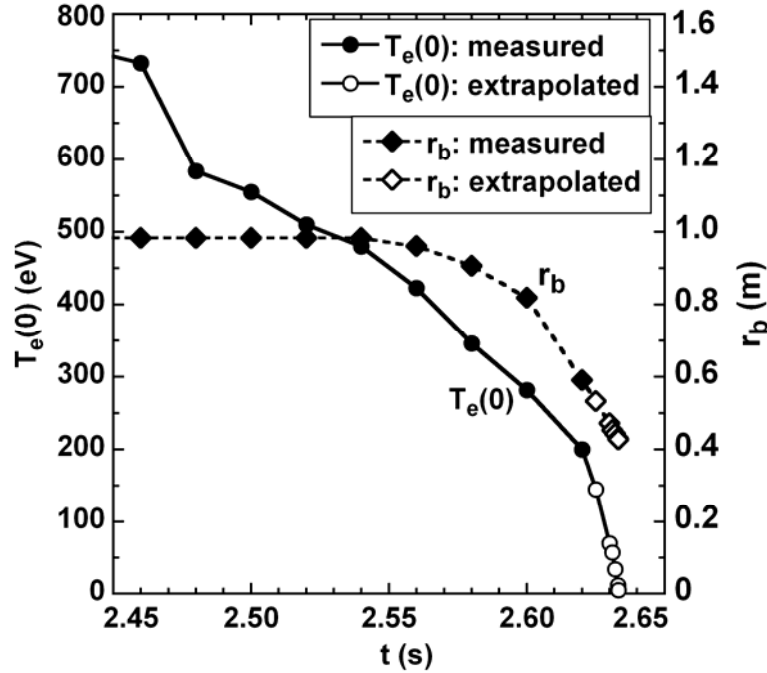


Fig. 4.2 Time behaviors of central electron temperature ($T_e(0)$: circles) and horizontal plasma radius (r_b : diamonds) at horizontally elongated plasma cross section during recombining phase. Closed circles and diamonds mean measured values, and open circles and diamonds mean extrapolated values.

Temporal evolution of carbon emissions during the recombining phase has been calculated using one-dimensional impurity transport code. The calculation has been done on the averaged magnetic surface by replacing the elliptical shape of LHD plasmas with the circular shape. In this study the diffusion coefficient D_q is considered as an independent of q and r , and the inward convection velocity V_q is considered as a linear function of r . Here, the maximum value of V_q is given as $V(a)$ at average plasma radius, a (see Eq.4.3). The values of D_q and $V(a)$ are taken to be $0.2\text{m}^2\text{s}^{-1}$ and 1.0ms^{-1} for diffusion coefficient and inward convective velocity, respectively.

Figure 4.3 illustrates the total radiation power emitted from Be-like CIII to H-like CVI, which are obtained by integrating the whole plasma surface of LHD. The experimental and calculated results are indicated with solid and dashed lines, respectively. In the calculation 3% carbon density is assumed to the electron density. All the carbon radiations gradually increase after turning off the heating power at $t=2.3\text{s}$ as the T_e

decreases. At first the CVI emissions reach the peak value at 2.60s where the $T_e(0)$ is 280eV. This is in good agreement with the calculation. Then, the CV and CVI radiations quickly decrease and become zero immediately at 2.625s. At this moment the $T_e(0)$ drops less than 150eV. The calculation of CV and CVI radiations also drop at 2.630s. Since the exposure time of CCD detector is 5ms in the present experiment, the difference between measurement and calculation may originate in the uncertainty of time window.

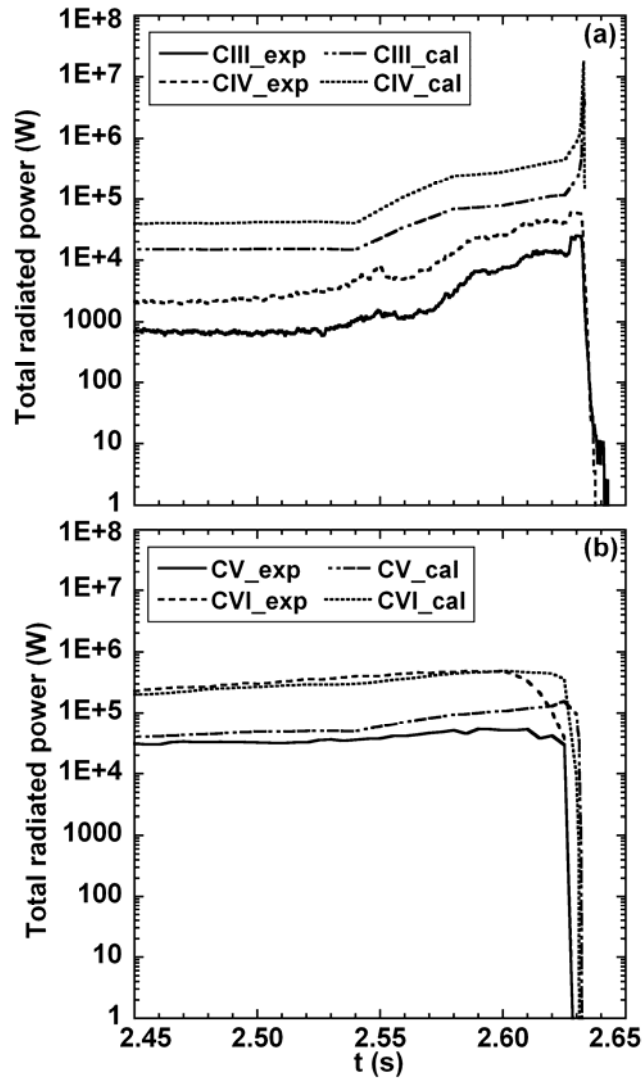


Fig. 4.3 Calculated and experimental total radiation power of (a) CIII and CIV and (b) CV and CVI. Solid (CIII and CV) and dashed (CIV and CVI) lines are experimental data. Dashed-dotted (CIII and CV) and dotted (CIV and CVI) lines indicate calculated data.

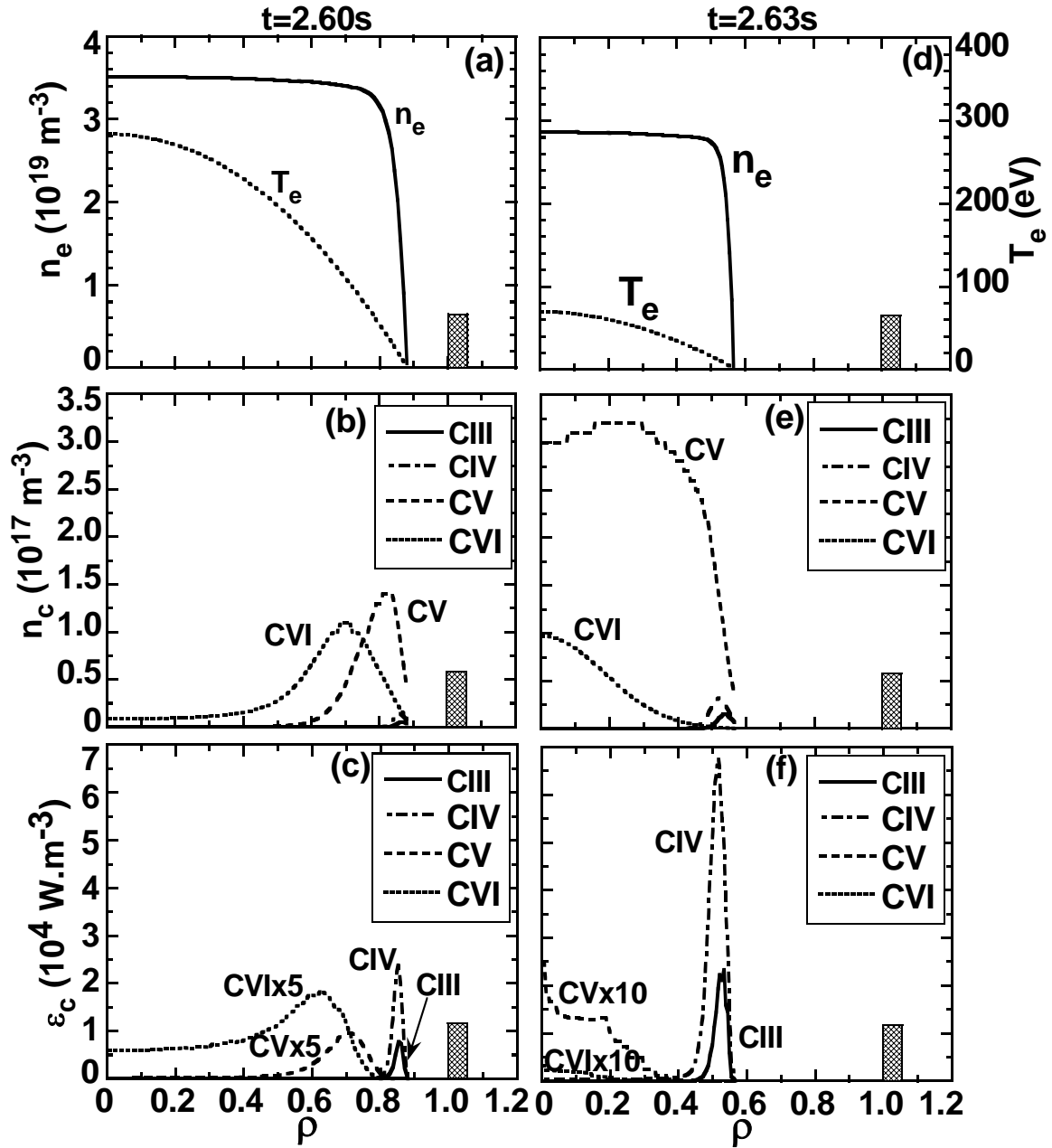


Fig. 4.4 Radial profiles of n_e and T_e ((a) and ((d)), densities ((b) and (e)) and emissivities ((c) and (f)) of CIII to CVI taken at two different time frames of 2.60 and 2.63s, respectively. Horizontal axis means normalized radius, ρ . Hatched area indicates ergodic layer outside the LCFS.

On the other hand, signal dynamic range of the CIII and CIV emissions is really large compared to the CV and CVI cases. The voltage applied to the secondary electron multiplier (SEM) is always adjusted to monitor the main discharges, not the plasma termination phase. Then, the signals of CIII and CIV are always saturated at the plasma termination phase as seen during $t=2.628\text{--}2.632\text{s}$ in the figure. The calculation on CIII and CIV radiations reaches the peak value at 2.632s when the $T_e(0)$ becomes 12eV . The calculation after 2.633s is, however, practically impossible because of the extremely low electron temperature. In the discharge very low temperature plasma is maintained until $t=2.645\text{s}$ as apparently seen in the CIII temporal behavior.

During the steady state phase of discharges the carbon emissions are basically located inside the narrow shell at plasma edge. In LHD the CIII and CIV generally exist in the ergodic layer [13] surrounding the main plasma and the CV and CVI exist near the LCFS. During the recombining phase the width of such emission shells is broaden as the T_e decreases, and moves inside because of the reduction in the plasma size, as shown in Fig.4.2. Calculated results on the radial profiles of carbon densities and emissivities are shown in Fig. 4.4. Figures 4.4 (a)–(c) and (d)–(f) are the radial profiles at $t=2.60$ and 2.63s in Fig. 4.3, respectively. The position of the ergodic layer is shown by hatched area outside the LCFS ($\rho=1$). It can be seen from the figure that the emission shells of CIII to CVI move inside the LCFS at these times since the plasma size has been reduced. The CVI emission takes the maximum value at 2.60s and the CV and CVI entirely disappear at 2.63s . Figures 4.4 (a) and (d) are the measured n_e and T_e profiles used in the calculation. The CIII and CIV are always located at the plasma edge in these time frames with sharp peaks.

On the other hand, the CV and CVI emission profiles are quite different. At $t=2.60\text{ s}$ the shell widths of the CV and CVI densities become wider (see Fig.4.4 (b)), and resultant emission profiles also become much wider (see Fig.4.4 (c)). Especially the tendency is remarkable to the CVI emission profile, because the excitation rate coefficient of CVI quickly drops at $T_e < 200\text{eV}$. This effect can be seen in the difference between the peak positions of CVI density profile ($\rho=0.67$ in Fig.4.4 (b)) and emissivity profile ($\rho=0.63$ in Fig.4.4 (c)).

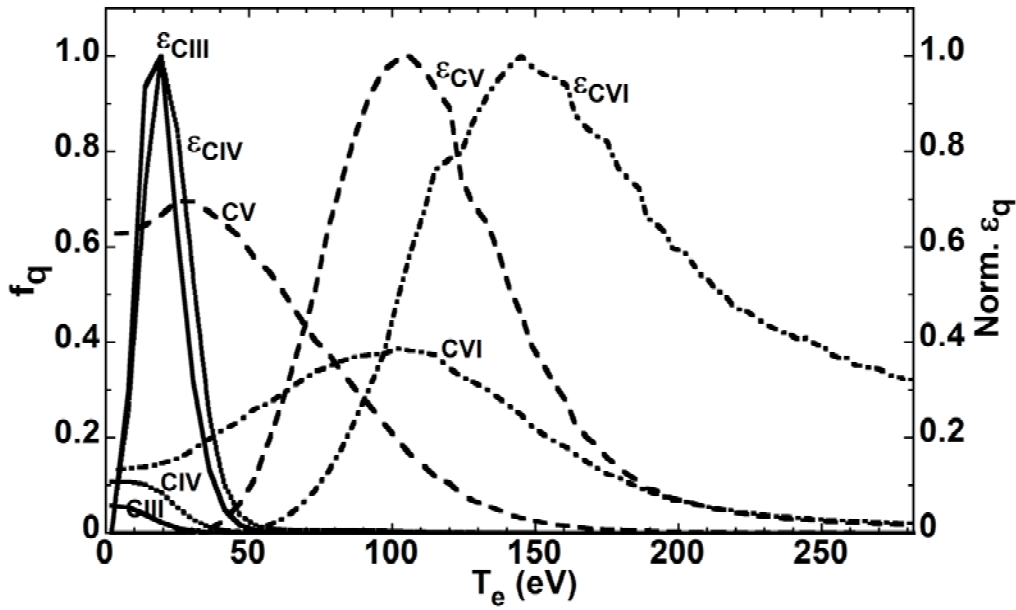


Fig. 4.5 Fractional abundance (f_q) and emissivity (Norm. ϵ_q) plotted with T_e for CIII (solid line), CIV (dotted line), CV (dashed line) and CVI (dashed-dotted line) at $t=2.60s$. Notations of CIII to CVI and e CIII to e CVI indicate fractional abundance and emissivity of each charge state, respectively. Emissivity is normalized by its peak value.

Figure 4.5 shows the fractional abundances and the emissivities for CIII to CVI at $t=2.60s$. In the figure horizontal axis in Figs.4.4 (b) and (c) is replaced by the T_e . Here, the emissivity of individual charge state is normalized to its peak value. It can be seen that the peak of the CVI density profile occurs at $T_e=105eV$ ($\rho=0.67$) while the peak of the emissivity profile, e CVI, appears at $T_e=150eV$ ($\rho=0.63$). At $t=2.63s$ the CV and CVI emissions entirely disappear as seen in Fig.4.4 (f), whereas the CV and CVI densities increase at the plasma center (see Fig.4.4 (e)). The excitation rate coefficient of CVI at Fig.4.4 (f) ($1.97 \times 10^{-18} m^3 \cdot s^{-1}$ at $T_e(0)=70eV$) is 33 times less than Fig.4.4 (c) case ($6.69 \times 10^{-17} m^3 \cdot s^{-1}$ at $T_e(0) = 280eV$).

The calculation of the total radiation power from the CV and CVI shows the good agreement with the experiment under evaluation of 3% carbon density. However, the CIII and CIV results are ten times larger than the experimental values. The reason is not

fully clear at present. At least, it is known that the emission distribution from low ionized ions and neutral atoms is toroidally and poloidally inhomogeneous because of the presence of the ergodic layer. Indeed, recent studies indicate that the emissions from CIII and CIV have the asymmetric features reflecting the field line structure of the ergodic layer. Especially, the vertical profile of CIV exhibits four peaks. The four peaks are formed at the inboard side near the X-point in addition to the top and bottom edge peaks at the horizontally elongated plasma cross section [14]. It is reported that the particle recycling is enhanced at the inboard side [15]. It is also observed that the inhomogeneous poloidal distribution of the neutral emissions arises mainly from the inhomogeneity in the neutral particle density, not from the nonuniformity of the electron temperature and density [16]. This is likely to be one of the reasons for the difference.

4.1.4.2 Density dependence of carbon emissions during recombining and steady state phases

Finally the CVI emission is examined for several discharges at the peak value during the recombining phase, where the plasma begins to shrink and the size becomes a little smaller than the LCFS. The CVI emission during the steady-state phase is also studied for the comparison. Intensities of CVI are plotted against $\langle n_e \rangle$, as shown in Figs.4.6 (a) and (b) for the recombining and steady state phases, respectively. CVI intensities normalized to the density and excitation rate coefficient ($CVI/(n_e Q)$), which means the CVI density, are also plotted in the figures. The excitation rate coefficient is calculated against the electron temperature at the LCFS for steady state phase and at the central electron temperature for recombining phase. This choice is reasonably correct since the CVI emission location is estimated from the CV radial profile. The difference between the two phases is very clear. The CVI intensities from the recombining phase increase with $\langle n_e \rangle$ but those from the steady state phase decrease with $\langle n_e \rangle$. Thus, we find a clear difference in the carbon density behavior with $\langle n_e \rangle$. That is to say, the CVI density is nearly constant with $\langle n_e \rangle$ for the recombining phase, but it definitely decreases with $\langle n_e \rangle$ for the steady state phase.

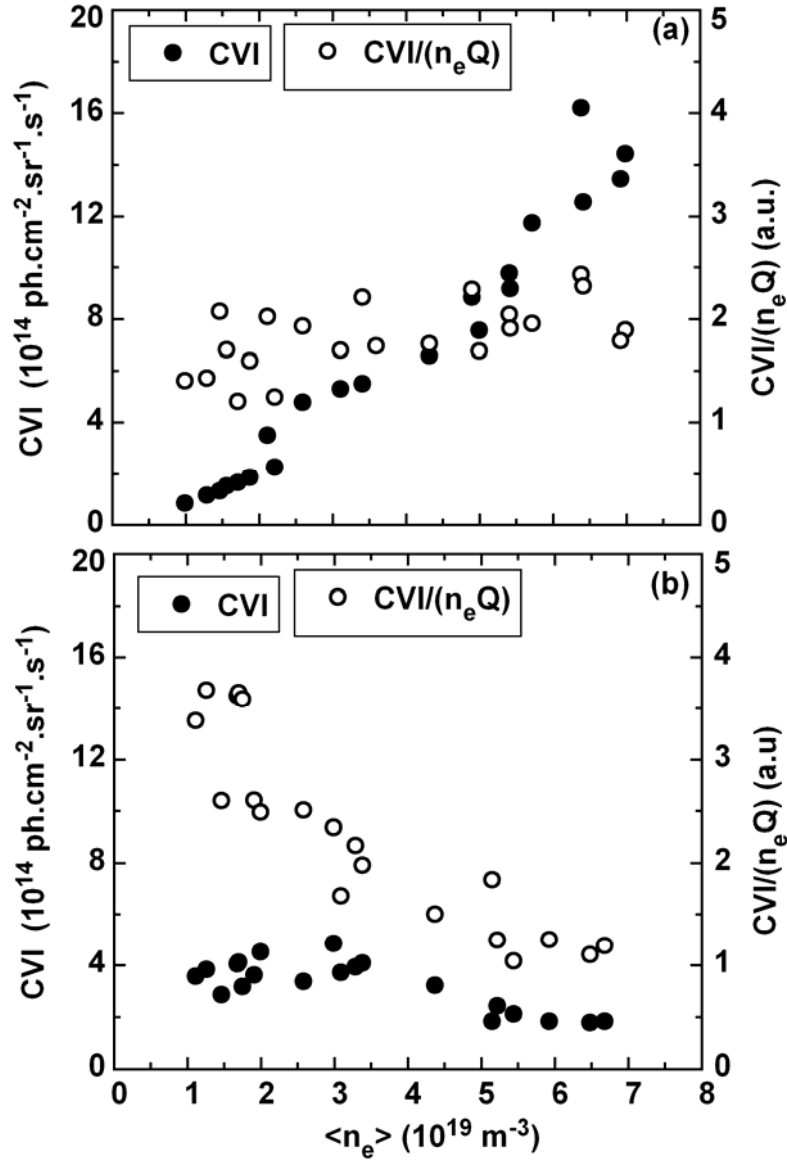


Fig. 4.6 CVI intensity (closed circles) and $CVI/(n_e Q)$ (open circles) plotted against line-averaged electron density $\langle n_e \rangle$ for (a) recombining and (b) steady state phases. Value of Q means excitation rate coefficient of CVI.

CV emissions and densities also follow a similar trend to CVI as shown in Figs.4.7 (a) and (b) for the recombining and steady state phases, respectively. The CV intensities increase with $\langle n_e \rangle$ during the recombining phase while it is nearly constant during the steady state phase. On the other hand, the CIII intensities, which suggest the carbon influx for the ionizing plasma like during steady state phase, increase with $\langle n_e \rangle$

for both phases, as shown in Fig.4.8. The CIII intensities for recombining phase are saturated at densities greater than $5 \times 10^{19} \text{m}^{-3}$. The intensities of CIV also show the same tendency as depicted in Fig.4.9 and are saturated at densities greater than $3.5 \times 10^{19} \text{m}^{-3}$. The reduction of the CV and CVI densities for the steady state phase may suggest the impurity screening effect. Increasing the density in the ergodic layer, the friction force becomes large, which leads to the impurity screening. In case of the recombining phase, the understanding of carbon emissions is not really simple, because the CIII emissions do not indicate simply the influx. In addition, the origin of the carbon source is very unclear since the plasma shrinks and is completely detached from the divertor plates and vacuum wall. We need further investigation on the study of carbon behavior during the recombining phase.

4.1.5. Summary

Temporal evolution of carbon emissions during the recombining phase of the discharges has been studied through the calculation of the spectral emissivity using one dimensional transport code. From the calculation of CV and CVI emissions it indicates that the carbon density is 3% to the electron density. The difference between density and emission locations as a function of T_e has been studied for CV and CVI. The discrepancy between computed and experimental CIII and CIV emissions has been found. Although the reason behind this is not fully clear it is argued that the three dimensional structure of CIII and CIV emissions might be responsible for the differences.

Comparison of CV and CVI emissions during steady state and recombining phase reveal its different dependence with n_e . Both intensities increase with n_e during the recombining phase but remain nearly constant during the steady state phase. On the other hand, the CIII and CIV intensities increase with n_e in the both phases. From this observation it is suggested that impurity screening effect is enhanced with n_e during the steady state phase and it disappears during the recombining phase.

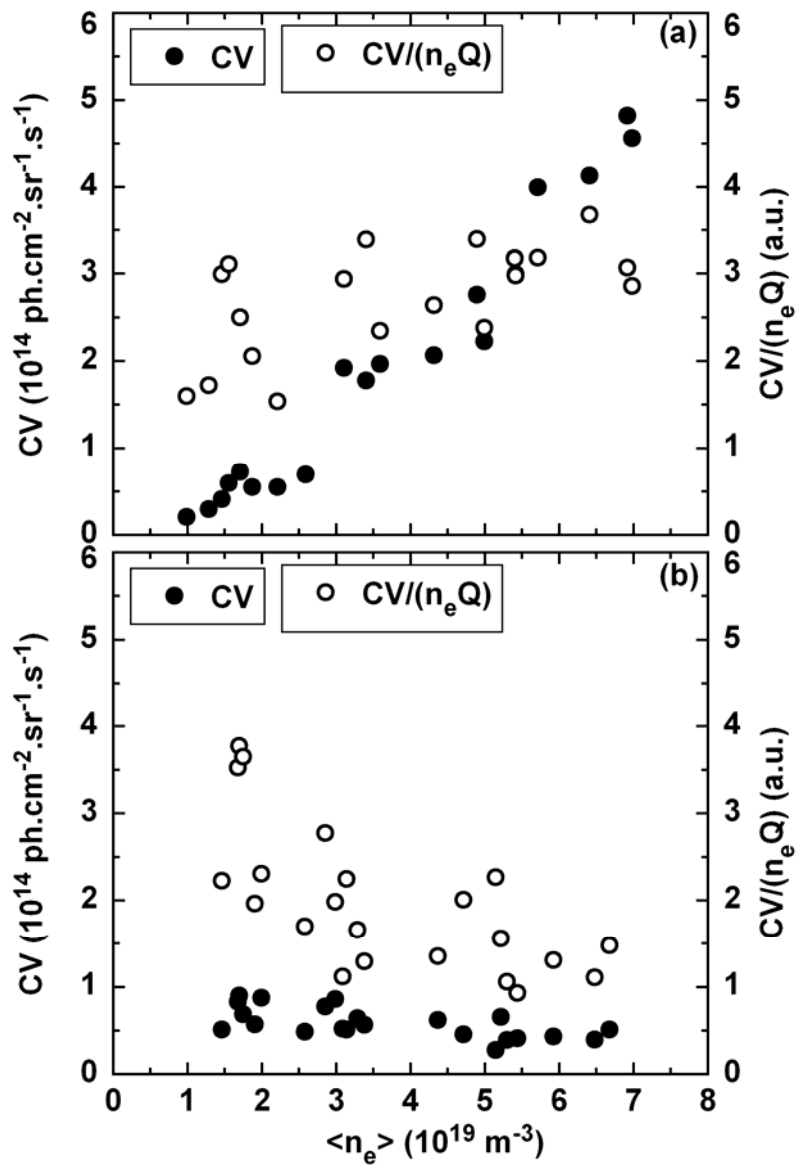


Fig. 4.7 CV intensity (closed circles) and $\text{CV}/(n_e Q)$ (open circles) plotted against line-averaged electron density $\langle n_e \rangle$ for (a) recombining and (b) steady state phases. Value of Q means excitation rate coefficient of CV.

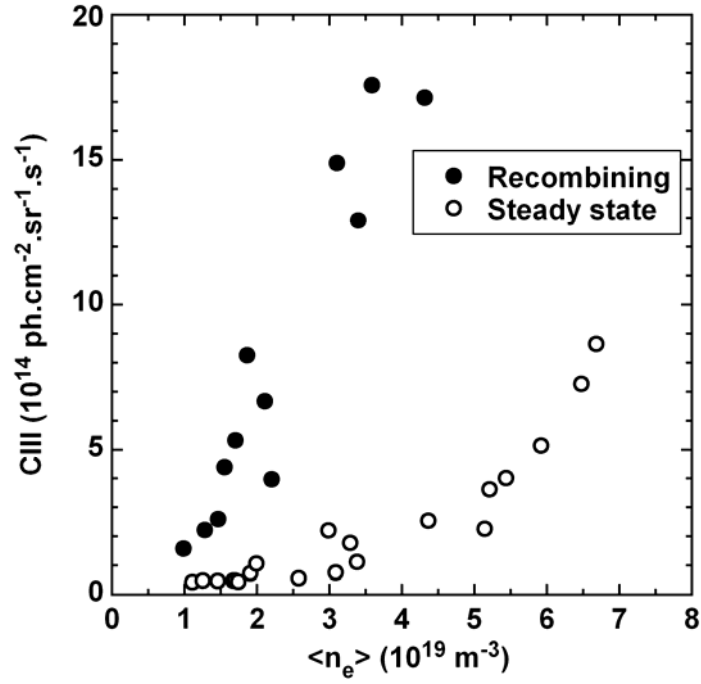


Fig. 4.8 CIII intensity against line-averaged electron density $\langle n_e \rangle$ for recombining (closed circles) and steady state phases (open circles).

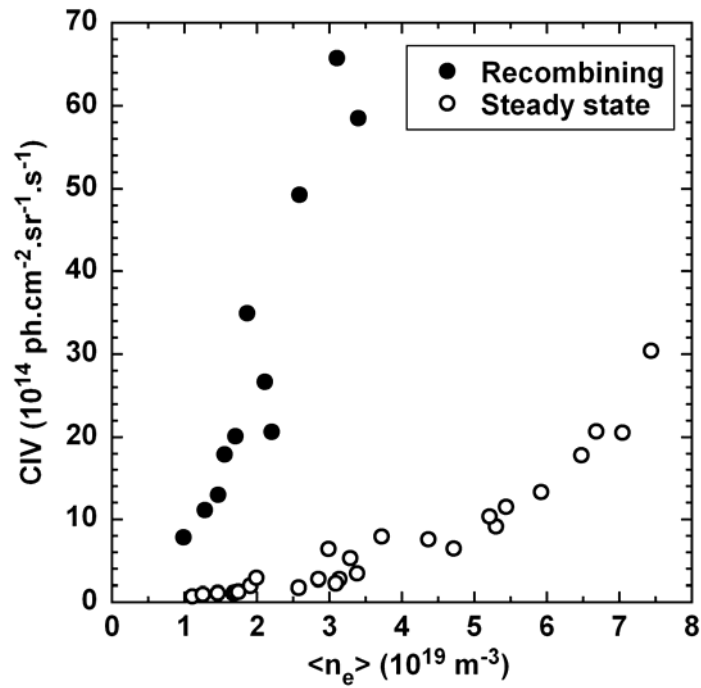


Fig. 4.9 CIV intensity against line-averaged electron density $\langle n_e \rangle$ for recombining (closed circles) and steady state phases (open circles).

4.2. Edge impurity transport study of plasmas with ergodic layer using CIII to CVI

4.2.1. Introduction

Edge particle control including impurity is one of important key issues in fusion research with relation to confinement improvement and divertor heat flux control. The impurity control becomes also important from view points of enhancement of bremsstrahlung emission in high-density operation in addition to the dilution of fuel ions and radiation loss. Active impurity control was done using an axis-symmetric poloidal divertor configuration [17], where the particles outflux is directed into a region separated from the main plasma. Another approach of the active impurity control was the stochastization of edge magnetic fields using resonant perturbations [18]. Such perturbations could ergodise the magnetic field lines by overlapping edge magnetic islands. It is reported that the enhancement of edge particle and energy transport by the stochastic magnetic fields should lead to a reduction of impurity content in the core plasma [6].

In tokamak devices, the effect of such a stochastic magnetic field structure has been generally studied using externally supplied magnetic field coils as mentioned above, i.e., perturbation field on DIII-D [19], ergodic divertor (ED) on Tore Supra [20] and dynamic ergodic divertor (DED) on TEXTOR [21]. In DIII-D, the effect of stochastization has been mainly studied on controls of divertor heat flux enhanced by ELM (edge localized mode) and pedestal profile [22]. On the other hand, extensive studies on the impurity behavior due to ergodization of the edge magnetic fields have been carried out in the Tore Supra. In Tore Supra the activation of ED led to a significant reduction in the concentration of intrinsic impurities and the appreciable enhancement of its radiation from the plasma edge [23]. The ED differently affected according to each ionization state of highly charged impurity ions [24]. In TEXTOR, the decontamination of highly ionized carbon in the plasma core was observed during DED operation [25]. These experimental results clearly suggest the importance of the impurity transport in the stochastic magnetic field layer where collisions with background particles are mainly dominant [26].

In helical devices such as Large Helical Device (LHD) [13], on the other hand, the edge magnetic fields become intrinsically stochastic. The edge plasma is therefore characterized by the presence of thick stochastic magnetic field layer surrounding the plasma core, which is called ergodic layer [27]. The properties of the ergodic layer can be changed with the magnetic axis shift by vertical magnetic field and deformation of plasma shape by quadrupole magnetic field. It is interesting to study the edge impurity behavior in LHD related to the static ergodic layer formed by only the steady superconducting magnetic coils, which is entirely different from the tokamak case [28].

The edge particle and impurity study has been started with the beginning of LHD experiment using limiter experiment [29], and has been progressed with developments of several diagnostic tools and computer simulation code. In this section the edge impurity transport has been studied using the spectral emissions from carbon, which is the primary impurity in LHD as well as other fusion devices.

4.2.2. LHD edge magnetic structure

LHD is a superconducting device with major and average minor radii of $R=3.60$ and $a=0.64\text{m}$, respectively. The magnetic field for the confinement is produced and sustained by a pair of continuous helical coils and pairs of outer vertical, inner vertical and inner shaping coils. Toroidal and poloidal pitch numbers of the helical coils are $M/\ell=10/2$, respectively. Ten pairs of local island divertor (LID) [30] normal conducting coils are set at the top and bottom ports of all vertically elongated plasma cross sections. These LID coils are basically used for the cancellation or expansion of $m/n=1/1$ island. The plasma axis position, which makes a remarkable change in both structures of the magnetic surface and the ergodic layer, can be moved horizontally by changing the vertical field due to outer and inner vertical coils. The schematic views of LHD magnetic configurations at horizontally elongated cross sections of $R_{ax} = 3.60$ and 4.00m are shown in Figs.4.10 (a) and (b), respectively. The elliptical magnetic flux surfaces appear inside the last closed flux surface (LCFS). The position of LCFS in LHD is defined by the

outermost flux surface on which the deviation of the magnetic field line is less than 4mm while it travels 100 turns along the torus.

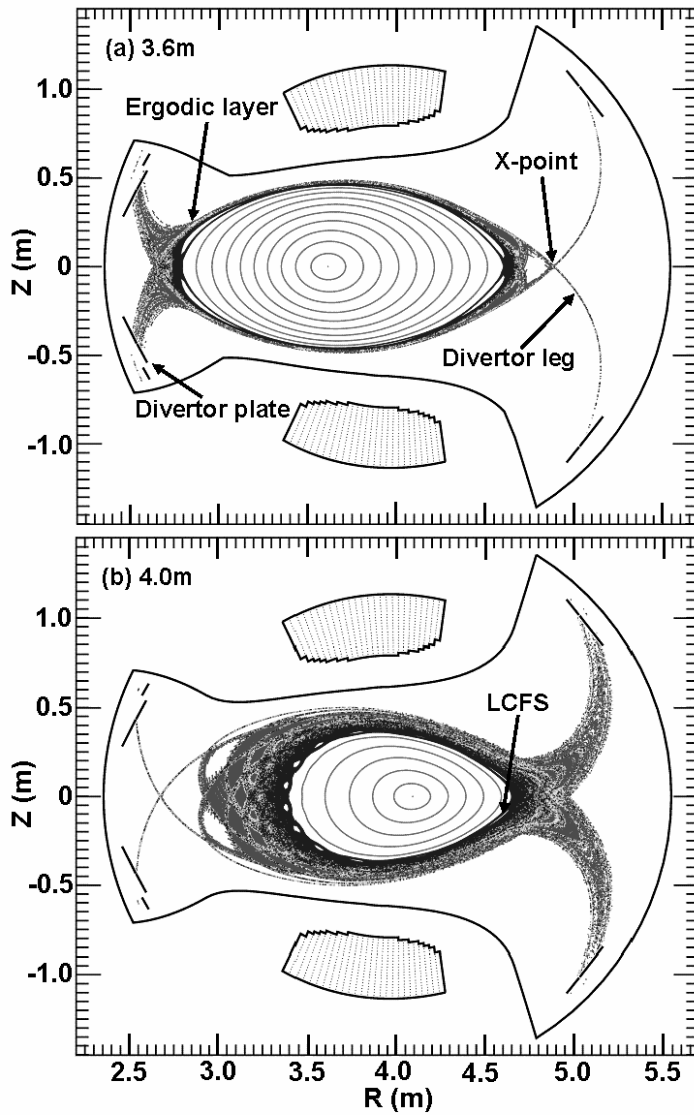


Fig. 4.10 Schematic views of horizontally elongated plasma cross section in (a) $R_{ax}=3.6$ and (b) 4.0m of LHD. Major radius and vertical distance are indicated by R and Z , respectively. Position of $Z=0$ means equatorial plane.

The LCFS is surrounded by the ergodic layer. The ergodic layer is naturally formed by overlapping magnetic islands with many modes based on radial magnetic field arising from the helical coils. The volume of the ergodic layer is quite large in $R_{ax}=4.00\text{m}$ compared with $R_{ax}=3.60\text{m}$ as indicated in Fig.4.10. The thickness of the

ergodic layer varies with the poloidal angle. The thickness becomes the minimum at the O-points located near the helical coils, e.g., 1-2cm for $R_{ax}=3.60\text{m}$. The ergodic layer typically consists of stochastic magnetic field lines with lengths of 10-2000m, which correspond to 0.5-100 toroidal turns of the torus. The thickness of ergodic layer, λ_{erg} , increases with the shift of magnetic axis outwardly. It can be seen that the λ_{erg} at inboard side becomes very large for the outward shifted plasma configurations. Ergodicity is defined by the inverse of Kolmogorov length, L_k^{-1} . In LHD, the L_k^{-1} is an increasing function of major radius. When the ergodic layer becomes thicker, the L_k^{-1} becomes larger at the periphery of the ergodic layer. Then, the ergodicity in the thick ergodic layer is always large [31]. Outside of this ergodic layer, there exist four intrinsic divertor legs between the X-points and divertor plates. Particles flux came out of the plasma core finally reach the divertor plates though the ergodic layer and the divertor legs.

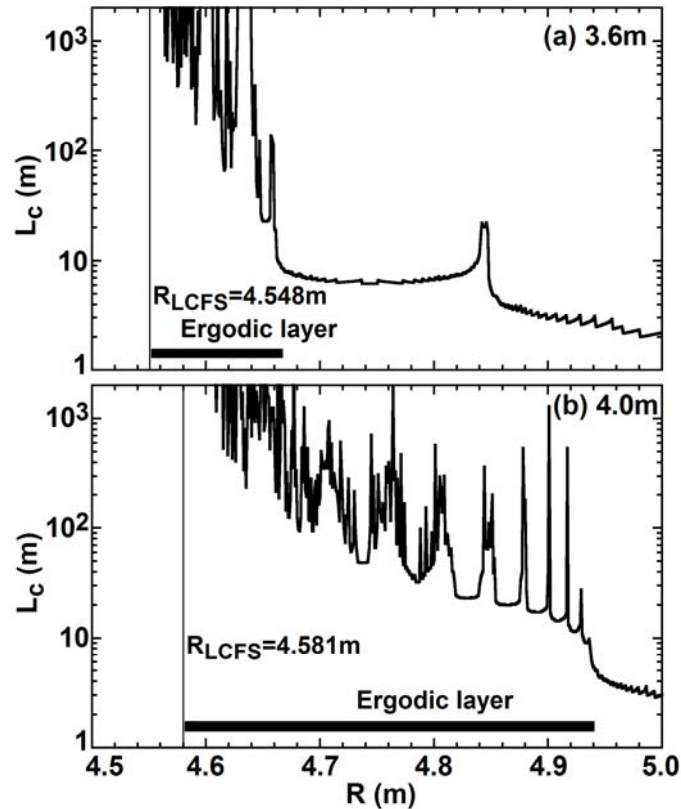


Fig. 4.11 Edge profiles of magnetic field connection length, L_c , as a function of major radius, R , at outboard side of horizontally elongated plasma cross section in (a) $R_{ax}=3.6$ and (b) 4.0m . Vertical solid lines indicate LCFS positions and horizontal thick bars denote range of ergodic layer.

Edge profiles of the magnetic field connection length, L_c , are illustrated in Figs.4.11 (a) and (b) at the horizontally elongated plasma cross sections for $R_{ax}=3.60$ and 4.00m , respectively. The LCFS position is shown by a solid vertical line and typical range of the ergodic layer is indicated by a thick horizontal bar. As one can see, the ergodic layer consists of field lines with short and long connection lengths. The long field lines work as the main channel of the particle and heat outfluxes. Number of the field lines with short connection length of $L_c \leq 100\text{m}$ increases towards the periphery of the ergodic layer, which is known as the edge surface layer. Long connection lengths also appear in the edge surface layer with narrow discrete region and coexist together with the short connection lengths. This structure is a unique feature of the LHD intrinsic divertor configuration. The short field lines provide particle and energy sinks for the long field lines via perpendicular transport.

4.2.3. Experimental setup

LHD discharge is generally initiated by electron cyclotron heating (ECH) and then sustained and heated by three negative-ion based neutral beam injection (NBI). Total heating power of NBI is 18MW in maximum. Typical operational range of LHD discharges with gas puff is in $n_e \leq 10^{20}\text{m}^{-3}$ and $T_e \leq 3\text{keV}$. Higher density operation up to 10^{21}m^{-3} is possible using H_2 pellet injection. Carbon emissions have been monitored using resonance transitions of CIII (977\AA , $2s2p\ ^1P-2s^2\ ^1S$), CIV (1548\AA , $2p\ ^2P-2s\ ^2S$), CV (40.27\AA , $1s2p\ ^1P-1s^2\ ^1S$) and CVI (33.73\AA , $2p\ ^2P-1s\ ^2S$). The CIII and CIV lines in VUV range are observed using two absolutely calibrated 20cm normal incidence vacuum ultraviolet (VUV) monochromators equipped with secondary electron multiplier (SEM) tube detectors [9]. The signal is usually acquired with time interval of $100\mu\text{s}$. Absolute intensity calibration is done using intensity ratio of $3p-2s$ transition to $2p-2s$ transition in addition to the branching ratio method when the carbon emissions are measured by an absolutely calibrated flat-field extreme ultraviolet (EUV) spectrometer (EUV_Long: $50-500\text{\AA}$ range) [8]. The spectral lines from CV and CVI are observed using another absolutely calibrated flat-field EUV spectrometer [7] (EUV_Short: $10-130\text{\AA}$ range) with

a spectral resolution of $\sim 0.10\text{\AA}$ at 40\AA . Back-illuminated VUV sensitive charge couple device (CCD) detectors are mounted with both spectrometers and operated in full binning mode. The CCD detectors are cooled down to -20°C using Peltier devices during normal operation. Data from the CCD are acquired in every 5 ms with good signal-to-noise ratio.

Vertical profiles of CIII (4650\AA), CIV (5810\AA) and CV (2271\AA) emissions have been observed using a visible spectrometer for the Z_{eff} profile measurement [32]. The system consists of a Czerny-Turner-type spectrometer with a visible CCD camera and 44 optical fibers vertical array. The 30cm focal length spectrometer equipped with a toroidal, a flat and two spherical mirrors and three gratings (110, 120, and 1200 grooves/mm) covers wavelengths range of $2000\text{--}9000\text{\AA}$. Combination of the optical fiber (core diameter: $100\mu\text{m}$) with the lens (focal length: 30mm) provides spatial resolution of 30mm at the plasma center. Electron temperature and density profiles are measured with Thomson scattering diagnostics. Line-integrated electron density is measured with FIR diagnostics. Ion saturation current measured by Langmuir probes embedded on divertor plates is used in the present study as edge divertor density.

4.2.4. Brief description on impurity transport in ergodic layer

Analysis of impurity transport in ergodic magnetic field layer of LHD having toroidally nonuniform magnetic structure should be done with three-dimensional treatment of magnetic fields, as mentioned in section 4.2.6. For a better understanding of the physical background on the edge impurity transport, here, we describe usually used formulation in a simple 1D model along parallel and perpendicular to the field lines.

In the fluid description, the impurity transport along the field lines is considered to be governed by the momentum equation;

$$\mathbf{m}_z \frac{\partial \mathbf{V}_{z\parallel}}{\partial t} = -\frac{1}{n_z} \frac{\partial T_i n_z}{\partial s} + \mathbf{m}_z \frac{V_{i\parallel} - V_{z\parallel}}{\tau_{zi}} + Z\mathbf{e}E_{\parallel} + 0.76Z^2 \frac{\partial T_e}{\partial s} + 2.6Z^2 \frac{\partial T_i}{\partial s}, \quad (4.4)$$

where the subscript of z and i denote the impurity ion with charge state of Z and the background ion, respectively. The parameter of s is the coordinate along the field line. The symbols of τ_{zi} , E_{\parallel} and V_{\parallel} denote the impurity-ion collision time, the parallel electric

field and the parallel flow velocity, respectively. It is assumed that the ion temperature of impurity, T_z , is equal to the one of background ion, T_i . The first term in the right hand side is the pressure gradient force (FPG) of impurity. The second and third terms are the force due to friction (FF) between impurity and background ions and the one due to parallel electric field (FE), respectively. The FF goes towards divertor (downstream) and the FE pushes the impurity ions along the electric field. The fourth and fifth terms on the right hand side are the forces due to electron (FeG) and ion (FiG) temperature gradients, respectively. The both of them drive the impurity ions towards the high temperature region (upstream). Among these terms, the FF and FiG become dominant in usual plasma parameters [33]. When typical parameters are considered to be $T_e=100\text{eV}$, $T_i=150\text{eV}$, $n_i=10^{19}\text{m}^{-3}$ and $L_c=50\text{m}$ for He-like CV (C^{+4}) ions, the values of the force terms mentioned above are given by

$$\begin{aligned} \mathbf{FF} &\sim \mathbf{m}_z \times 0.5\mathbf{c}_s / \tau_{\text{CV},i} = 1.3 \times 10^{-17}, \\ \mathbf{FE} &\sim z \times \mathbf{T}_e / L_c = 1.3 \times 10^{-18}, \\ \mathbf{FiG} &\sim 2.6Z^2 \times \mathbf{T}_i / L_c = 2.0 \times 10^{-17} \text{ and} \\ \mathbf{FeG} &\sim 0.71Z^2 \times \mathbf{T}_e / L_c = 3.0 \times 10^{-18} \text{ kg.m.s}^{-2}, \end{aligned}$$

where $\tau_{\text{CV},i} \sim 1.16 \times 10^{-4}\text{s}$. The relation of $\text{FF} > \text{FE}$ and $\text{FiG} > \text{FeG}$ is seen in the estimation. The term of FPG becomes very weak, since the parallel density gradient is relatively small. The force balance between FF and FIG, i.e., friction force and thermal force, thus defines the direction of impurity flow. The impurity velocity along field lines is expressed by

$$\mathbf{V}_{z\parallel} = \mathbf{V}_{i\parallel} + 2.6Z^2 \frac{\tau_{zi}}{\mathbf{m}_z} \frac{\partial \mathbf{T}_i}{\partial \mathbf{s}}. \quad (4.5)$$

The flow of $\mathbf{V}_{i\parallel}$ goes toward downstream and the gradient of $\partial \mathbf{T}_i / \partial \mathbf{s}$ defines the upstream flow. The impurity flow goes toward downstream, when the thermal force is dominated by the friction force. Here, the ratio of these two force terms [34] can be written as

$$\frac{\text{friction force}}{\text{thermal force}} \sim \frac{2.5n_i T_i V_{i\parallel}}{\kappa_i^0 T_i^{2.5} \nabla_{\parallel} T_i} \propto \frac{n_i |M|}{T_i \nabla_{\parallel} T_i}, \quad (4.6)$$

where M is the Mach number and κ_i^0 the parallel heat transport coefficient. The numerator and denominator represent convective and conductive energy fluxes, respectively.

In radial transport in the ergodic layer, on the other hand, the 1D radial continuity equation of impurity [34] is expressed as

$$\frac{\partial}{\partial r} \left(\Theta n_I V_{z\parallel} - D_I \frac{\partial n_I}{\partial r} \right) = 0, \quad (4.7)$$

since the source term can be neglected because of the short ionization mean free path of neutral impurity. Here, the symbol of r defines the radial direction of plasma and n_I means the impurity density summed over all charge states. The value of D_I expresses the cross field diffusion coefficient of impurity. The symbol of Θ denotes the field line pitch inside remnant islands in the ergodic layer, which is defined as dr/dl with dl being the parallel path along island separatrix for radial displacement of dr . The equation can be integrated and replaced by [35]

$$n_I(\mathbf{r}) = n_I(\mathbf{a}) \exp \left(- \int_r^a \frac{\Theta V_{z\parallel}}{D_I} dr \right), \quad (4.8)$$

where a is the outermost boundary of the ergodic layer. The equation indicates that the impurity is screened in the ergodic layer, if the outward impurity flow, $V_{z\parallel} > 0$, is appeared. In the following discussion it is assumed that the perpendicular transport coefficients do not change so much when the edge parameters such as the density and magnetic field structure are changed.

4.2.5. Experimental results and discussions

Fractional abundance of carbon ions at plasma center is calculated using 1-d transport code [1] assuming diffusion coefficient of $D=0.1\text{m}^2/\text{s}$, which is used to study the core transport properties of LHD plasma [4]. Figure 4.12 shows the fractional abundance as a function of T_e . Since the abundance of carbon ions located at plasma edge and are also a function of convection velocity, the radial position of each carbon ion should shift toward higher temperature range. However, the figure is still useful for

understanding the ionization balance of carbon. The Be-like (CIII) and Li-like (CIV) ions are located in a very low temperature region of $T_e < 15\text{eV}$. The He-like (CV) and H-like (CVI) ions, on the other hand, are located in a clearly separated temperature region from CIII and CIV, i.e., $10 < T_e < 200\text{eV}$. This is a very important thing in the present study. Since edge temperatures at LCFS ($\rho=1$) in LHD usually distribute in a range of $50 \leq T_e \leq 500\text{eV}$ except for extremely high-density range, the CIII and CIV always exist outside of the ergodic layer in LHD, whereas the CV and CVI exist near the LCFS (see typical edge T_e profiles, e.g., Fig.4.16).

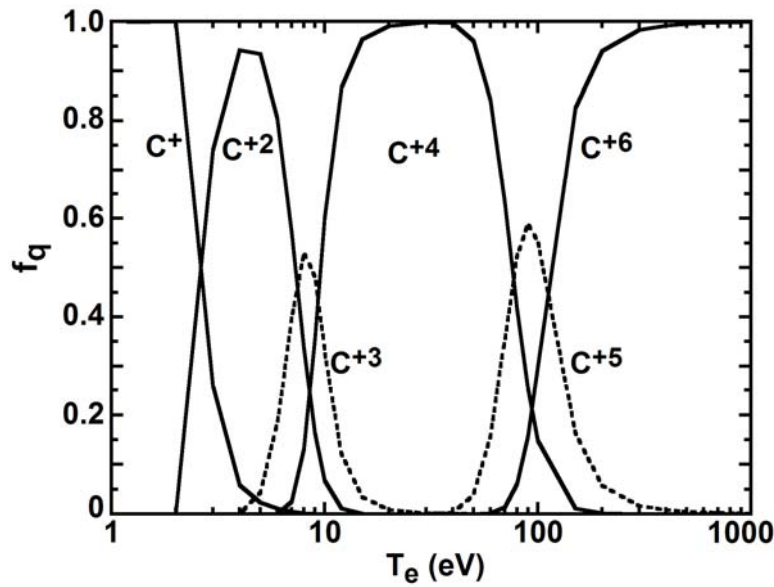


Fig. 4.12 Fractional abundance of C^+ , C^{+2} , C^{+3} , C^{+4} , C^{+5} and C^{+6} as a function of T_e .

The impurity radial profiles have been observed using a visible spectrometer for bremsstrahlung profile measurement. Typical examples of vertical profiles in CIII, CIV and CV emissions measured at $R_{ax}=3.6\text{m}$ are shown in Fig.4.13. The magnetic field configuration of $R_{ax}=3.6\text{m}$ is traced in Fig.4.14 for poloidal cross section along the view angle of the visible spectrometer. The CIII and CIV profiles in Fig.4.13 indicate a remarkable nonuniformity reflecting the field line structure of the ergodic layer. Both of the strong peaks at $Z=0.37\text{m}$ in CIII and at $Z=0.09\text{m}$ in CIV originate in the ergodic layer near inboard side X-point. Other peaks of CIII and CIV profiles seen in the same vertical location of $Z=0.46\text{m}$ indicate the usual edge emission of the elliptical plasma at the

horizontally elongated plasma cross section. This edge emission can be enhanced by the long chord length along the plasma edge at the top side as seen in Fig.4.14. In LHD the particle recycling becomes dominant at the inboard side in the $R_{ax}=3.6\text{m}$ configuration, whereas it becomes dominant at the outboard side in outwardly shifted plasma position such as $R_{ax}=3.9\text{m}$ [15]. The neutral hydrogen and helium emissions also show the inhomogeneous poloidal distribution, which arises mainly from the inhomogeneity in the neutral particle density [16]. This is the reason why such the nonuniform profiles are seen in the CIII and CIV. However, the CV profile does not have any strong asymmetric characteristic suggesting a function of the magnetic surface. Here, it should be mentioned that a few viewing chords at the bottom side near $Z=-0.4\text{m}$ are hid by a rid of the vacuum vessel. Its intensity gradually increases when the line-of-sight is moved from the bottom to the top side of elliptical plasma. This continuous intensity change mainly originates in the different chord integration length of the edge plasma.

Spectral emissions from CIII, CIV, CV and CVI have been analyzed during steady state phase of several NBI discharges in LHD. Since the ionization energies of CIII (48eV) and CIV (64eV) are very small compare to the CV (392eV) and CVI (490eV), there exists a clear separation among radial locations of carbon ions in such different four ionization stages, as mentioned before. The four charge states of carbon ions can be thus divided into two groups, i.e., CIII+CIV and CV+CVI. The CIII and CIV existing at outer side in the ergodic layer can be taken as the source term representing the influx of carbon, while the CV and CVI existing near the LCFS can be taken as the ions through the transport in the ergodic layer. Intensity ratio of the two groups, which can give a degree of the impurity screening, has been analyzed to study the edge impurity transport with different edge plasma parameters and ergodic magnetic field structures.

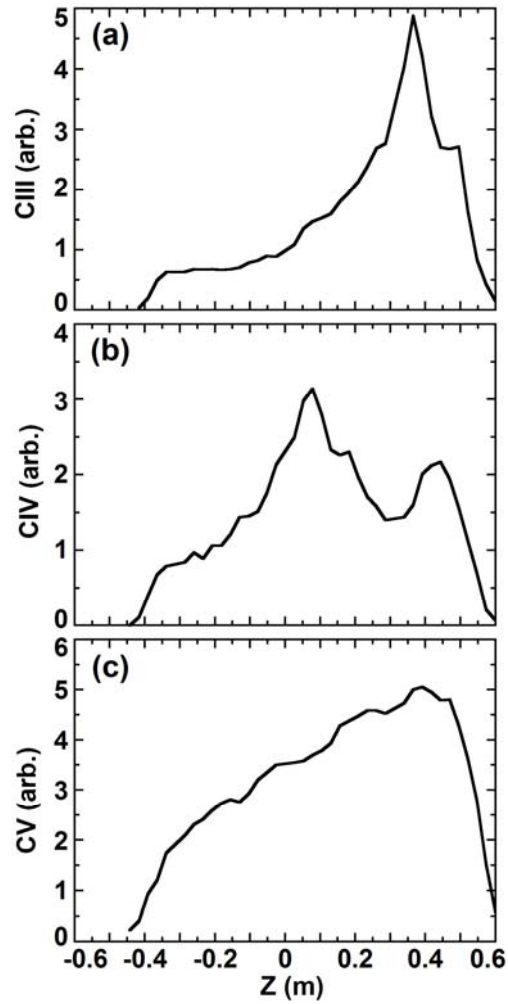


Fig. 4.13 Vertical profiles of (a) CIII (4647Å), (b) CIV (5810Å) and (c) CV (2271Å) at $R_{ax}=3.6m$ measured by visible spectrometer for bremsstrahlung profile measurement.

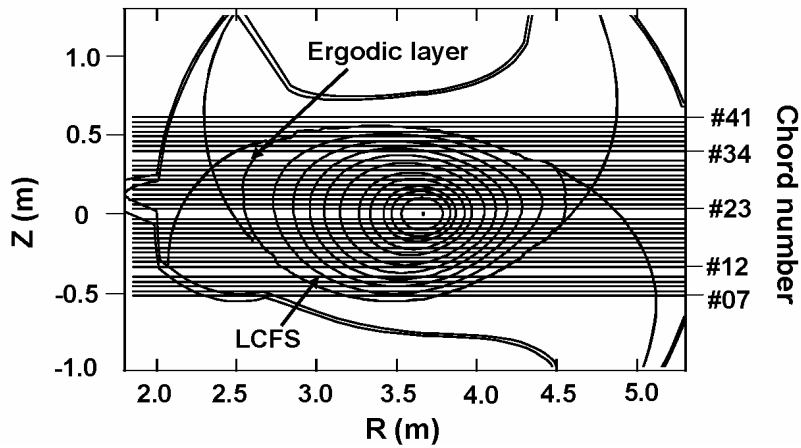


Fig. 4.14 View chords of visible spectrometer (horizontal lines) and magnetic field structure of LHD in $R_{ax}=3.6m$. Chord number of optical fibers is expressed as '#41'.

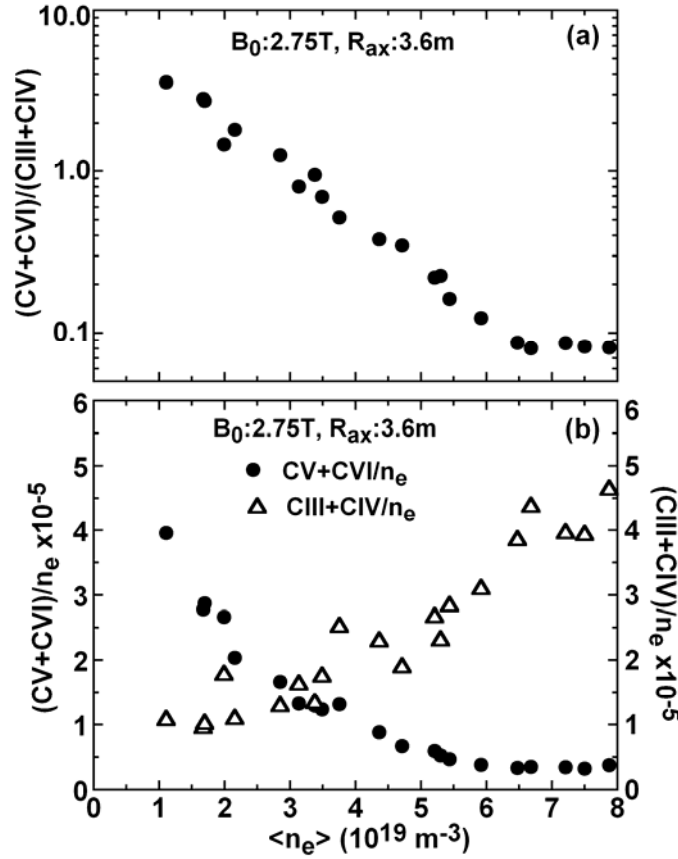


Fig. 4.15 (a) Ratio of CV+CVI to CIII+CIV and normalized intensities of (b) $(CV+CVI)/n_e$ (closed circles) and $(CIII+CIV)/n_e$ (open triangles) in unit of $10^{14} \text{ photons.cm}^{-2}.\text{sr}^{-1}.\text{s}^{-1} / 10^{19} \text{ m}^{-3}$ as a function of $\langle n_e \rangle$ for $R_{ax}=3.6\text{m}$.

4.2.5.1. Density dependence of carbon emissions

The ratio of the CV+CVI to CIII+CIV as a function of line-averaged electron density, $\langle n_e \rangle$, is plotted in Fig.4.15 (a). The ratios drop two orders in magnitude when the density rises from 1 to $8 \times 10^{19} \text{ m}^{-3}$. This drop is mainly due to that the CIII+CIV intensity monotonically increases with n_e whereas the CV+CVI intensity tends to decrease with increasing n_e . This is seen in the Fig.4.15 (b), where the CV+CVI and CIII+CIV intensities normalized by the density are plotted with $\langle n_e \rangle$. The edge n_e (circles) and T_e (triangles) profiles from two discharges with different $\langle n_e \rangle$ are plotted in Fig.4.16. Here, the closed and open symbols mean low- ($\langle n_e \rangle = 1.5 \times 10^{19} \text{ m}^{-3}$) and high-

density ($\langle n_e \rangle = 5.5 \times 10^{19} \text{ m}^{-3}$) discharges, respectively. It can be clearly seen that the edge T_e becomes lower at higher edge n_e . In ionizing plasma like the steady states phase of discharges, the CIII and CIV intensities normalized by the density reflect the influx of carbon since the excitation rate coefficients become independent on T_e . The edge T_e profile generally does not change so much in LHD when the density changes. Then, the emission profile itself of CV and CVI does not change although the radial location changes according to the change of edge T_e . In the edge n_e profiles a little jump is seen at $R=4.6\text{m}$. This edge density jump is seen in most of the discharges measured from Thomson scattering diagnostics. The reason is now unclear. As indicated in the Fig.4.15 (a) the drop of the intensity ratio thus suggests the impurity screening in higher n_e range.

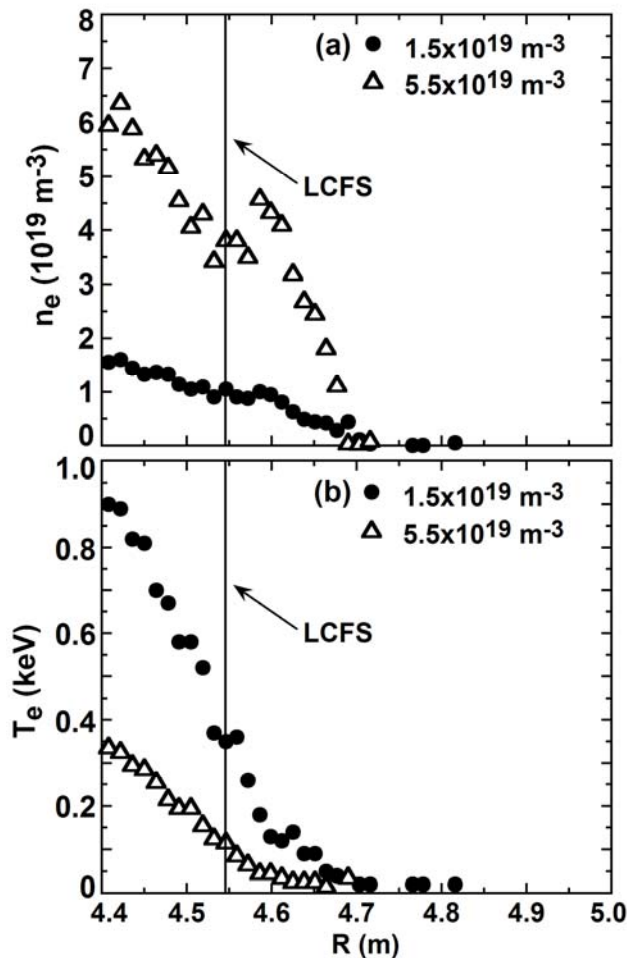


Fig. 4.16 (a) Edge n_e and (b) T_e profiles as a function of major radius for low-density (closed circles: $\langle n_e \rangle = 1.50 \times 10^{19} \text{ m}^{-3}$) and high-density (open triangles: $5.52 \times 10^{19} \text{ m}^{-3}$) discharges in $R_{ax} = 3.6\text{m}$.

The ion-impurity collision frequency, ν_{zi} , for He-like CV ion given by [33]

$$\nu_{zi} \equiv 1/\tau_s = \frac{(1 + m_i/m_z) z^2 n_i \ln \Lambda}{1.47 \times 10^{13} m_z T_i (T_i/m_i)^{0.5}} \quad (4.9)$$

Assuming $T_i=100\text{eV}$, the frequencies become 3.42×10^4 and $1.02 \times 10^5 \text{s}^{-1}$ at densities of $n_i=2 \times 10^{19}$ and $6 \times 10^{19} \text{m}^{-3}$, respectively. The increase of the collision frequency means the enhanced contribution of the friction at higher densities. The friction force begins to overcome the thermal force in higher n_e range as suggested in Eq.4.6 and leads to enhancement of the impurity screening. This argument is continued in next section 4.2.6 in more detailed with the edge transport simulation using EMC3+EIRENE code.

4.2.5.2. Carbon emissions with different magnetic axes

When the magnetic axis is shifted, the thickness of the ergodic layer remarkably changes. Figure 4.17 (a) illustrates the ratio of the CV+CVI to CIII+CIV emission as a function of $\langle n_e \rangle$. The ratios decrease with increasing $\langle n_e \rangle$ for all magnetic axis configurations. In addition, the ratios become lower with shifting R_{ax} outwardly. This tendency is very clear especially for densities of $\leq 5 \times 10^{19} \text{m}^{-3}$. This reduction is mainly caused by the decrease in the CV+CVI intensity, as shown in Fig.4.17 (b). On the contrary, the CIII+CIV intensities are not changed with $\langle n_e \rangle$ for all configurations, as revealed in Fig.4.17 (c), although the edge T_e and n_e are considerably changed by the R_{ax} shift. This indicates that the carbon source term is nearly similar in all magnetic axes except for 3.60m, where the source term is somewhat different at the low densities. Then, the reduction of the CV+CVI suggests enhancement of the impurity screening with increasing R_{ax} position. The structures of the ergodic layer are shown in Fig.4.18 for each R_{ax} position. The thickness of the ergodic layer increases with shifting the magnetic axis outwardly. This size of the ergodic layer plays an important role to the edge particle transport. Exact determination of the ergodic layer size is difficult at present because magnetic field lines continuously expand into outer area with a limited connection length. However, it is known from the experiments that the edge density is formed with connection lengths of $L_c > 10\text{m}$. Then, the area of the ergodic layer can be practically

determined from the experimental result, as indicated with horizontal bar in Fig.4.18. The thickness of the ergodic layer is plotted in Fig.4.19 as a function of R_{ax} position. The thinnest ergodic layer can be obtained in $R_{ax}=3.6m$ configuration with the maximum volume in LHD plasmas of $30m^3$, which is called 'standard configuration'. The ergodic layer thickness becomes 3–5 times larger in $R_{ax}=4.0$ and $4.1m$ cases with reducing the plasma volume contrastively.

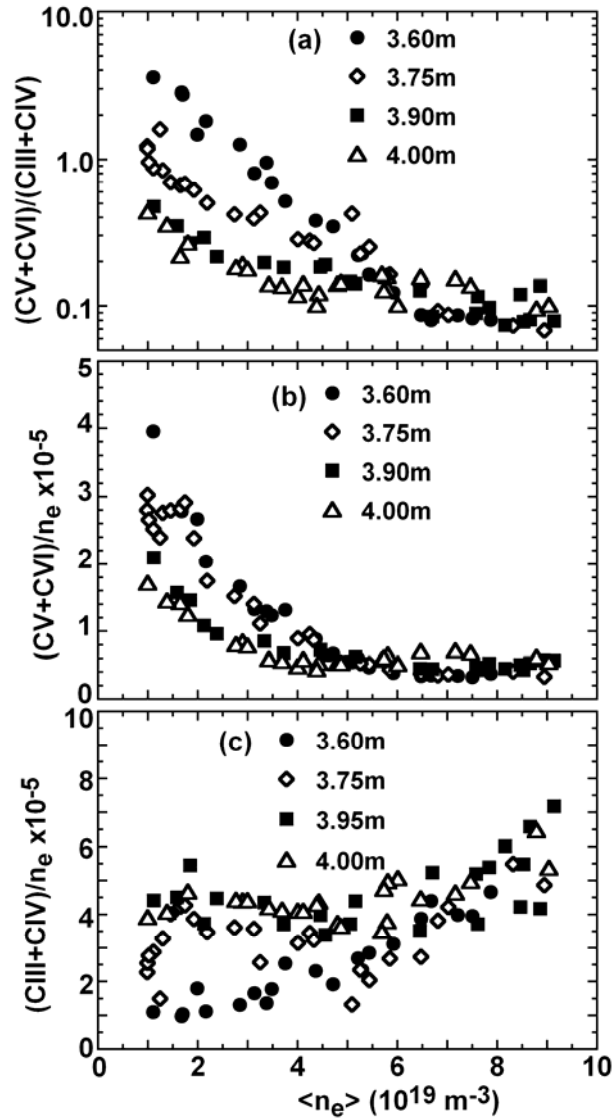


Fig. 4.17 (a) Ratio of CV+CVI to CIII+CIV and normalized intensities of (b) $(CV+CVI)/n_e$ and (c) $(CIII+CIV)/n_e$ in unit of $10^{14} \text{ photons.cm}^{-2}.\text{sr}^{-1}.\text{s}^{-1}/10^{19} m^{-3}$ as a function of $\langle n_e \rangle$ in $R_{ax}=3.60$ (closed circles), 3.75 (open diamonds), 3.90 (closed squares) and 4.00m (open triangles).

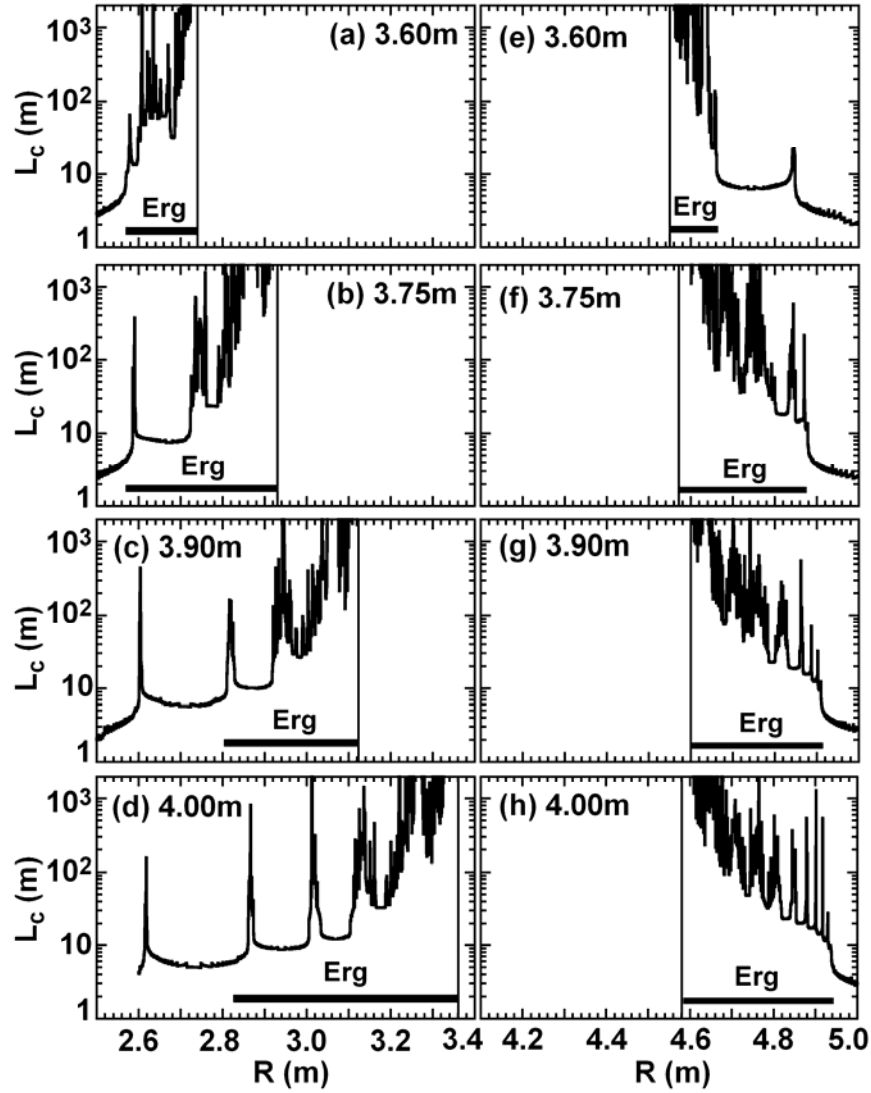


Fig. 4.18 Edge profiles of magnetic field connection length, L_c , plotted as a function of major radius, R , at inboard (a)-(d) and outboard (e)-(f) sides for horizontally elongated plasma cross section in $R_{ax}=3.60$, 3.75 , 3.90 and 4.00 m, respectively. Vertical solid lines indicate LCFS positions and horizontal thick bars denoted with 'Erg' show the range of ergodic layer.

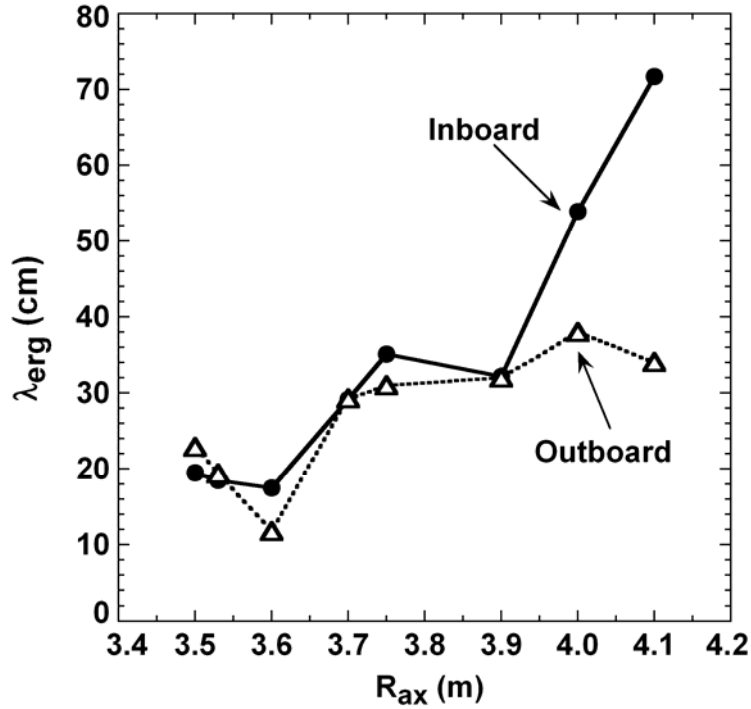


Fig. 4.19 Ergodic layer thickness, λ_{erg} , as function of magnetic axis, R_{ax} , at inboard (closed circles) and outboard (open triangles) sides in horizontally elongated plasma cross section

Figure 4.20 shows the edge profiles of n_e and T_e for $R_{ax}=3.60$ and 4.00 m positions. The edge density tends to have flatter profile with increasing R_{ax} position under the same line-averaged electron density. This tendency is clearly seen in Fig.4.20 (a). Thicker ergodic layer of $R_{ax}=4.00$ m maintains a flatter density profile with high density compared to $R_{ax}=3.60$ m case. The edge T_e profiles in the ergodic layer are almost similar in both cases as plotted in Fig.4.20 (b), while the core T_e profiles inside the LCFS are quite different. The edge density in the ergodic layer normalized to the core density becomes higher with increasing ergodic layer thickness. As a result, one can see that the friction force dominates over the ion thermal force in the thick ergodic layer and the degree of the impurity screening is a function of the size of the ergodic layer.

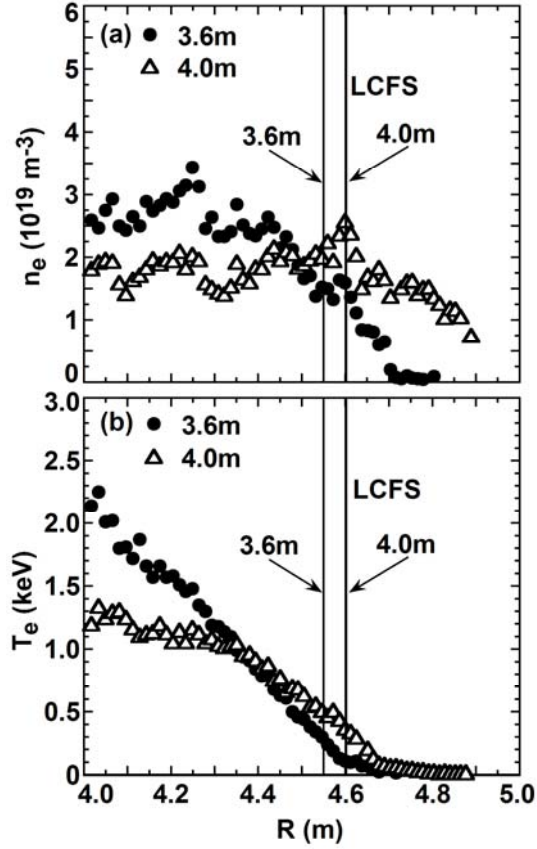


Fig. 4.20 (a) Edge n_e and (b) T_e profiles as a function of major radius for $R_{ax}=3.60$ (closed circles) and 4.00m (open triangles). Vertical lines indicate LCFS positions for $R_{ax}=3.60$ and 4.00m .

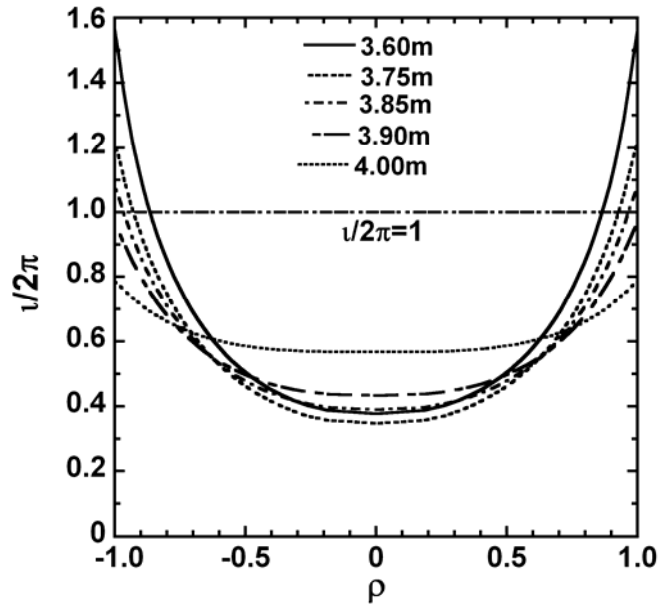


Fig. 4.21 Radial profiles of rotational transform, $v/2\pi$, in $R_{ax}=3.60$ (—), 3.75 (---), 3.85 (- · - ·), 3.90 (- - -) and 4.00m (·····). Value of ρ means normalized radius.

4.2.5.3. Carbon emissions with externally supplied $m/n=1/1$ magnetic island

In LHD, the $m/n=1/1$ magnetic island can be superimposed in the edge region by using LID coils, where m and n are the poloidal and toroidal mode numbers, respectively. The position of island varies with magnetic axis since the rotational transform appreciably changes with R_{ax} . Figure 4.21 shows the profiles of the rotational transform as a function of normalized radius of ρ . The rotational transform profiles become gradually flatter with R_{ax} . As a result, the radial location of $\iota/2\pi=1$ surface moves to the outside region of the plasma when the R_{ax} is shifted outwardly. The position of $\iota/2\pi=1$ is located at $\rho=0.83$ in $R_{ax}=3.60\text{m}$, whereas it is inside the ergodic layer for $R_{ax}=4.00\text{m}$. Then, the radial position of the $m/n=1/1$ island can be located just inside the LCFS for $R_{ax}=3.75\text{m}$ and just outside the LCFS (inside the ergodic layer) for $R_{ax}=3.85\text{m}$. The LID coils were supplied to expand the $m/n=1/1$ island for both cases. The edge magnetic field structures are calculated and the Poincare plots are shown in Fig.4.22 at horizontally elongated plasma cross section. Vertical solid lines indicate LCFS position. The size of intrinsic $m/n=1/1$ island is basically very small (see Fig.4.22 (a)). When the LID coils are supplied, the formation of large island is clearly visible at outboard side of the elliptical plasma. On the contrary, the formation of the island is not visible at least in Fig.4.22 (d) because no resonant field essentially exists in the ergodic layer. A certain effect given by the supplied LID coils, however, can be seen in the figure. It is then expected to modify the edge impurity transport using $m/n=1/1$ magnetic island.

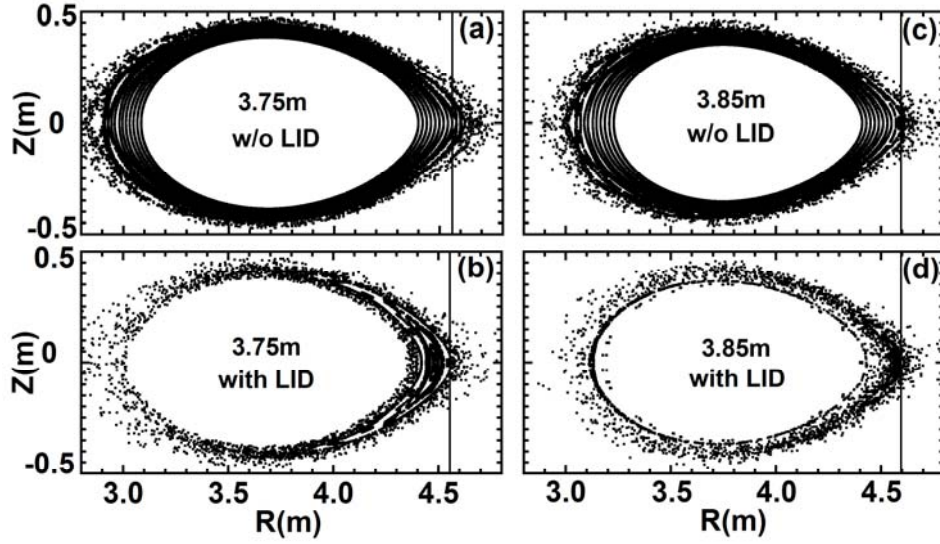


Fig. 4.22 Magnetic field structures of edge ergodic layer at horizontally elongated plasma cross sections in (a) $R_{ax}=3.75\text{m}$ without LID, (b) $R_{ax}=3.75\text{m}$ with LID, (c) $R_{ax}=3.85\text{m}$ without LID and $R_{ax}=3.85\text{m}$ with ILD. Large $m/n=1/1$ island is externally produced by ten sets of LID coils. Vertical solid lines indicate LCFS positions.

The line emissions from carbon are observed in the absence and presence of the superimposed island for $R_{ax}=3.75$ and 3.85m as mentioned above. The ratios of CV+CVI to CIII+CIV are plotted with their intensities as a function of $\langle n_e \rangle$ in Fig.4.23. In the $R_{ax}=3.75\text{m}$ configuration the ratios do not entirely change between the cases with and without $m/n=1/1$ island. However, the ratios measured in $R_{ax}=3.85\text{m}$ configuration drastically decrease when the magnetic field structure in the ergodic layer is changed by the LID coils current, as seen in Fig.4.23 (d). This reduction of the ratios originates in the simultaneous changes of CV+CVI decrease and CIII+CIV increase (see Figs.4.23 (e) and (f)).

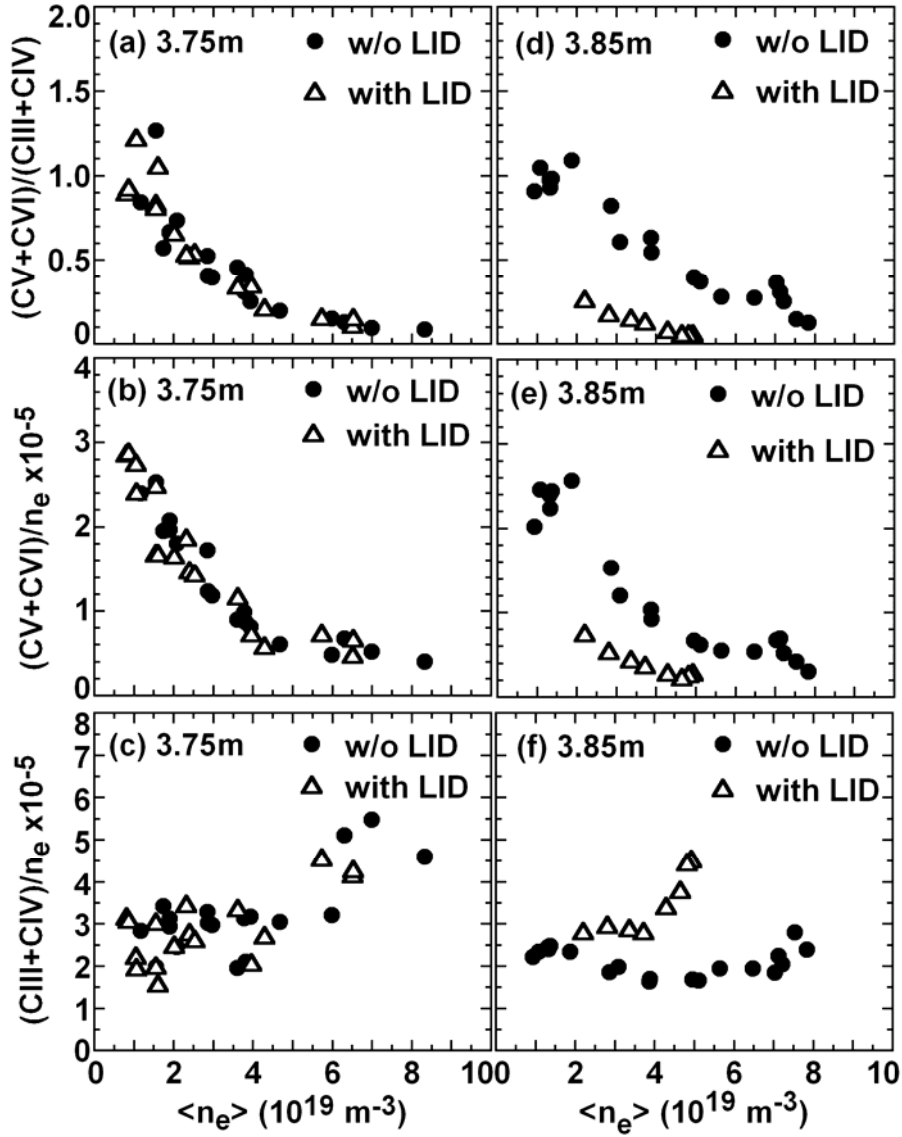


Fig.4.23 (a) Ratio of CV+CVI to CIII+CIV and normalized intensities of (b) $(CV+CVI)/n_e$ and (c) $(CIII+CIV)/n_e$ as a function of $\langle n_e \rangle$ for $R_{ax}=3.75\text{m}$ and (d) ratio of CV+CVI to CIII+CIV, intensities of (e) $(CV+CVI)/n_e$ and (f) $(CIII+CIV)/n_e$ as a function of $\langle n_e \rangle$ for $R=3.85\text{m}$ without (closed circles) and with (open triangles) LID coils current. Unit of $(CV+CVI)/n_e$ and $(CIII+CIV)/n_e$ is in $10^{14}\text{ photons.cm}^{-2}\text{.sr}^{-1}\text{.s}^{-1}/10^{19}\text{m}^{-3}$.

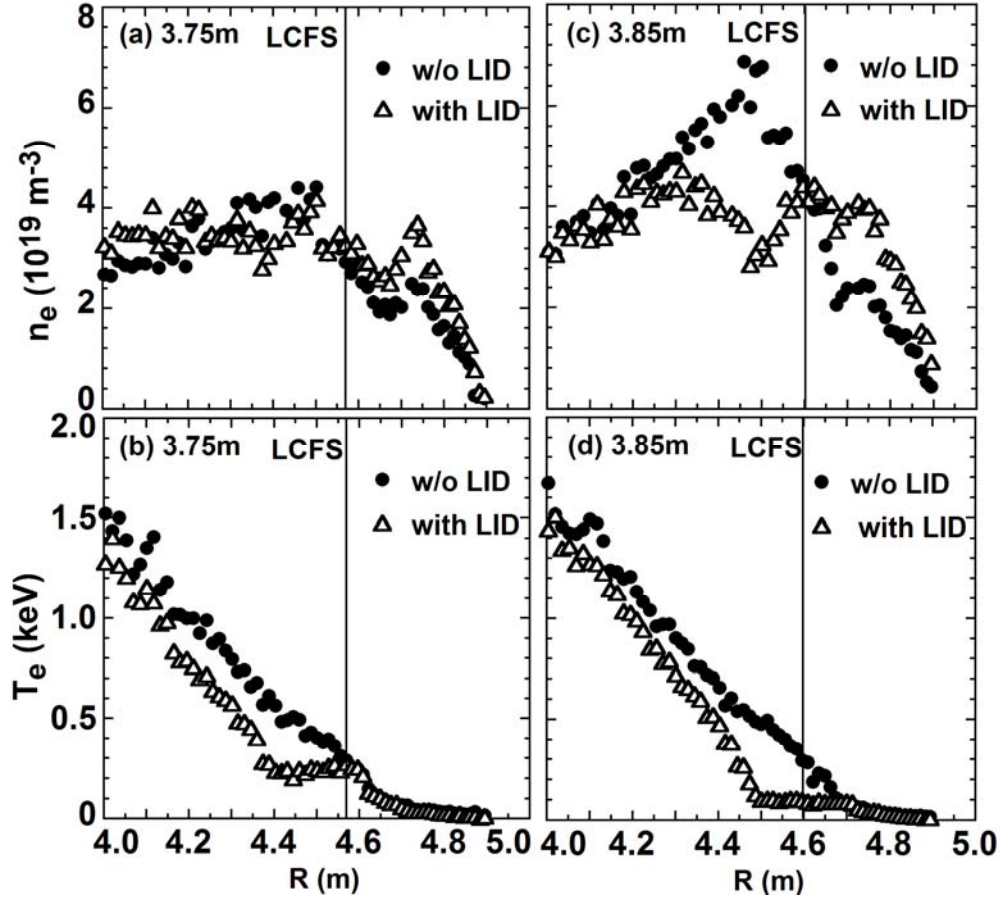


Fig. 4.24 Edge n_e and T_e profiles as a function of major radius with (open triangles) and without (closed circles) LID; (a) n_e at $R_{ax}=3.75$, (b) T_e at $R_{ax}=3.75$, (c) n_e at $R_{ax}=3.85$ m and (d) T_e at $R_{ax}=3.85$ m. Solid vertical lines indicate LCFS positions.

Edge n_e and T_e profiles are shown in Fig.4.24 for $R_{ax}=3.75$ and 3.85 m. When the LID coils are turned on in $R_{ax}=3.75$ m configuration, the T_e profile in the ergodic layer does not change, whereas the T_e profile inside the LCFS changes very much with appearance of flat T_e profile due to the $m/n=1/1$ island formation (see Fig.4.24 (b)). In case of the $R_{ax}=3.85$ m the flat T_e profile expands inside the ergodic layer, as shown in Fig.4.24 (d). The density in the ergodic layer increases a little when the island is produced (see Fig.4.24 (c)). Here, the discharges were tried to achieve the same line-averaged electron density in both cases of $R_{ax}=3.85$ m. However, higher gas puffing rate was required in case of the island formation. This may be the reason why the ergodic layer density is a little high. The size of the island in $R_{ax}=3.75$ and 3.85 m configurations

was ~ 17 and ~ 22 cm with $T_e \sim 250$ and ~ 90 eV, respectively. Through this island experiment one can understand that the modification of magnetic field lines in the ergodic layer clearly changes the edge impurity transport. The physical understanding is, however, not enough at present. A help of the edge transport simulation will be necessary in understanding the parallel and perpendicular transports in the ergodic layer with large island.

4.2.5.4. Carbon emissions with H₂ and He discharges

The carbon impurity behavior has been studied with the change of background ion species. For the purpose, He discharges were produced instead of H₂ at magnetic axis of 3.85 m. The ratios of CV+CVI to CIII+CIV are plotted with $\langle n_e \rangle$ in Fig.4.25. The ratios shown in Fig.4.25 (a) are appreciably reduced by the He discharges, especially in densities of $\leq 5 \times 10^{19} \text{ m}^{-3}$. This reduction is mainly originated in the decrease of CV+CVI intensities as seen in Fig.4.25 (b). The CIII+CIV intensities become nearly the same in both cases in densities of $\leq 5 \times 10^{19} \text{ m}^{-3}$ except for a sudden rise in densities of $\geq 5 \times 10^{19} \text{ m}^{-3}$ (see Fig.4.25 (c)).

Waveforms of plasma stored energy and line-averaged density are traced in Fig.4.26 with carbon emissions. The global parameters of W_p and $\langle n_e \rangle$ are nearly the same except for the edge parameters including the carbon emissions. The edge T_e are plotted at $\rho=1$ as a function of $\langle n_e \rangle$ in Fig.4.27 (a). Any important difference is not seen in the figure between the H₂ and He discharges, while the edge T_e in He discharges are a little higher. A clear difference can be seen in the ion flux measured by Langmuir probe embedded on divertor plates, as shown in Fig.4.27 (b). The ion flux suddenly increases in densities of $\geq 5 \times 10^{19} \text{ m}^{-3}$ in H₂ discharges suggesting the enhanced carbon influx. The increase in the carbon influx at higher densities seen in Fig.4.25 (c) is reasonable, although the reason is quite unclear.

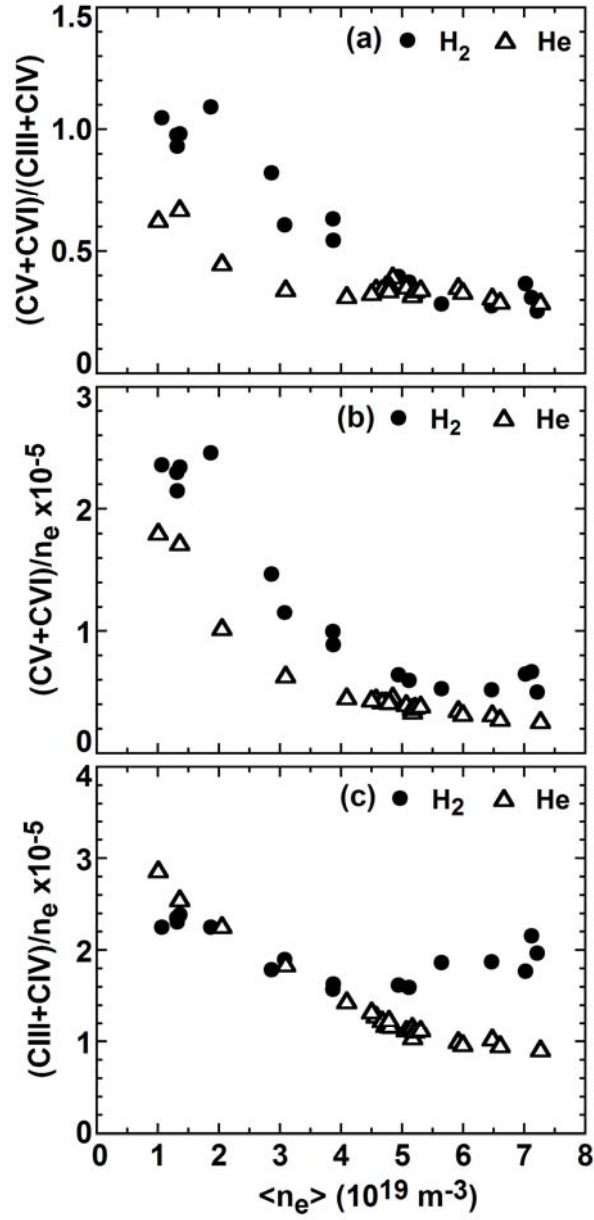


Fig. 4.25 (a) Ratio of CV+CVI to CIII+CIV and normalized intensities of (b) $(CV+CVI)/n_e$ and (c) $(CIII+CIV)/n_e$ in unit of 10^{14} photons.cm⁻².sr⁻¹.s⁻¹/10¹⁹m⁻³ as a function of $\langle n_e \rangle$ for H₂ (closed circles) and He (open triangles) discharges.

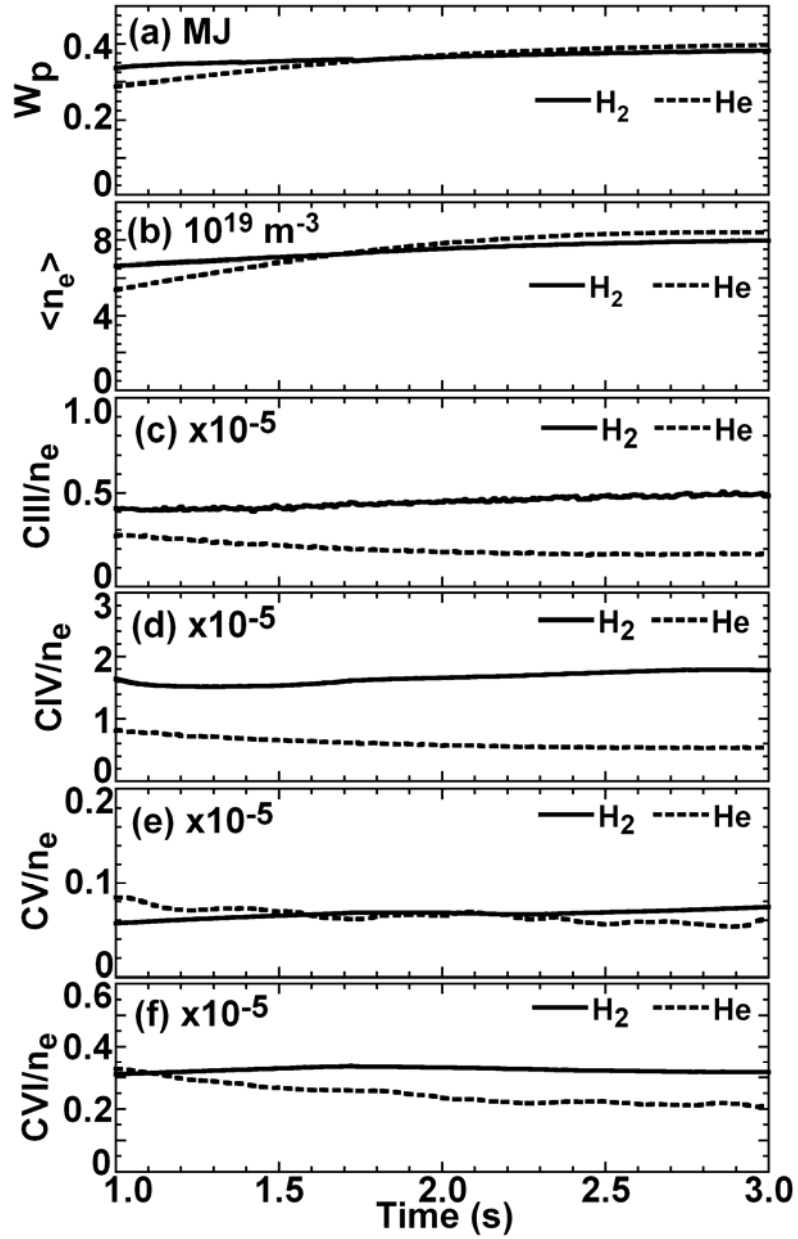


Fig. 4.26 (a) Plasma stored energy, W_p , (b) line-averaged density, $\langle n_e \rangle$ and normalized intensities of (c) $CIII/n_e$, (d) CIV/n_e , (e) CV/n_e and (f) CVI/n_e in H_2 (solid lines) and He (dashed lines) discharges. Unit of all carbon emissions of CIII (977Å), CIV (1548Å), CV (40.27Å) and CVI (33.73Å) is in $10^{14} \text{ photons.cm}^{-2}.\text{sr}^{-1}.\text{s}^{-1}/10^{19}\text{m}^{-3}$.

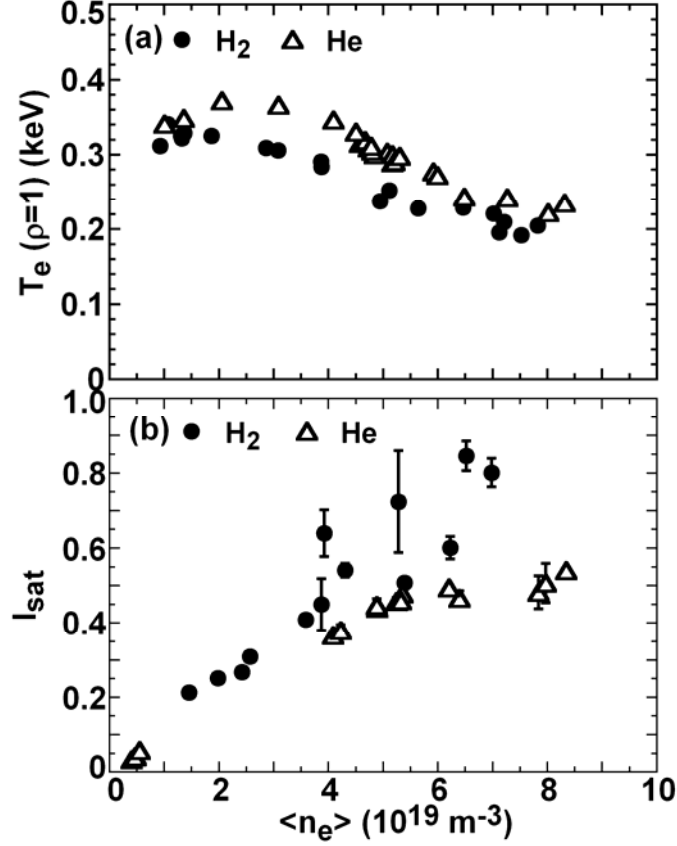


Fig. 4.27 (a) T_e at $\rho=1$ and (b) divertor ion saturation current, I_{sat} , as a function of $\langle n_e \rangle$ for H₂ (closed circles) and He (open triangles) discharges.

The reduction of the ratio $((\text{CV}+\text{CVI})/(\text{CIII}+\text{CIV}))$ in He discharges seems to be related to the change in the force balance parallel to magnetic fields. Assuming $T_i=100\text{eV}$ and $n_i=10^{19}\text{m}^{-3}$, the ion-impurity collision frequencies for He-like CV ion become 1.58×10^4 and $3.88 \times 10^4 \text{ s}^{-1}$ with H₂ and He background ions, respectively. This leads to the increased friction force. In He plasmas, furthermore, the constant part of $2.6Z^2$ for the ion thermal force term given by Eq.4.4 has to be replaced by $1.6Z^2$. This leads to the reduced contribution of the ion thermal force [33]. The increased friction force and reduced ion thermal force in He plasmas can enhance the impurity screening effect in the ergodic layer.

4.2.6. Comparison with simulated carbon emission using edge transport code

Impurity transport characteristics in the ergodic layer are analyzed using three dimensional edge transport code, EMC3+EIRENE. The simulation code of EMC3 [36] solves the fluid equations of mass, momentum and energy in arbitrarily magnetic field geometry using Monte Carlo scheme. The simulation code of EIRENE [37] solves a kinetic transport model of neutrals such as the recycling neutral from divertor plates as well as the interaction with bulk plasmas. The computational domain of the combined code starts from the LCFS at upstream, which covers entire ergodic layer and includes the realistic three dimensional nature of the magnetic field line structure [38].

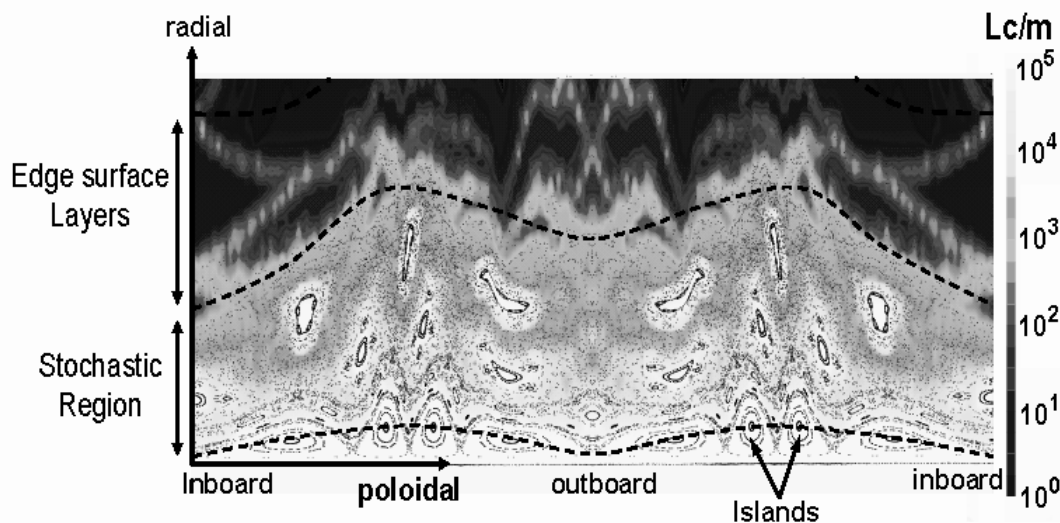


Fig.4.28. 2-dimensional profile of connection length, L_c , in ergodic layer of LHD ($R_{ax}=3.75m$) superposed with Poincare plot of magnetic field lines.

The profile of connection length, L_c , in ergodic layer of LHD superposed with Poincare plot of field lines is illustrated in Fig.4.28 with clearly separated two regions of 'stochastic region' and 'edge surface region'. The values of L_c in range of $1-10^5$ m are plotted in the figure. The magnetic islands are visible in the stochastic region. Moving further outwards, short and long field lines are mixed together. This region known as the edge surface layer is characterized by strong magnetic shear which stretches and bends

the flux tubes and thus mixes up the long and short flux tubes. The density and energy fluxes at the LCFS obtained from the experiment are used as the boundary conditions for particle and energy transports with input power to SOL of 8MW, while the Bohm condition is imposed at the divertor plates. Perpendicular transport coefficients for particle, D , and heat, χ , are taken to be 0.5 and $1.5\text{m}^2\cdot\text{s}^{-1}$, respectively. The perpendicular transport coefficient of impurity is considered to be the same as the background ions. The obtained impurity density profiles are averaged over poloidal and toroidal directions in order to plot as a function of radial coordinate, r_{eff} , which is defined by cylindrical approximation of the volume enclosed by each radial surface of the computational mesh. Radial profiles of the total carbon density are plotted in Fig.4.29 for different plasma densities. At the low density of $n_{\text{LCFS}}=2\times 10^{19}\text{m}^{-3}$ the carbon impurity is accumulated towards LCFS because of the effective ion thermal force. The impurity density in the stochastic layer gradually decreases with increasing densities and the impurity changes its direction towards the divertor plates due to the increase in the friction force at $n_{\text{LCFS}}=4\times 10^{19}\text{m}^{-3}$.

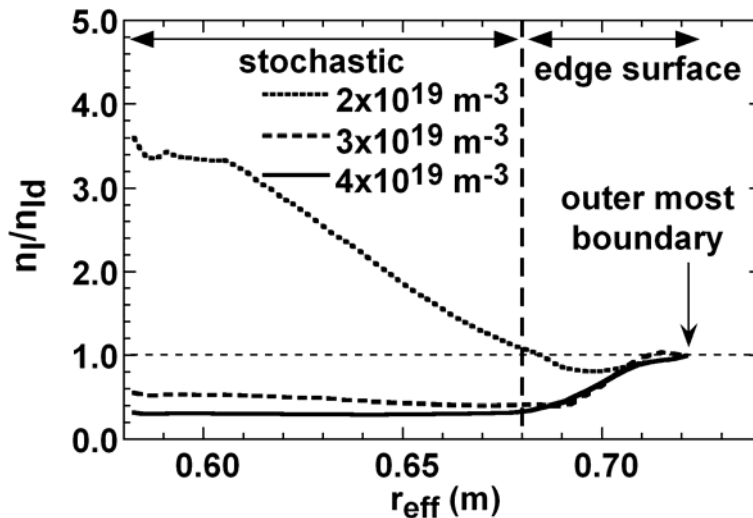


Fig. 4.29 Edge profiles of carbon density summed up over all charge states for different densities; (a) $n_{\text{LCFS}}=2\times 10^{19}\text{m}^{-3}$ (dotted line), $3\times 10^{19}\text{m}^{-3}$ (dashed line) and $4\times 10^{19}\text{m}^{-3}$ (solid line). Carbon density is normalized at outer most boundary of ergodic layer. Horizontal axis of r_{eff} means minor radius defined by cylindrical approximation. Vertical dashed line indicates the boundary between stochastic region and edge surface layers as shown in Fig.19.

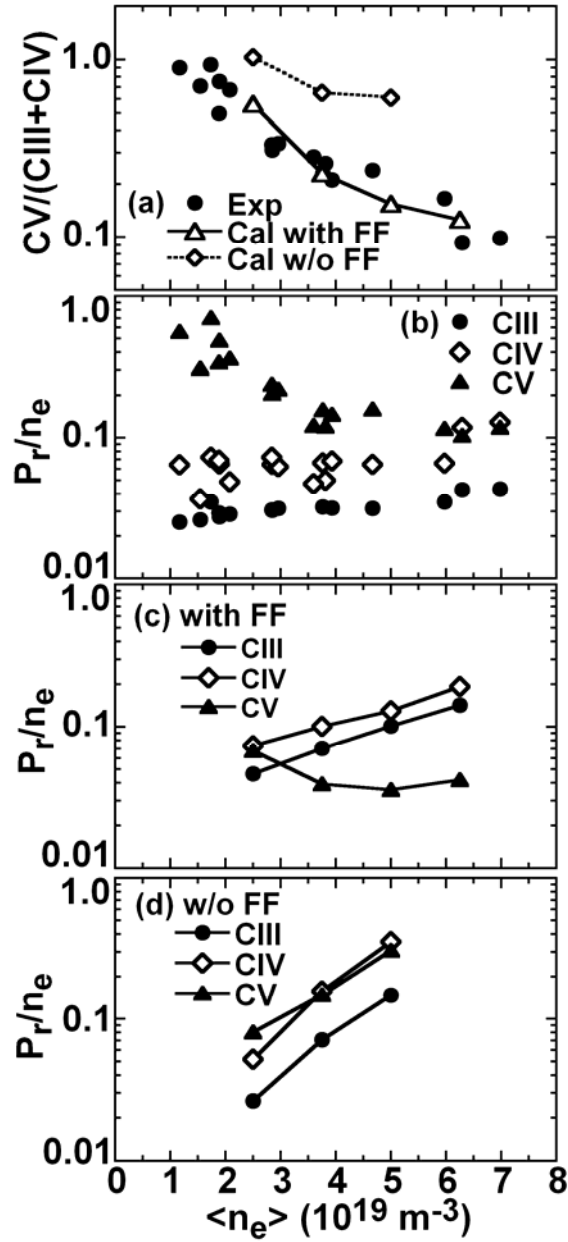


Fig. 4.30 (a) Ratios of CV to CIII+CIV from experiment (closed circles) and simulation with (open triangles+solid line) and without (open diamonds+dotted line) friction force as a function of $\langle n_e \rangle$ and normalized line radiations of CIII/ n_e (closed circles), CIV/ n_e (open diamonds) and CV/ n_e (closed triangles) from (b) experiment and simulations (c) with and (d) without friction force in unit of $\text{kW}/10^{19} \text{ m}^{-3}$ as a function of $\langle n_e \rangle$. Ratios from simulation are normalized to experimental value at $3.7 \times 10^{19} \text{ m}^{-3}$.

In the present computational domain the calculation is difficult inside the LCFS. However, the substantial fraction of CVI is often located inside the LCFS. Ratios of CV to CIII+CIV are then compared with simulated ones as shown in Fig.4.30 (a) instead of the ratio of CV+CVI to CIII+CIV. Data from the magnetic axis of 3.75m is considered here for the comparison. In the intensity calculation of the carbon emissions, the specific observation volume determined by each spectrometer is taking into account with its observation angle and line-of-sight.

The experimental line radiations are plotted in Fig.4.30 (b) as a function of line-averaged density. The CIII and CIV increase with n_e , whereas the CV decreases with n_e . The result from the simulation is shown in Fig.4.30 (c). The tendency of the emissions is very similar to the experimental ones. However, the absolute line radiation of CV is clearly different each other, i.e., the experimental CV radiation is 4 times larger than the calculated one. The reason is not clearly identified at present. There exist several assumptions in the simulation code due to the complexity of the magnetic field structure in the ergodic layer of LHD in addition to no access into the LCFS of the simulation code. Although the magnetic field structure in vacuum is used for the ergodic layer, the deformation based on the plasma pressure is entirely unknown at present. A little improvement seems to be necessary also in the absolute calibration of the spectrometers. Therefore, the calculated intensity ratios are normalized to the experimental ratio. The result is shown in Fig.4.30 (a). Data are normalized at $3.75 \times 10^{19} \text{ m}^{-3}$. The n_e dependence of the ratios qualitatively agrees well between the experiment and simulation. The simulation is also done in case of the absence of friction force. A clear difference is seen in the behavior of CV as shown in Fig.4.30 (d). The CV emission monotonically increases with n_e as well as the CIII and CIV when the friction force is disappeared in the ergodic layer. As a result, the ratio of CV to CIII+CIV does not decrease against the n_e as seen also in Fig.4.30 (a). The role of friction force becomes apparent by switching off the friction force term during the simulation.

The carbon density profiles simulated for each charge state are plotted in Fig.4.31 for two densities of n_{LCFS} . At high density of $n_{\text{LCFS}}=4 \times 10^{19} \text{ m}^{-3}$, the densities of C^{+4} (CV) and C^{+5} (CVI) become smaller while the ones of C^{+2} (CIII) and C^{+3} (CIV) increase

compared with the low-density case. Radial locations of the charge states are not basically changed by the difference of density. When the density increases, the friction dominant region gradually extends to inner radial space, which was originally dominated by the ion thermal force. The locations of C^{+2} and C^{+3} are then further limited to the edge surface layer. The negative gradient at $r_{\text{eff}} > 0.68\text{m}$ seen in the total carbon density of Fig.4.31 (b) is a clear indication for the outward impurity flow and resultant impurity screening.

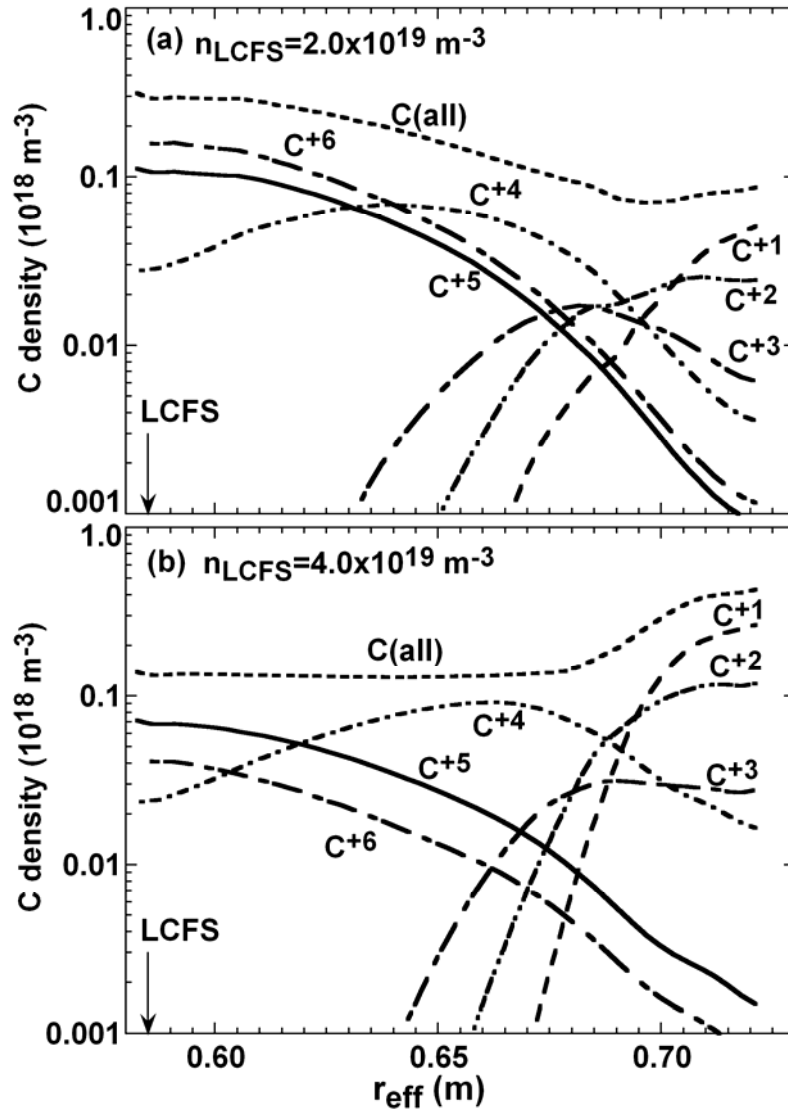


Fig. 4.31 Radial carbon density profiles of each charge state simulated by EMC3-EIRENE code with (a) $n_{\text{LCFS}}=2 \times 10^{19}$ and (b) $4 \times 10^{19} \text{m}^{-3}$. Solid vertical arrows indicate LCFS positions at $R_{\text{ax}}=3.75\text{m}$.

4.2.7. Summary

Carbon emissions have been studied to understand the impurity behavior in the edge ergodic layer of LHD. The study is carried out by taking the ratio of CV+CVI to CIII+CIV as a typical indicator of impurity screening. The results are discussed in relation to the impurity transport parallel to the magnetic field lines in the ergodic layer, which is mainly dominated by the ion thermal force and the friction force.

The ratio of CV+CVI to CIII+CIV decreases in two orders of magnitude with increasing n_e in a range of $1-8 \times 10^{19} \text{m}^{-3}$. This result indicates enhanced impurity screening in the ergodic layer at higher densities suggesting the importance of the friction force. The ratio is also examined by changing the thickness of the ergodic layer. The ratio decreases with ergodic layer thickness. The effect of the impurity screening can be enhanced in thicker ergodic layer. The carbon emissions are observed by changing the radial position of externally supplied $m/n=1/1$ island. The ratio clearly decreases when the island is located in the ergodic layer. This result evidently indicates that the modification of magnetic field structure in the ergodic layer gives a significant influence to the impurity behavior, although the reason is a little unclear now because of the uncertainty in the perpendicular transport. The ratio can be considerably reduced when the H_2 discharge is replaced by He discharge. The reduction of the ratio might be brought by the enhanced friction force due to increased collision with heavier background ions and decreased ion thermal force.

The simulation of impurity transport in the ergodic layer has been done to analyze the experimental data using EMC3+EIRENE code. The result strongly suggests the importance of the friction force in higher density ranges, which means the appearance of the impurity screening. The density dependence of the simulated ratio of CV to CIII+CIV is in a good agreement with the experimental result. Further effort is now being done to simulate the impurity behavior in the ergodic layer with $m/n=1/1$ large island. The atomic number dependence of the impurity screening effect is the future study in both sides of experiment and simulation.

References

- [1] T. Amano, J. Mizuno, and T. Kako, Int. Rep. IIPJ-616, Institute for Plasma Physics, Nagoya University (1982).
- [2] J. C. Moreno, and E. S. Marmor, Phys. Rev. A **31**, 3291 (1985).
- [3] H. Chen et al., Plasma Phys. Control. Fusion **43**, 1 (2001).
- [4] H. Nozato, S. Morita, M. Goto et al., Phys. Plasmas **11**, 1920 (2004).
- [5] R. Burhenn et al., Fusion Sci. Tech. **46**, 115 (2004).
- [6] Ph Ghendrih et al., Plasma Phys. Control. Fusion. **38**, 1653 (1996).
- [7] M. B. Chowdhuri, S. Morita, and M. Goto, Appl. Opt. **47**, 135 (2008).
- [8] M. B. Chowdhuri, S. Morita, M. Goto et al., Rev. Sci. Instrum. **78**, 023501 (2007).
- [9] S. Morita, M. Goto et al., Physica Script **T91**, 48 (2001).
- [10] S. Morita, M. Goto et al., Plasma Sci. Tech. **8**, 55 (2006).
- [11] M. Goto, J. Quant. Spect. Rad. Trans. **76**, 331 (2003).
- [12] Y. Itikawa et al., Atomic Data and Nuclear Data Tables **33**, 149 (1985).
- [13] S. Morita, T. Morisaki, M. Goto et al., Nucl. Fusion **47**, 1033 (2007).
- [14] R. Katai, S. Morita, and M. Goto, Rev. Sci. Instrum. **77**, 10F307 (2006).
- [15] M. Goto, and S. Morita, Phys. Rev. E **65**, 026401 (2002).
- [16] H. Yamazaki, M. Goto, S. Morita et al., Plasma Fusion Res. **2**, S1000 (2007).
- [17] C. S. Pitcher and P. C. Stangeby, Plasma Phys. Control. Fusion **39**, 779 (1997).
- [18] W. Engelhardt and W. Feneberg, J. Nucl. Mater. **76**, 818 (1978).
- [19] T. E. Evans et al., Phys. Plasmas **9**, 4957 (2002).
- [20] J. H. Hogan et al., Phys. Control. Fusion **44**, 673 (2002).
- [21] K. H. Finken et al., Nucl. Fusion **38**, 515 (1998).
- [22] T. E. Evans et al., Nature Phys. **2**, 419 (2006).
- [23] C. Breton, et al., Nucl. Fusion **31**, 1774 (1991).
- [24] M. Mattioli et al., Nucl. Fusion **35**, 807 (1995).
- [25] G. Telesca et al., J. Nucl. Mater. **44**, 337 (2005).
- [26] M. Z. Tokar, Phys. Plasmas **6**, 2808 (1999).
- [27] N. Ohyaabu et al., Nucl. Fusion **34**, 387 (1994).
- [28] S. Morita, M. Goto et al., Plasma Sci. Tech **8**, 55 (2006).

- [29] S. Morita, M. Goto et al., *Proc. 26th. European Conference on Controlled Fusion and Plasma Physics*, Maastricht, 1999 (European Physical Society, Geneva, 1999) Vol.23J, p.1321.
- [30] N. Ohyaabu et al., *J. Nucl. Mater.* **266-269**, 302 (1999).
- [31] T. Morisaki et al., *J. Nucl. Mater.* **313-316**, 548 (2003).
- [32] H. Zhou, S. Morita, M. Goto, and M. B. Chowdhuri, will be published in *Rev. Sci. Instrum.* **79**, (2008).
- [33] P. C. Stangeby, *The Plasma Boundary of Magnetic Fusion Devices*, chapter 6, (Institute for Physics Publishing, 2002).
- [34] M. Kobayashi et al., *Contrib. Plasma Phys.* **48**, 255 (2008).
- [35] Y. Feng et al., *Nucl. Fusion* **47**, 807 (2006).
- [36] Y. Feng et al., *Contrib. Plasma Phys.* **44**, 57 (2004).
- [37] D. Reiter et al., *Fusion Sci. Technol.* **47**, 172 (2005).
- [38] M. Kobayashi et al., *Plasma Fusion Res.* **3**, S1005 (2008).

Chapter 5

Summary and conclusion

Two flat-field extreme ultraviolet (EUV) spectrometers for measuring 10–500Å range have been developed to improve the technical basis on the spectroscopic diagnostics and to study the edge impurity transport in high-temperature plasmas of Large Helical Device (LHD). This wavelength range contains many spectral lines from low- to high-Z impurities typically seen in fusion plasmas such as B, C, O, Ar, Ti, Fe, Mo and W. The EUV Spectrometers with varied-line-spacing 1200 (named as 'EUV_Long') and 2400 grooves/mm (named as 'EUV_Short') gratings cover each wavelength range of 50–500Å and 10–130Å ranges, respectively. Spectral characteristics of newly developed laminar-type holographic gratings used for both EUV spectrometers have been studied by comparing with conventional ruled gratings.

Comparison between ruled and holographic gratings for EUV_Long spectrometer shows that both spectral resolutions (FWHM) are excellent for the spectroscopic use and a very similar spectral resolution is obtained for both (e.g. $\Delta\lambda \sim 0.24\text{\AA}$ at $\lambda=200\text{\AA}$). However, only the holographic grating can sufficiently suppress the higher order light. For example, the second order light of CV (40.27Å) is only about 18% to the first order for the holographic grating, whereas the second order light is nearly equal to the first order light for the ruled grating.

Relative sensitivity of the EUV_Long spectrometer was determined using a new technique of EUV bremsstrahlung continuum measurement. As a result, it was found that the sensitivity of the ruled grating quickly deteriorates at wavelengths lower than 150Å, but the holographic grating constantly keeps a high sensitivity against the wavelength. The holographic grating was therefore finally selected for the EUV_Long spectrometer. The absolute calibration has been done using a combination of the bremsstrahlung continuum and the branching ratio technique with two CIV spectral lines in EUV (3p-3s: 312.4Å) and visible (3p-2s: 5810Å) ranges. The absolute calibration curve is obtained continuously against the wavelength. This technique could be an

excellent alternative to overcome a large uncertainty against the wavelength dependence seen in the conventional absolute calibration method using only the branching ratio.

In case of the EUV_Short spectrometer, both ruled and old holographic gratings effectively suppress higher order light, but the ruled grating shows better spectral resolution ($\Delta\lambda=0.083\text{\AA}$ at $\lambda=18.97\text{\AA}$) than the old holographic grating ($\Delta\lambda=0.130\text{\AA}$ at $\lambda=18.97\text{\AA}$). Relative sensitivity was also determined from the EUV bremsstrahlung continuum and the absolute calibration was done by comparing the overlapping wavelength range (50–130 \AA) with absolutely calibrated EUV_Long spectrometer. It was found that the holographic grating is three times brighter than the ruled grating. A new holographic grating has been developed in Shimadzu Co. Ltd. very recently with modified grating parameters. This new holographic grating was also checked instead of the old holographic grating. We thus found that the new grating improved the spectral resolution at lower wavelengths of $\leq 40\text{\AA}$ ($\Delta\lambda=0.900\text{\AA}$ at $\lambda=18.97\text{\AA}$). As a result, the EUV spectroscopy was clearly progressed at shorter wavelength range, at least in 10–30 \AA range, where $\Delta n=1$ transitions of medium-Z impurities (Ar, Ti, Fe etc.) and many EUV spectral lines of high-Z impurities (Mo, W etc.) closely exist.

EUV spectra from Mo and W in 20–500 \AA range have been observed using double-structure impurity pellet injected into LHD plasmas. From the data analysis many spectral lines have been successfully identified and compared with previous experimental results and also with calculated values. Especially, The $\Delta n=1$ transitions of WXXII-WXXVI ($4d^9 4f^k 5p-4d^{10} 4f^k$, $4f^{k-1} 5g-4f^k$: $k=3-7$) in 25–40 \AA range are newly identified with the help of calculated values. The $\Delta n=1$ ($n=3-2$) transitions of Ti and Fe in 10–30 \AA range have been measured using the EUV_Short spectrometer. The spectra from Ne-like TiXIII (FeXVII) to Li-like TiXX (FeXXIV) have been also newly observed simultaneously with a good spectral resolution.

Impurity transport of edge plasmas with ergodic layer in LHD has been studied using CIII to CVI emissions. For this purpose, four resonance transitions of CIII (977 \AA : $2s2p\ ^1P_1-2s^2\ ^1S_0$), CIV (1548 \AA : $2p\ ^2P-2s\ ^2S$), CV (40.27 \AA : $1s2p\ ^1P_1-1s^2\ ^1S_0$) and CVI (33.73 \AA : $2p\ ^2P-1s\ ^2S$) have been observed using EUV_Short spectrometer and two VUV monochromators. The ionization energies of CIII (48eV) and CIV (64eV) are clearly

separated from CV (392eV) and CVI (495eV). These carbon emissions can be then divided into two groups, i.e., CIII+CIV and CV+CVI. Here, the CIII+CIV indicates the influx of the carbon at plasma edge and the CV+CVI indicates the carbon fraction after transport in the ergodic layer. The ratio of CV+CVI to CIII+CIV has been observed in a variety of magnetic configurations and plasma parameters.

The ratio of CV+CVI to CIII+CIV decreases in two orders of magnitude with increasing n_e in the range of $1-8 \times 10^{19} \text{m}^{-3}$. This reduction with n_e comes mainly due to monotonically increased CIII+CIV emissions and constant CV+CVI emissions. This result suggests enhanced impurity screening by the presence of the ergodic layer. On the other hand, the edge impurity transport parallel to the magnetic fields is mainly dominated by the ion thermal force due to ion temperature gradient and the friction force due to proton-impurity collision. The modeling of the edge impurity transport with EMC3+EIRENE code strongly suggests the importance of the friction force in high-density range, which means the appearance of the impurity screening. The density dependence of the measured ratio is in good agreement with the modeling result.

The ratio has been also examined by shifting the plasma axis and changing the thickness of the ergodic layer. The ratio decreases with changing the ergodic layer thickness under similar line-averaged densities. The edge density in the ergodic layer normalized to the core density becomes higher with increasing ergodic layer thickness. As a result, the effect of the impurity screening can be enhanced in thicker ergodic layer. The carbon emissions have been also observed changing the radial position of externally supplied $m/n=1/1$ island. The ratio considerably decreases when the island exists in the ergodic layer. This result evidently indicates that the modification of magnetic field structure in the ergodic layer changes the edge impurity behavior.

Acknowledgements

This doctoral thesis is completed through a study of plasma spectroscopy in the Large Helical Device (LHD) at National Institute for Fusion Science (NIFS), Toki, Japan. Here, I want to thank to all people who have helped me during this work. Without the support of a number of people, there is no way I would have finished my PhD thesis.

At First, my deepest and most sincere thanks go to my supervisor, Prof. Shigeru Morita. From him I have understood not only the principle of the EUV spectroscopy, but also plasma physics in general. He has taught me during these three years the vital knowledge on the every aspect of the experimental study. Whenever I faced difficulties in making progress in my work, he was always ready with a new idea, and an unwavering commitment to solve the problem. His tireless help made my personal life in Japan completely stress-free and enjoyable in addition to his continuous support and encouragement in academic matter.

I am deeply grateful to Dr. Motoshi Goto for his professional support in experimental work and for the many insights on the understanding of atomic physics. I am also thankful to Dr. Masahiro Kobayashi who has always answered my questions promptly and patiently, and as a result of our discussions my knowledge of the edge impurity transport physics has substantially improved.

It is pleasure to acknowledge Dr. R. Sakamoto, Dr. T. H. Watanabe, Dr. S. Masuzaki, Dr. N. Ashikawa, Dr. S. Muto, Dr. T. Morisaki, Prof. T. Kato and Prof. H. Yamada. I would like to thank my fellow graduate students, Dr. R. Katai, Mr. H. Yamazaki, Dr. H. Tsuchiya, Dr. M. Hoshino and Mr. H.Y. Zhou for their help. My special thanks to Dr. Gourab Bansal, Mr. Xu Qi and Mr. Sariful Haque Bhuiya with whom I have shared my joy and sorrow and spent much pleasant times in NIFS engaging in discussion on the many topics, from plasma physics to human nature.

I wish to express my appreciation to all members of LHD experimental group, NIFS and The Graduate University for Advanced Studies (SOKENDAI) staffs for their supports and my sincere gratitude to Prof. Osamu Motojima, Director General, NIFS for his encouragement.

I am grateful to Prof. P. K. Kaw, Director, Institute for Plasma Research (IPR), Gandhinagar, India, for his continuous interest and to members of academic committee for granting me leave to do this study. I wish to convey my special thanks to Dr. P. Vasu for his teaching on the basis of spectroscopic technique and plasma physics during my earlier years in IPR. My sincere thanks Dr. Vinay Kumar for his guidance in spectroscopy and his everlasting encouragement towards my PhD. I remember Ms. Ranjana Manchanda, Dr. N. Ramasubramanian, Dr. Mritunjoy Kundu, Mr. Santanu Banerjee and Mr. Ketan M. Patel from IPR for their enthusiasm on my PhD.

My three years stay in Japan has become perfectly enjoyable and exciting due to my sweet friend, Nilam. Her endless e-mails, SMSs, missed calls and weekend chatting has made my lonely private life energetic and diverse. She has rejoiced in my success and provided moral support during the bad times. I express my thanks to Rajen da, Jayashri di, and cute Ribhu, who brought lots of laugh and happiness in my Japan life whenever I could meet and visit them in Kyushu University, Fukuoka, Japan. Many thanks to my friend Tarak to make my life joyful through his nonstop e-mails.

Finally, my great thanks to my father, mother and brother and other family members in India for the huge moral support given to me during three years of PhD study in NIFS, Toki, Japan.

List of publications

- [1] “Spectroscopic comparison between 1200 grooves/mm ruled and holographic gratings of a flat-field spectrometer and its absolute sensitivity calibration using bremsstrahlung continuum”,
M. B. Chowdhuri, S. Morita, M. Goto, H. Nishimura, K. Nagai and S. Fujioka,
Review of Scientific Instruments **78** (2007) 023501.
- [2] “Line analysis of EUV spectra from Molybdenum and Tungsten injected with impurity pellets in LHD”,
M. B. Chowdhuri, S. Morita, M. Goto, H. Nishimura, K. Nagai and S. Fujioka,
Plasma Fusion Research **2** (2007) S1060.
- [3] “Characteristics of an absolutely calibrated flat-field extreme ultraviolet spectrometer in the 10–130Å range for fusion plasma diagnostics”,
M. B. Chowdhuri, S. Morita and M. Goto,
Applied Optics **47** (2008) 135.
- [4] “Behavior of CIII to CVI emissions during recombining phase of LHD plasmas”,
M. B. Chowdhuri, S. Morita and M. Goto,
Plasma Fusion Research **3** (2008) S1043.
- [5] “Spectroscopic evaluation of three different gratings used for a flat-field EUV spectrometer to monitor $\Delta n=1$ transitions from medium-Z impurities in 10–30Å”,
M. B. Chowdhuri, S. Morita, M. Goto and H. Sasai,
To be published in Review Scientific Instruments **79** (Oct, 2008).
- [6] “Experimental study of impurity screening in edge ergodic layer of Large Helical Device using carbon emissions of CIII to CVI”,
M. B. Chowdhuri, S. Morita, M. Kobayashi, M. Goto, H. Y. Zhou, S. Masuzaki, T. Morisaki, K. Narihara, I. Yamada and Y. Feng,
Submitted to Physics of Plasmas.